

**ULTRASOUND IMAGING OF OXIDATIVE STRESS IN VIVO  
WITH CHEMICALLY GENERATED GAS MICROBUBBLE**

A Dissertation  
Presented to  
The Academic Faculty

by

John Kangchun Perng

In Partial Fulfillment  
of the Requirements for the Degree  
Doctor of Philosophy in the  
Bioengineering Program, School of Electrical and Computer Engineering

Georgia Institute of Technology  
May 2011

**COPYRIGHT 2011 BY JOHN KANGCHUN PERNG**

**ULTRASOUND IMAGING OF OXIDATIVE STRESS IN VIVO**  
**WITH CHEMICALLY GENERATED GAS MICROBUBBLE**

Approved by:

Dr. Niren Murthy, Advisor  
Department of Biomedical Engineering  
*Georgia Institute of Technology*

Dr. W. Robert Taylor  
School of Medicine, Division of  
Cardiology  
*Emory University*

Dr. Mark R. Prausnitz  
School of Chemical Engineering  
*Georgia Institute of Technology*

Dr. F. Levent Degertekin  
School of Mechanical Engineering  
*Georgia Institute of Technology*

Dr. Stefan France  
School of Chemistry and Biochemistry  
*Georgia Institute of Technology*

Date Approved: March 10, 2011

To my family for their love, care, encouragement and support

## ACKNOWLEDGEMENTS

I wish to thank my thesis advisor, Dr. Niren Murthy, for giving me the opportunity to pursue my Ph.D. study in his laboratory. Throughout my graduate studies at Georgia Tech, he has provided with guidance and support for the completion of my thesis. I am grateful for his insightful ideas, intellectual perspective, constructive criticisms, and for motivating me to excel and think critically in research.

I also wish to thank the members of my research lab. I like to thank Dr. Madhuri Dasari for teaching me many techniques of organic chemistry synthesis. I like to thank Dr. Kousik Kundu for guiding me through many principles of organic chemistry reactions and insights into their mechanism. I like to thank Dr. Xinghai Ning, Dr. Sungmun Lee and Dr. Chen-Yu Kao for their support and encouragement throughout my studies. I like to thank Scott Wilson, Jay Sy and Warren Gray for their friendship and intellectual feedback. I like to thank Dr. Dongin Kim for his help on preparation of liposomes and micelles. I like to thank Dr. Seungjun Lee for his help on acoustic characterization and principles of animal physiology.

I would also like to thank our collaborators, Dr. Degertekin and Sarp Satir for providing much help and advice on ultrasound system, bubble acoustics and signal processing. I like to thank Dr. Catherine Ferrara and Dr. Charles Caskey for their help and insightful discussions on acoustic characterization of bubble nucleation. I also like to thank Dr. Robert Taylor, Dr. Sarah Knight, Dr. Daniel Sorescu, Dr. Lihong Cheng and Milton Brown for their help with *in vivo* animal studies.

I wish to thank Dr. Stefan France, Dr. Bob Taylor, Dr. Prausnitz, and Dr. Degertekin for serving on my thesis committee. Their advice and guidance have helped me greatly in my thesis research.

I am also grateful to the funding sources that made my thesis research possible. These funding sources include The Parker H. Petit Institute for Bioengineering and Biosciences, the National Science Foundation, the TI:GER program from the Georgia Tech School of Management, and the National Institute of Health.

I would like to thank all my friends and colleagues in IBB and the Bioengineering program at Georgia tech. They have definitely made my PhD studies an enjoyable journey.

Lastly, I like to thank my parents and my dear wife for their love and support. I would not be able to complete my PhD degree without their encouragement, care and sacrifice.

# TABLE OF CONTENTS

	Page
ACKNOWLEDGEMENTS	iv
LIST OF TABLES	x
LIST OF FIGURES	xi
LIST OF SYMBOLS AND ABBREVIATIONS	xv
SUMMARY	xvii
<u>CHAPTER</u>	
1 SPECIFIC AIMS	1
1.1 Introduction	1
1.2 Specific Aim I	1
1.3 Specific Aim II	2
1.4 Specific Aim III	3
1.5 Significance	4
2 LITERATURE REVIEW	5
2.1 Ultrasound imaging and microbubble contrast agent	5
2.2 ROS and impact on human diseases	6
2.3 Current technology and motivation for imaging ROS	8
2.4 Bubble nucleation from chemical reactions	9
2.5 Classical bubble nucleation theory	10
2.6 Ultrasound detection of gas bubbles	11
2.7 Liposomal encapsulation and stabilization of gas bubbles	13
2.8 <i>In vivo</i> imaging of oxidative stress	15
3 CHEMICAL GAS GENERATION INVOLVING RADICAL OXIDANTS	17

3.1	Introduction	17
3.2	Materials and Methods	18
3.2.1	Allylhydrazine and synthesis of allylhydrazine analogs	18
3.2.2	Trinitrobenzene sulfonic (TNBS) assay	21
3.2.3	ABTS assay	22
3.3	Results	23
3.3.1	Synthesis of allylhydrazine analogs	23
3.3.2	Oxidation of allylhydrazine with the hydroxyl radical	27
3.3.3	Oxidation kinetics of allylhydrazine with radical oxidants	28
3.4	Discussion	28
3.4.1	Oxidation kinetics and implication for clinical applications	28
3.4.2	Theoretical prediction for threshold of bubble nucleation	30
4	ULTRASOUND DETECTION OF BUBBLE NUCLEATION	31
4.1	Introduction	31
4.2	Materials and Methods	32
4.2.1	Optical observation and acoustic characterization of bubble nucleation	32
4.2.2	Ultrasound characterization system	33
4.2.3	Optimization of ultrasound parameters	35
4.2.4	<i>In vitro</i> acoustic characterization of allylhydrazine with the hydroxyl radical	36
4.2.5	<i>In vitro</i> characterization with clinical ultrasound system	37
4.3	Results	41
4.3.1	Optical confirmation of bubble nucleation	41
4.3.2	Optimization of ultrasound parameters	42
4.3.3	Acoustic response of allylhydrazine with the hydroxyl radical	43

4.3.4	<i>In vitro</i> characterization of bubble nucleation with clinical ultrasound system	49
4.4	Discussion	53
4.4.1	Optical observation of bubble nucleation	53
4.4.2	Classical nucleation theory and observed results	54
4.4.3	Effect of ultrasound parameters on bubble nucleation and rectified diffusion	55
5	LIPOSOMAL ENCAPSULATION AND STABILIZATION OF GAS MICROBUBBLE	60
5.1	Introduction	60
5.2	Materials and Methods	62
5.2.1	Liposome composition and formulation	62
5.2.2	Liposome characterization	63
5.2.3	<i>In vitro</i> acoustic characterization of allylhydrazine encapsulated in liposomes	64
5.2.4	<i>In vivo</i> biodistribution of liposomes loaded with fluorescent marker	65
5.3	Results	67
5.3.1	Physical characterization of liposomes	67
5.3.2	<i>In vitro</i> acoustic response of allylhydrazine encapsulated within liposomes	73
5.3.3	<i>In vivo</i> biodistribution of liposomes	77
5.4	Discussion	80
5.4.1	Acoustic improvement of liposomal encapsulation	80
5.4.2	Biodistribution of liposomes and <i>in vivo</i> implication	81
6	IN VIVO IMAGING OF OXIDATIVE STRESS USING CLINICAL ULTRASOUND SYSTEM	82
6.1	Introduction	82
6.2	Materials and Methods	83



6.2.1 <i>In vivo</i> study with intraperitoneal injection of allylhydrazine and hydroxyl radical	83
6.2.2 <i>In vivo</i> LPS model with allylhydrazine	84
6.2.3 <i>In vivo</i> LPS model with allylhydrazine encapsulated in liposomes	85
6.2.4 Comparison with clinical contrast agents (Definity)	86
6.3 Results	87
6.3.1 Ultrasound imaging of bubble nucleation inside intraperitoneal cavity of mice	87
6.3.2 <i>In vivo</i> imaging of oxidative stress using allylhydrazine	91
6.3.3 <i>In vivo</i> imaging of oxidative stress using allylhydrazine encapsulated within liposomes	94
6.3.4 Comparison with clinical contrast agent (Definity)	97
6.4 Discussion	101
6.4.1 <i>In vivo</i> imaging of oxidative stress using clinical ultrasound system	101
6.4.2 <i>In vivo</i> enhancement of liposomal encapsulation	101
7 SUMMARY AND FUTURE DIRECTIONS	103
7.1 Overall Summary	103
7.2 Aim I: Ultrasound Detection of Chemically Generated Microbubble	104
7.3 Aim II: Liposomal Encapsulation and Stabilization of Microbubble	105
7.4 Aim III: <i>In Vivo</i> Imaging of Oxidative Stress	105
7.5 Conclusions	106
7.6 Future directions	106
APPENDIX A: CLINICAL ULTRASOUND SYSTEM AND CALIBRATION	108
REFERENCES	111
VITA	123

## LIST OF TABLES

	Page
Table 1: Ultrasound parameters that can affect bubble acoustic response	36
Table 2: Summary of ultrasound parameters and acoustic response of allylhydrazine with various concentrations of the hydroxyl radical	47
Table 3: Summary of acoustic response of allylhydrazine analogs with various concentrations of the hydroxyl radical	48
Table 4: Phospholipid types and abbreviation	62
Table 5: Liposomes compositions	63
Table 6: Acoustic response of allylhydrazine encapsulated within various liposome compositions at various hydroxyl radical concentrations	74

## LIST OF FIGURES

	Page
Scheme 1.    Ultrasound imaging of oxidative stress <i>in vivo</i> with chemically generated gas bubbles	xviii
Figure 2.1.   The role of ROS in normal physiology and the development of diseases	7
Figure 2.2.   The mechanism of intramolecular retro-ene reaction of allylic hydrazine	10
Figure 3.1.   Chemical synthesis of 2-fluoro-allylhydrazine	19
Figure 3.2.   Reaction of trinitrobenzene sulfonic acid (TNBS) with primary amine on allylhydrazine	21
Figure 3.3.   Structure of azinobis-3-ethylbenzothiazoline-6-sulfonic acid (ABTS)	23
Figure 3.4.   Allylhydrazine reacts with the hydroxyl radical and is decomposed into a product that has no reactivity with TNBS	27
Figure 3.5.   The absorbance of ABTS assay shows that allylhydrazine reacts rapidly with radical oxidants	28
Figure 3.6.   Generation of gas molecules from the reaction of allylhydrazine with radical oxidants	29
Figure 4.1.   Measuring system for simultaneous optical observation and acoustic characterization of bubble nucleation	33
Figure 4.2.   Ultrasound measurement system for <i>in vitro</i> characterization of allylhydrazine with the hydroxyl radical	34
Figure 4.3.   Matlab user interface for displaying data acquisition and setting ultrasound parameters	35
Figure 4.4.   In vitro characterization using clinical ultrasound system	38
Figure 4.5.   Representative ultrasound image showing the region of interest	40
Figure 4.6.   Background subtraction of ultrasound video images	40
Figure 4.7.   Video images of the cellulose tube showing that allylhydrazine can nucleate gas bubbles in the presence of the hydroxyl radical	41

Figure 4.8.	The microbubble identified by optical observation inside the cellulose generated a strong acoustic echo (55 – 58 $\mu$ s). The microbubble displayed a 20 fold increase in acoustic signal intensity compared to adjacent fluid	42
Figure 4.9.	Acoustic characterization of allylhydrazine before the addition of the hydroxyl radical	44
Figure 4.10.	Acoustic characterization of allylhydrazine after the addition of the hydroxyl radical (100 $\mu$ M)	44
Figure 4.11.	Allylhydrazine can react with hydroxyl radicals to generate bubbles and reach its peak acoustic intensity within a 10 minute period	45
Figure 4.12.	Allylhydrazine can detect micromolar concentrations of ROS and showing a linear correlation between ultrasound intensity and the hydroxyl radical concentration within the concentration range of 10 $\mu$ M - 1 mM ( $R^2 = 0.98$ )	46
Figure 4.13.	Representative ultrasound images of bubble detection with a clinical ultrasound system at various concentrations of the hydroxyl radical with allylhydrazine	50
Figure 4.14.	Bubble generation from the reaction of allylhydrazine with the hydroxyl radical can be detected in vitro by a clinical ultrasound system	51
Figure 4.15.	Representative ultrasound images showing that more bubbles are generated inside the holder at higher mechanical index	52
Figure 4.16.	Stronger ultrasound power (higher MI) resulted in larger change in video intensity, suggesting enhancement of bubble nucleation	53
Figure 4.17.	Threshold for rectified diffusion at 1 MHz sinusoidal oscillation frequency	58
Figure 4.18.	Threshold for rectified diffusion at 2.25 MHz sinusoidal oscillation frequency.	59
Figure 4.19.	Threshold for rectified diffusion at 5 MHz sinusoidal oscillation frequency	59
Figure 5.1.	Liposome encapsulation efficiency of allylhydrazine determined by the TNBS assay	72
Figure 5.2.	Acoustic response of allylhydrazine encapsulated within liposomes (APLs) showing linear correlation between ultrasound intensity and hydroxyl radical concentrations	75

Figure 5.3.	Hydroxyl radical added to empty liposomes did not show increase in ultrasound intensity	76
Figure 5.4.	Control experiments demonstrating that the APLs are specific toward the hydroxyl radical	77
Figure 5.5.	Fluorescence imaging revealed that liposomes loaded with IR-786 dye can reach the liver in 10 minutes	78
Figure 5.6.	Fluorescence imaging of liposomes loaded with IR-786 in the heart, liver, lung and kidney	79
Figure 5.7.	Biodistribution of APL-based liposomes loaded with Rhodamine B dye 10 minutes after injection	80
Figure 6.1.	Injection of allylhydrazine (100 mM) and hydroxyl radical (1 mM) inside mouse IP cavity	88
Figure 6.2.	Injection of allylhydrazine (100 mM) and hydroxyl radical (86 $\mu$ M) inside mouse IP cavity	90
Figure 6.3.	Representative ultrasound images of mice livers treated with allylhydrazine and LPS versus treatment with allylhydrazine and saline	92
Figure 6.4.	Quantitative analysis of the ultrasound images in Fig. 6.3 A and B demonstrated that mice treated with allylhydrazine and LPS increased their normalized mean video intensity by 60% (circles), compared to a 30% increase in control mice treated with allylhydrazine and saline (squares)	93
Figure 6.5.	Representative ultrasound images of mice livers treated with the APLs and LPS versus mice treated with the APLs and saline	95
Figure 6.6.	Quantitative analysis of the ultrasound images in Fig. 6.5 A and B demonstrated that mice treated with the APLs and LPS increased their normalized mean video intensity by 40% (circles), compared to no increase in control mice treated with the APLs and saline (squares). In addition, quantitative image analysis of mice treated with LPS and empty liposomes (n = 5) did not show an increase in normalized mean video intensity (triangles). The vertical bars represent standard error	96
Figure 6.7.	B-mode imaging of mice liver after intravenous injection of clinical contrast agent Definity	98
Figure 6.8.	B-mode and Doppler imaging of mice liver after intravenous injection of clinical contrast agent Definity	100
Figure A.1.	Conversion between mechanical index (MI) and ultrasound power	109

Figure A.2. Linear relationship between mean video intensity and power at -20 dB gain 109

Figure A.3. Linear relationship between mean video intensity and power at -7 dB gain 110

Figure A.4. Linear relationship between video intensity and gain at  $MI = 0.05$  110

## LIST OF SYMBOLS AND ABBREVIATIONS

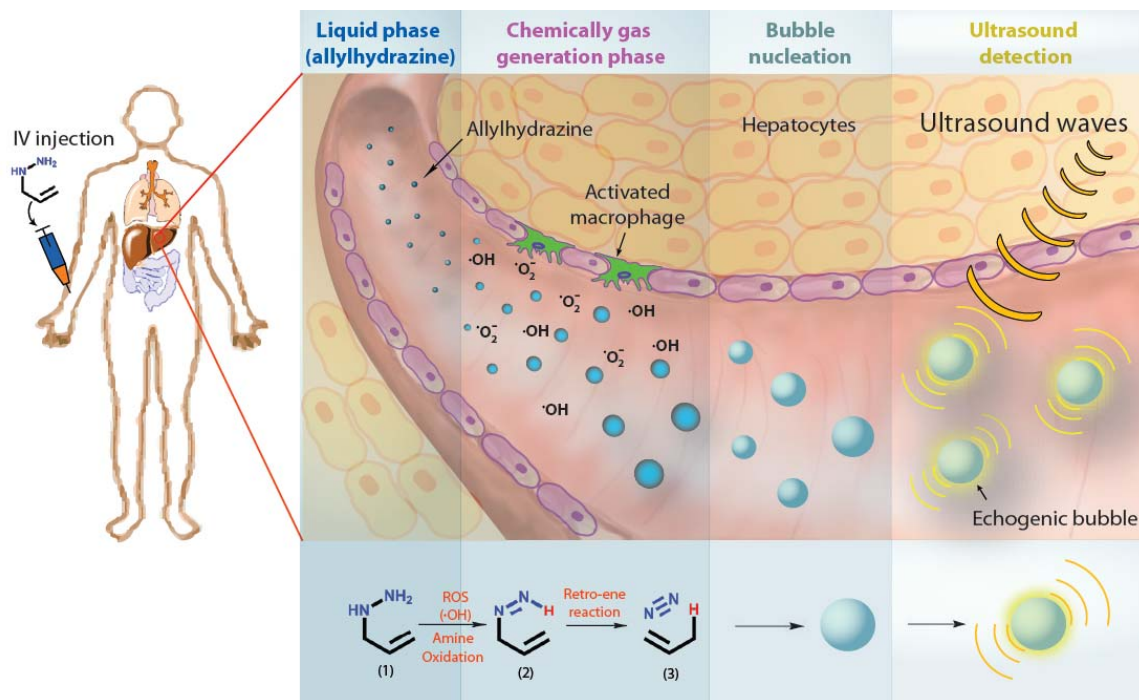
ABTS	2,2'-azinobis-3-ethylbenzothiazoline-6-sulfonic acid
APLs	Allylhydrazine encapsulated within Phospholipid Liposomes
CT	Computed Tomography
DCM	Dichloromethane
DI	Deionized
DLS	Dynamic Light Scattering
DPPA	1,2-Dipalmitoyl-sn-glycero-3-phosphatidic acid
DPPC	1,2-Dipalmitoyl-sn-glycero-3-phosphocholine
DPPE	1,2-Dipalmitoyl-sn-glycero-3-phosphoethanolamine
DSPC	1,2-Distearoyl-sn-glycero-3-phosphocholine
ESR	Electron Spin Resonance
EtOAc	Ethyl Acetate
FDA	Federal Food and Drug Administration
FFT	Fast Fourier Transform
ICAM	Inter-Cellular Adhesion Molecule
IP	Intraperitoneal
LPS	Lipopolysaccharide
MI	Mechanical Index
MRI	Magnetic Resonance Imaging
MWCO	Molecular Weight Cut Off
NMR	Nuclear Magnetic Resonance
PBS	Phosphate Buffer Saline

PEG	PolyEthyleneGlycol
PET	Positron Emission Tomography
PRF	Pulse Repetition Frequency
RBC	Red Blood Cell
RF	Radio Frequency
ROI	Region of Interest
ROS	Reactive Oxygen Species
SOD	Super Oxide Dismutase
STP	Standard Temperature and Pressure
TBAHS	Tetrabutylammonium Hydrogen Sulfate
TLC	Thin Layer Chromatography
TNBS	Trinitrobenzene Sulfonic Acid
UCA	Ultrasound Contrast Agent



## SUMMARY

Ultrasound contrast agents (UCA) have tremendous potential for *in vivo* molecular imaging because of their high sensitivity and great spatial resolution of ultrasound imaging. However, the diagnostic potential of UCAs has been difficult to exploit because current contrast agents are based on pre-formed microbubbles, which can only detect cell surface receptors. In this work, we demonstrated that chemical reactions that generate gas forming molecules can be used to perform molecular imaging by ultrasound *in vivo*. This new approach for generating ultrasound contrast agents was demonstrated by imaging reactive oxygen species (ROS) *in vivo* with allylhydrazine, a compound that is converted into nitrogen and propylene gas after reacting with radical oxidants (Scheme 1). We demonstrated that allylhydrazine encapsulated within liposomes (termed APLs) can detect a 10  $\mu$ M concentration of radical oxidants by ultrasound, and can image oxidative stress in mice, induced by lipopolysaccharide (LPS), using a clinical ultrasound machine. We showed that a 1-2% increase in gas concentration above saturation can be detected acoustically and suggest that numerous biological targets can be imaged via appropriately designed gas forming reactions. This work was the first demonstration of *in vivo* imaging of ROS using ultrasound, and this work presented a new strategy to generate gas bubbles from reactions involving radical oxidants. We anticipate numerous applications of chemically generated microbubbles, given the excellent spatial resolution of ultrasound imaging, its widespread clinical use and its high sensitivity to detect gas bubbles.



**Scheme 1.** Ultrasound imaging of oxidative stress *in vivo* with chemically generated gas bubbles

# CHAPTER 1 SPECIFIC AIMS

## 1.1 Introduction

Conventional ultrasound contrast agents (UCA) are composed of preformed microbubbles conjugated with ligands that can bind to cell surface receptors. However, the development of UCA that can image disease biomarkers remains a major challenge because many disease biomarkers are not expressed through the up-regulation of surface receptors. Reactive oxygen species (ROS), for example, are disease biomarkers that are central to the development of inflammatory diseases, atherosclerosis and cardiovascular diseases. Currently there are no contrast agents that can image ROS in a clinical setting. Hence, the ability to image ROS *in vivo* associated with inflammation, for example, would have translational impact on clinical diagnosis and early medical treatment.

The overall objective of this thesis is to develop a new ultrasound contrast agent that has the physical and chemical properties needed to image ROS *in vivo*. **The central hypothesis is that ROS can be imaged by ultrasound *in vivo* via chemical reactions that generate gas bubbles in the presence of radical oxidants.** To accomplish this task, we will test our central hypothesis through the following three specific aims:

## 1.2 Specific Aim I

**Design appropriate chemical reactions that can chemically generate gas bubbles in the presence of radical oxidants and characterize the *in vitro* acoustic response**

The objectives of this aim were to investigate the oxidation kinetics of various chemical reactions that generate gas forming molecules, and their *in vitro* acoustic

response. Our working hypothesis was that allylhydrazine and its analogs can produce nitrogen gas molecules and nucleate gas bubbles under physiologically relevant concentrations of radical oxidants. To accomplish this aim, several analogs of allylhydrazine were synthesized and their oxidation kinetics were characterized using various fluorescence spectroscopy assays. We showed that the oxidation kinetics of allylhydrazine is suitable for bubble generation under physiological conditions. Both optical observation and acoustic characterization confirmed that the oxidation of allylhydrazine can nucleate gas bubbles. A custom-built ultrasound system was used to study the effect of various ultrasound parameters on bubble nucleation, and the ultrasound parameters were optimized for bubble detection. We found a linear correlation between the ultrasound intensity and the concentrations of radical oxidants. The outcomes of this Aim are described in Chapter 3 and 4.

### **1.3 Specific Aim II**

#### **Encapsulate allylhydrazine within liposomes to improve bubble stability and to enhance *in vivo* efficacy**

The objectives of this aim were to formulate the optimal liposome composition to encapsulate allylhydrazine for *in vivo* application. Our working hypothesis was that encapsulating allylhydrazine within liposomes can improve the bubble stability and enhance the *in vivo* efficacy. To accomplish this aim, we analyzed the effects of various liposome compositions on bubble nucleation, including lipid chain length, PEGylation, incorporation of charged lipid and porphyrin, and lipid to allylhydrazine loading ratio. We characterized the acoustic response of allylhydrazine encapsulated within liposomes,

and we found that allylhydrazine encapsulated within liposomes displayed stronger ultrasound intensity than free allylhydrazine. We also investigated the *in vivo* biodistribution of liposomes and we identified the liver as a suitable target organ for *in vivo* imaging. The results of this Aim are described in Chapter 5.

### **1.4 Specific Aim III**

#### **Demonstrate *in vivo* imaging of oxidative stress using a clinical ultrasound system**

The objectives of this aim were to evaluate the feasibility of using allylhydrazine encapsulated within liposomes (APLs) to image oxidative stress *in vivo* with a clinical ultrasound system. Our *working hypothesis* was that relative oxidative stress can be assessed using a lipopolysaccharide (LPS) endotoxin-induced inflammation model. We first investigated an *in vivo* phantom experiment by direct local injection of allylhydrazine and hydroxyl radicals inside the intraperitoneal (IP) cavity of mice, and a clinical ultrasound system was used for imaging. To image oxidative stress *in vivo* with ultrasound, LPS was injected into the IP cavity of mice to induce inflammation overnight, and the APLs were injected intravenously through the retro-orbital capillary. We compared the ultrasound images of the liver from mice treated with LPS and the APLs versus mice treated with saline the APLs and we analyzed the video intensity in the region of interest. We also used a clinical ultrasound contrast agent for comparison. The outcomes of this Aim are described in Chapter 6.

## 1.5 Significance

Clinical ultrasound imaging provides non-invasive real-time imaging with good 3D spatial resolution, and the application of ultrasound contrast agents for molecular imaging can enhance the diagnosis of many diseases. Here, we presented a new strategy to create ultrasound contrast that can image ROS via chemically generated microbubbles. Since the overproduction of ROS are implicated in many diseases such as inflammation, atherosclerosis and cancer [1], the ability to image ROS *in vivo* can help clinicians diagnose diseases early. Furthermore, classical theory predicts that bubble nucleation occurs at exceedingly high concentrations above gas supersaturation. In this work, we showed that ultrasound can detect a 1-2% increase in gas concentration above saturation. Although many have reported that bubble nucleation can occur at much lower concentrations in the presence of pre-existing nuclei for bubble nucleation, using ultrasound to detect bubble nucleation is much more sensitive than previous methods with optical observation. This approach opens up the development of new ultrasound contrasts, and numerous biological targets can be imaged via appropriately designed gas forming reactions. We anticipate numerous applications of chemically generated microbubbles, given the excellent spatial resolution of ultrasound imaging, its widespread clinical use and its high sensitivity to detect gas bubbles.

## **CHAPTER 2 LITERATURE REVIEW**

### **2.1 Clinical ultrasound imaging and microbubble contrast agent**

Ultrasound is widely used for diagnostic imaging, and nearly 25% of all imaging studies worldwide are conducted by ultrasound examinations [2]. Ultrasound imaging is noninvasive, cost-effective, portable, and provides real-time imaging with good spatial and temporal resolution, allowing evaluation of dynamic physiological processes [3]. Clinical examples include blood pool enhancement, characterization of liver lesions and perfusion imaging. In certain clinical applications such as echocardiogram, ultrasound is the most cost-effective method compared to other modalities (MRI, CT or PET). Ultrasound has also been used to guide surgery such as radioactive seed implants in the prostate [4].

In recent years, the introduction of microbubbles as contrast agents for ultrasound has greatly improved image quality and diagnostic value [5]. Microbubble contrast agents consist of a gas core (air or perfluorocarbon) which is stabilized by a shell (denatured albumin, phospholipid, or surfactant). The principle behind using microbubbles as contrast agents is based on their compressibility. Gas-containing microbubbles are 10,000 times more compressible than water or tissue. This results in a very high echogenicity (up to 300 fold signal enhancement) such that the echo from an individual microbubble contrast agent can be detected by a clinical ultrasound system. The microbubble contrast agents behave hemodynamically like red blood cells (RBC). The unique properties of microbubbles as true intravascular tracers have enabled noninvasive measurements of microvascular perfusion in heart, brain, kidney, skeletal muscle, skin grafts, and solid tumors [6].

An ideal ultrasound contrast agent (UCA) should be non-toxic, injectable intravenously, capable of crossing pulmonary capillary bed ( $<10\mu\text{m}$ ) and stable enough to achieve enhancement during examination (few minutes) [7]. Microbubbles can also be directed selectively to specific vascular beds by conjugating targeting ligands (peptides, antibodies, aptamers) to their surface [8-9]. Molecular imaging with targeted microbubbles has been used for *in vivo* assessment of inflammation [10], angiogenesis [11-13], thrombus formation [14-15], tumor vasculature [16-18], and spleen infarctions [19-20]. Current targeted imaging with microbubble contrast agents are based on molecular recognition of ligands with cell receptor. However, many disease biomarkers are not expressed through the up-regulation of surface receptors, and pre-formed gas bubbles cannot detect intracellular events.

## **2.2 ROS and impact on human diseases**

Reactive oxygen species (ROS) are disease biomarkers and the overproduction of ROS is associated with many diseases including inflammation, atherosclerosis, cardiovascular disease, ischemia/reperfusion, and cancer. The exact mechanisms and involvement of ROS in these diseases are not entirely known, and are the subject of intense research. There is a strong correlation between ROS overproduction, oxidative stress, cellular damage and aging, and hence the maintenance of ROS level is essential to homeostasis [1, 21-22]. **Figure 2.1** shows the role of ROS in normal physiology and the development of diseases.



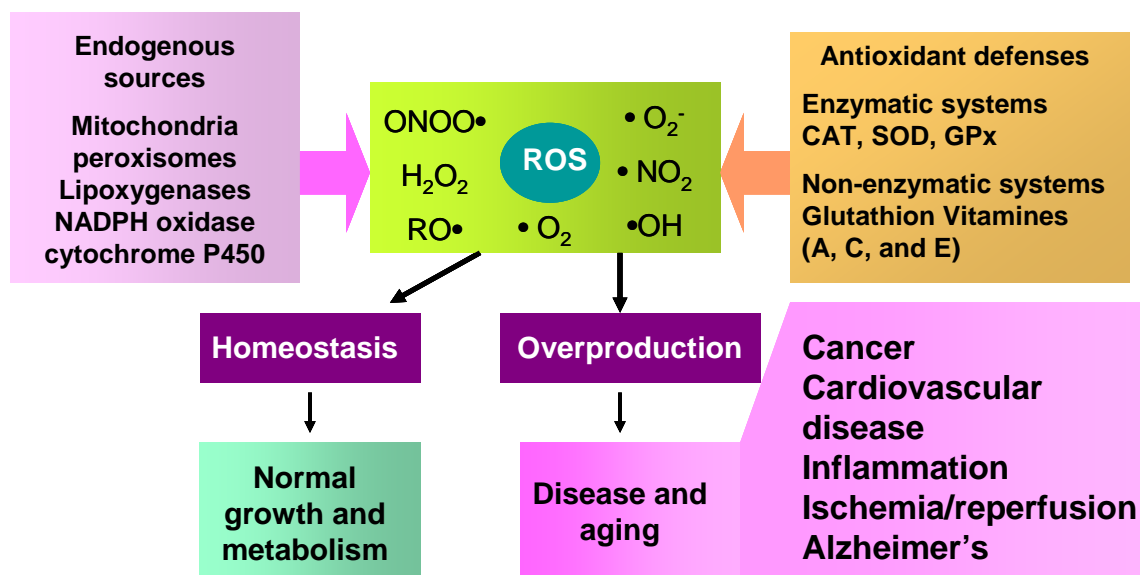


**Figure 2.1.** The role of ROS in normal physiology and the development of diseases

In the 1950s, Denham Harman first proposed the ‘free-radical theory’ of aging, speculating that endogenous oxygen radicals were generated in cells and resulted in a pattern of cumulative damage [23]. Later, the discovery of superoxide dismutase (SOD), an enzyme whose sole function is to convert superoxide anion into hydrogen peroxide provided strong support for Harman’s hypothesis [24]. Since then, the recognition of ROS led to the discovery of other reactive oxygen species and recent evidence indicates that ROS act as messengers in cellular signaling pathways that affect cell proliferation and/or cell death [21, 25]

Most estimates suggest that the majority of intracellular ROS production occurs at the electron transport chain in the mitochondria [26-27]. During energy transduction, a small number of electrons “leak” to oxygen prematurely, forming the oxygen free radical superoxide [8, 28]. Measurements on submitochondrial particles suggest an upper limit

of 1-3% of all electrons in the transport chain “leaking” to generate superoxide [29]. Superoxide species are very reactive and can be converted to hydroxyl radical ( $\bullet\text{OH}$ ) and various downstream reactive oxygen species. As a result, these reactive oxygen species can cause damage to DNA, lipid and proteins [30-31].

### **2.3 Current technology and motivation for imaging ROS**

Despite the fact that ROS is a focus of intense research interest and thousands of papers have been published on this subject, there is a lack of imaging techniques to measure cellular ROS production *in vivo*. Current methods to measure ROS quantitatively such as electron-spin-resonance (ESR) and HPLC require freezing the sample in liquid nitrogen or cumbersome sample preparation, which are not suitable for *in vivo* imaging. Currently, the only practical method to image ROS is by fluorescence spectroscopy. In fluorescence imaging, a fluorescent probe reacts with specific reactive oxygen species and the change in fluorescence intensity (at a detectable wavelength) is measured. The advantage of fluorescence imaging includes high sensitivity (down to nanomolar concentration with some probes), specificity, and spatial resolution in microscopic imaging techniques [32]. Different probes have been developed for various reactive oxygen species [33]. However, fluorescence imaging has shallow penetration depth ( $< 1\text{ cm}$ ) and poor spatial resolution, which presents a serious challenge for *in vivo* imaging of deep tissue or large animal in clinical applications. Recently, a few fluorescent probes have been developed for *in vivo* imaging of ROS in small animals such as mice [34-36], but their applicability for *in vivo* imaging in large animals would require invasive procedure such as intravascular catheter or biopsy. Other major issues

with these fluorescent probes include auto-oxidation, solubility, emission wavelength, and toxicity [33, 36]. To say the least, the limitations in current technology call for the development of new imaging modalities that can detect ROS *in vivo* non-invasively with high resolution, sensitivity, specificity and stability.

## 2.4 Bubble nucleation from chemical reactions

Our strategy is to detect ROS by ultrasound via chemical reactions that generate gas forming molecules in the presence of ROS. Since the human body is saturated with nitrogen, an inert gas, chemical reactions that generate nitrogen or other inert gases would be suitable for *in vivo* imaging. Furthermore, in order to generate gas bubbles chemically, the chemical reactions should be specific toward radical oxidants, sufficiently fast in clinical setting, and generate enough gas under physiological conditions that can be detected by ultrasound.

Rubin & Noyes first demonstrated chemical generation of diatomic gases  $H_2$ ,  $N_2$ ,  $O_2$ , CO and NO in aqueous solutions and measured the rates of bubble nucleation respectively [37]. For bubble generation involving free radicals, Corey showed that allylic hydrazine can be oxidized,  $RNHNH_2 \rightarrow RN=NH$ , followed by a 1,5-sigmatropic rearrangement of hydrogen with loss of nitrogen gas [38]. Sorenson proposed that allyldiazenes undergo intramolecular retro-ene reactions and showed that this is a concerted process involving a six-center cyclic transition state [39] (see **Figure 2.2**), although other mechanisms may be possible [40-43]. The oxidation rate of substituted hydrazines by superoxide ion ( $O_2^{\cdot -}$ ) has also been reported [44-48]. These studies

provided the understanding of how to design appropriate chemistry that can generate nitrogen gas from the reaction with free radicals.

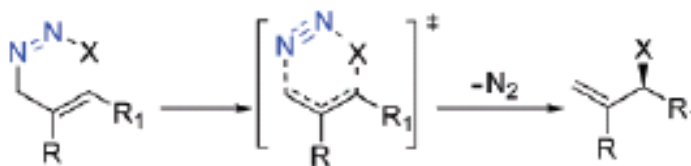


**Figure 2.2.** The mechanism of intramolecular retro-ene reaction of allylic hydrazine

## 2.5 Classical bubble nucleation theory

There have been many studies on bubble nucleation from supersaturated solutions and classical bubble nucleation theory predicts that homogeneous bubble nucleation should occur at exceedingly high concentrations above gas supersaturation [49-50]. In general, there are three ways to measure bubble nucleation. First, reducing the external pressure below the vapor pressure of a pure liquid can cause cavitation. Second, increasing the temperature until the vapor is more stable than a pure liquid can cause boiling. Third, if a gas is dissolved in the liquid, then changing the conditions to create a supersaturated solution may nucleate gas bubbles. The last scenario was often achieved by chemical generation of gas molecules, and experiments were designed to measure the supersaturation needed to cause appreciable nucleation. The threshold for bubble nucleation was measured by optical observation [51].

Experimental evidence based on the first and second methods to measure bubble nucleation showed good agreement with theoretical prediction. However, many reported that the threshold of bubble nucleation from gas forming reactions was much lower than theoretical prediction, and sometimes by as much as 2 orders of magnitude [52].

Furthermore, optical observations have limited sensitivity because it requires the observer to note the onset of bubble nucleation, and this means that the threshold for bubble nucleation could be even lower if more accurate methods are available. Some explanations for the discrepancies between bubble nucleation theory and experimental results are due to the catalytic effect of hetero surfaces. It has been shown that in the presence of pre-existing bubble nuclei, such as on the surfaces of the container or in the bulk solution, the energy required to nucleate bubble is much lower [51, 53], and therefore, bubble nucleation can occur at much lower concentrations.

In the case of nitrogen, its solubility in water is 550  $\mu\text{M}$  under standard condition (STP 1atm, 20°C) and 450  $\mu\text{M}$  at 37°C [37]. The nitrogen gas concentration in the blood is nearly saturated ( $760 \text{ Torr} \times 0.78 \times 8.42 \times 10^{-7} \text{ mol/L}\cdot\text{Torr} = 500 \mu\text{M}$ ), which suggests that, theoretically, increasing the nitrogen concentration by a small amount could exceed the nitrogen saturation in blood. The lowest reported nitrogen concentration for homogeneous bubble nucleation is 10 mM, or 20 times above supersaturation [54].

## **2.6 Ultrasound detection of gas bubbles**

Ultrasound is extremely sensitive to gas bubbles and is capable of detecting individual micron-sized gas bubble with pico-liter ( $10^{-12} \text{ L}$ ) volume [55-57]. The reason is that microbubbles under an ultrasound field undergo volumetric oscillation and this vibration of the microbubbles produces a strong backscattered acoustic signal that can be detected and reproduced as an opacification on ultrasound imaging [58]. At low acoustic power ( $<100 \text{ kPa}$ ) these oscillations are linear and the frequency of the scattered signal is unaltered. As the acoustic power increases ( $100 \text{ kPa} - 1 \text{ MPa}$ ), non-linear interactions

occur because microbubbles resist compression more strongly than expansion. Microbubbles resonate (in the diagnostic range 1-20 MHz) and emit harmonic signal at multiples of the insonating frequency. These harmonic signals are bubble-specific and can be used to distinguish scattered signal from tissue. At even higher power ( $>1$  MPa), highly non-linear behavior occurs with bubble destruction which can be coupled with specific detection modes to differentiate contrast signal from background [2]. Although ultrasound is very sensitive for detecting gas bubble, using ultrasound to measure bubble nucleation from chemical generation of gas molecules has not been reported.

The behavior of free gas bubbles in solution has been studied over many years and is well understood [59]. Gas dissolved in liquid solution can nucleate, grow or dissolve back in solution [60]. On the other hand, the interaction between microbubbles and ultrasound beam is quite complex and requires specific signal processing to improve bubble detection (e.g. pulse inversion, harmonic imaging) [7]. Among the interactions between ultrasound and microbubbles, two phenomenon of particular interest are rectified diffusion and inertial cavitation. In rectified diffusion, a bubble that would ordinarily dissolve in a liquid may increase in mass, rather than dissolve, if the amplitude of the pressure oscillations exceeds a certain threshold value [61]. Inertial cavitation occurs at very high acoustic field, when a bubble expands and collapses violently, generating heat and light (sonoluminescence).

Microbubble-specific imaging sequences have been designed by varying imaging parameters such as the acoustic power, the transmit and receive frequencies, the pulse frequency, the pulse phase and amplitude. Optimization of these parameters is required for different contrast agents to obtain the best diagnostic performance [62]. In recent

years, some people used optical methods to study bubble behavior under an ultrasound field. They have demonstrated detection of single microbubble by ultrasound and verified optically. For example, de Jong used a 100 MHz high speed camera to capture microbubble oscillation optically [63]. Ferrara captured both the optical and acoustical dynamics of microbubble inside neutrophil using similar methods [58, 64-65], and they investigated the interaction of microbubbles with the microvessel wall [66]. These advancements allow visualization and characterization of individual bubble behavior under an acoustic field.

## **2.7 Liposomal encapsulation and stabilization of gas bubbles**

Maintaining bubble size is important because clinical ultrasound frequencies (1-10 MHz) are optimized for bubble size between 1-5  $\mu\text{m}$ . However, free gas bubbles suspended in liquid can coalesce, grow or shrink [67]. Studies have shown that unencapsulated bubbles of the same size would disappear within a few seconds after having been introduced in the blood circulation. This is because a free gas bubble has a finite surface tension, and Laplace overpressure exists that drives gas out even when the surrounding aqueous gas concentration is saturated [68-69]. On the other hand, gas encased in a solid lipid shell has essentially zero tension in the surface, can persist in this equilibrium state, and so is only constrained by the gas concentration in solution [70]. The change in bubble size is determined by the mass transfer [71], and large bubbles ( $\sim 100 \mu\text{m}$ ) change size relatively slowly due to gas saturation conditions or the Laplace pressure. However, for smaller gas bubbles ( $\sim 10 \mu\text{m}$ ), the Laplace pressure is hundred times larger and the rate of volume change is easily measurable.

An effective way to slow down the dissolution of microbubble is to protect the microbubble with a shell at the gas-liquid interface. The shell may be composed of protein [72], surfactant [73-75], polymer [76], or lipid [9, 77]. The advantage of using amphiphilic molecules as the coating material is that they self-assemble into a monolayer shell around the gas core [78], allowing better control of the shell surface architecture and greater flexibility when adding functional molecules [9]. Recently, it was discovered that phospholipid shells possess echogenic behavior [79-80], and they tend to reseal following surface rupture due to strong hydrophobic forces [81-82]. A lipid shell is also a better acoustic scatterer than a polymer shell because the polymer absorbs more acoustic energy. In general, increasing hydrophobic chain length will make lipid-coated microbubbles more robust [83]. As the lipid monolayer becomes more cohesive with increasing acyl chain length, the permeability of the shell to gases decreases, leading to a more stable bubble. Phospholipid with charged head group such as 1,2-Dipalmitoyl-sn-glycero-3-phosphatidic acid (DPPA) can enhance bubble dispersion. A hydrophilic polyethylene glycol (PEG) emulsifier can also be added to aid lipid dispersion and prevent microbubble coalescence [84]. These coatings can alter the elasticity and viscosity of the microbubble, and thereby change the resonant frequency of the microbubble and dampen the vibration.

Another benefit of attaching PEG chains to the lipid shell is that these sterically stabilized molecules allow the liposome to escape macrophage phagocytosis and prolong circulation [85]. Therefore, the contrast agent material for ROS can be encapsulated inside PEGylated liposome to enhance *in vivo* efficacy. Several commercial FDA-approved microbubble contrast agents are composed of phospholipid shells attached with



PEG chains [86]. Other surface modification allows attachment of specific ligands that promote cell adhesion and targeting. Examples include attachment to activated leukocytes [10, 87-88], integrins [89] and ICAM-1 [90]. In summary, encapsulating the contrast agent inside the liposomes can improve bubble stability and enhance *in vivo* efficacy.

## **2.8 *In vivo* imaging of oxidative stress**

ROS are overproduced in a variety of inflammatory diseases, including atherosclerosis, chronic obstructive pulmonary disease and liver hepatitis [36]. Contrast agents that can image ROS *in vivo* have the potential to significantly impact these areas of medicine and biology [91]. Hence, there is a great interest to determine if ROS imaging can be used as a diagnostic tool for inflammatory diseases. For ultrasound imaging, several studies described the effectiveness of microbubble contrast agents particularly in the liver, spleen, and kidneys [2]. Microbubbles allow assessment of the macrovasculature, the identification and characterization of hepatic and splenic lesions, the depiction of septal enhancement in cystic renal masses, and the quantification of organ perfusion. Even though microbubbles present a pure intravascular distribution, some agents present a post-vascular hepatosplenic specific phase from 2-5 minutes after intravenous injection [92-95]. The site of hepatic accumulation may be within the reticulo-endothelial system. From a clinical perspective, the liver has been the abdominal organ that the contrast agents have provided the most reliable clinical results [2]. Examples include characterization of portal vein patency in cirrhosis and liver

transplantation [96-98], liver lesions [94, 99-101], and hepatocellular carcinoma [99, 102-103].

Previous work in our lab demonstrated *in vivo* imaging of hydrogen peroxide based on a chemi-luminescent contrast agent [36]. In previous studies, a lipopolysaccharide-endotoxin (LPS) was injected into the intraperitoneal cavity of mice to induce inflammatory response, and the overproduction of hydrogen peroxide in the intraperitoneal cavity of mice was imaged *in vivo* using a fluorescence IVIS machine. The onset of inflammatory response and the recruitment of activated macrophages have been studied and confirmed to occur within 24 hours [104]. Therefore, the LPS-induced inflammatory response model could be used for similar studies by ultrasound.

# CHAPTER 3

## CHEMICAL GAS GENERATION INVOLVING RADICAL OXIDANTS

### 3.1 Introduction

The objective of this aim is to evaluate the feasibility of using chemical reactions to generate gas forming molecules in the presence of radical oxidants and detect ROS. The first task is to design and synthesize appropriate molecules that can generate gas molecules in the presence of radical oxidants. The second task is to characterize the chemical reactivity and the oxidation kinetics of the molecule after it has been designed.

There are many chemical reactions that form gas molecules, such as  $H_2$  [105],  $N_2$  [106],  $O_2$  [107],  $CO_2$  [108], disulfide [109] and  $NaBH_4$  [54]. Corey showed that allylic hydrazine can be oxidized by radical oxidants [38], and Sorenson showed that allyldiazenes undergo intramolecular retro-ene reactions to generate nitrogen and propene gas forming molecules [39]. Therefore, we anticipate allylhydrazine and its analogs could be potential molecules for this application. We hypothesize that the reactivity of allylhydrazine with radical oxidants can be enhanced by adding methyl or fluorine group on the C2 position, and attaching long hydrocarbon chain could enhance its *in vivo* efficacy by forming a micelle.

Theoretically, the kinetics of gas forming reaction needs to be faster than the rate of diffusion to exceed the critical threshold needed for bubble nucleation. Hence, the second task is to investigate if allylhydrazine and its analogs can be oxidized by radical oxidants and to determine their oxidation kinetics. The trinitrobenzene sulfonic acid (TNBS) and azinobis-3-ethylbenzothiazoline-6-sulfonic acid (ABTS) assays were used to

characterize the oxidation kinetics of allylhydrazine. The TNBS assay has been used to determine the presence of primary amine in proteins. The ABTS assay is used to determine the rate of oxidation, and hence the kinetics of free radicals reacting with allylhydrazine. This assay is based upon the ability of antioxidants to decolorize the ABTS radical cation.

### **3.2 Materials and Methods**

#### **3.2.1 Allylhydrazine and synthesis of allylhydrazine analogs**

##### Preparation of allylhydrazine

Allylhydrazine • 2 HCl was purchased from ECA International Corporation (Palatine, IL) and neutralized with NaOH to pH ~7.4 prior to use.

##### Synthesis of 2-fluoroallyl-hydrazine

10.00 g (0.043 mol) of N,N'-di-Boc-hydrazine, 11.87 g (2 equiv) of K<sub>2</sub>CO<sub>3</sub>, 6.03 g (3.5 equiv) of NaOH and 1.466 g (0.1 equiv) of TBAHS were dissolved in 160 mL of toluene and 3.9 mL of 2-fluoro-3-chloro-propene (1.05 equiv) dissolved in 15 mL of toluene was added dropwise at 20 mL/hr rate into the reaction mixture. The reaction was conducted at room temperature and stirred overnight. Thin Layer Chromatography (TLC) analysis was used to monitor the formation of product. Toluene was removed by a rotovap and 40 mL of water was added to the mixture and the organic phase was extracted 4 times with 80 mL of EtOAc, dried with Na<sub>2</sub>SO<sub>4</sub> and separated by column

chromatography. The di-*tert*-butyl 1-(2-fluoroallyl)hydrazine-1,2-dicarboxylate was confirmed with  $^1\text{H}$  NMR and mass spectroscopy.

The Boc protecting group was removed by dissolving 1.00 g of di-*tert*-butyl 1-(2-fluoroallyl)hydrazine-1,2-dicarboxylate in 8 mL of HCl (10 equiv) in dioxane and stirred at room temperature overnight. The dioxane was removed by a rotovap and neutralized with NaOH to pH 7.0. The product 2-fluoroallyl-hydrazine was confirmed by  $^1\text{H}$  NMR and mass spectroscopy. **Figure 3.1** provides a brief chemical scheme of the synthesis of 2-fluoro-allylhydrazine.

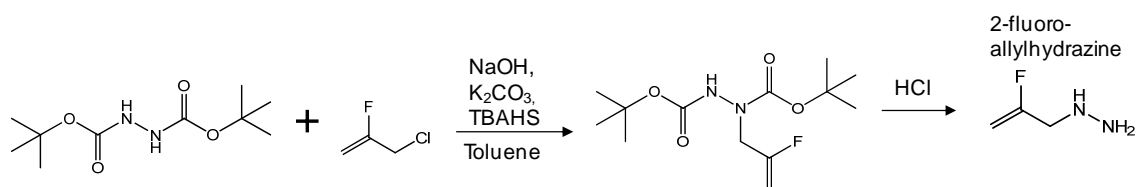


**Figure 3.1.** Chemical synthesis of 2-fluoro-allylhydrazine

#### Synthesis of 2-methylallyl-hydrazine

10.00 g (0.043 mol) of N,N'-di-Boc-hydrazine, 11.87 g (2 equiv) of  $\text{K}_2\text{CO}_3$ , 6.03 g (3.5 equiv) of NaOH and 1.47 g (0.1 equiv) of TBAHS were dissolved in 160 mL of toluene and 4.5 mL of 2-methyl-3-chloro-propene (1.05 equiv) dissolved in 15 mL of toluene was added dropwise at 20 mL/hr rate into the reaction mixture. The reaction was conducted at room temperature and stirred overnight. TLC analysis was used to monitor the formation of product. Toluene was removed by a rotovap and 40 mL of water was added to the mixture and the organic phase was extracted 4 times with 80 mL of EtOAc, dried with  $\text{Na}_2\text{SO}_4$  and separated by column chromatography. The di-*tert*-butyl 1-(2-

methylallyl)hydrazine-1,2-dicarboxylate was confirmed with  $^1\text{H}$  NMR and mass spectroscopy.

The Boc protecting group was removed by dissolving 1.00 g of di-*tert*-butyl 1-(2-methylallyl)hydrazine-1,2-dicarboxylate in 8 mL of HCl (10 equiv) in dioxane and stirred at room temperature overnight. The dioxane was removed by a rotovap and neutralized with NaOH to pH 7.0. The product 2-methyl -hydrazine was confirmed by  $^1\text{H}$  NMR and mass spectroscopy.

#### Synthesis of (Z)-dec-2-enylhydrazine

*Trans* 1-bromo-2-decene was synthesized from 15 mL of *trans*-2-decen-1-ol dissolved in DCM, cooled in an ice bath and stirred for 10 min. 8.73 g (0.4 equiv) of  $\text{PBr}_3$  was dissolved in 10 mL of DCM and added dropwise using a syringe pump and stirred for 6 hours. The reaction was quenched with saturated  $\text{NaHCO}_3$  in aqueous solution and stirred for 30 minutes. The reaction mixture was extracted 4 times with 50 mL of DCM and purified on a column chromatography.

5.30 g (0.043 mol) of N,N'-di-Boc-hydrazine, 6.25 g (2 equiv) of  $\text{K}_2\text{CO}_3$ , 3.20 g (3.5 equiv) of NaOH and 0.78 g (0.1 equiv) of TBAHS were dissolved in 80 mL of toluene and 5.00 g of *trans*-1-bromo-2-decene (1.05 equiv) dissolved in 5 mL of toluene was added dropwise at 20 mL/hr rate into the reaction mixture. The reaction was conducted at room temperature and stirred overnight. TLC analysis was used to monitor the formation of product. Toluene was removed using a rotovap and 40 mL of water was added to the mixture and the organic phase was extracted 4 times with 80 mL of EtOAc, dried and separated by column chromatography. The di-*tert*-butyl 1-(dec-2-en-1-

yl)hydrazine-1,2-dicarboxylate was confirmed with  $H^1$  NMR and mass spectroscopy. The Boc protecting group was removed by dissolving 1.00 g of di-*tert*-butyl 1-(dec-2-en-1-yl)hydrazine-1,2-dicarboxylate in 8 mL of HCl (10 equiv) in dioxane and stirred at room temperature overnight. The dioxane was removed by a rotovap and neutralized with NaOH to pH 7.0. The (Z)-dec-2-enylhydrazine was confirmed by  $H^1$  NMR and mass spectroscopy.

### 3.2.2 Trinitrobenzene sulfonic acid (TNBS) assay

Briefly, to 1 mL of allylhydrazine (25  $\mu$ M) aqueous solution, were added 1 mL of 4%  $NaHCO_3$  (pH 8.5). The mixture is incubated in a water bath at 42°C for 10 minutes. Next, 1 mL of 0.01% (341  $\mu$ M) freshly made TNBS was added to the mixture and incubated at 42°C for 2 hours followed by the addition of 1 mL 10% SDS and 0.5 mL of 1N HCl. The absorbance was monitored at 335 nm, after appropriate blank corrections. The blank correction is prepared through the same procedure except that the concentrated HCl is added to the allylhydrazine solution prior to the addition of the TNBS reagent.

To 5 mL of 25  $\mu$ M allylhydrazine solution was added 50  $\mu$ L of 100 mM  $Fe^{2+}$  and 50  $\mu$ L of 100 mM  $H_2O_2$  solution. This constitutes final concentration of 1 mM hydroxyl radicals. The mixture is allowed to react for 1 hour, and the sample is subjected to TNBS assay as described earlier. For blank correction, 1 mM ROS solution is prepared in DI water without addition of allylhydrazine. **Figure 3.2** shows how TNBS reacts with allylhydrazine and produced an absorbance at 335 nm.

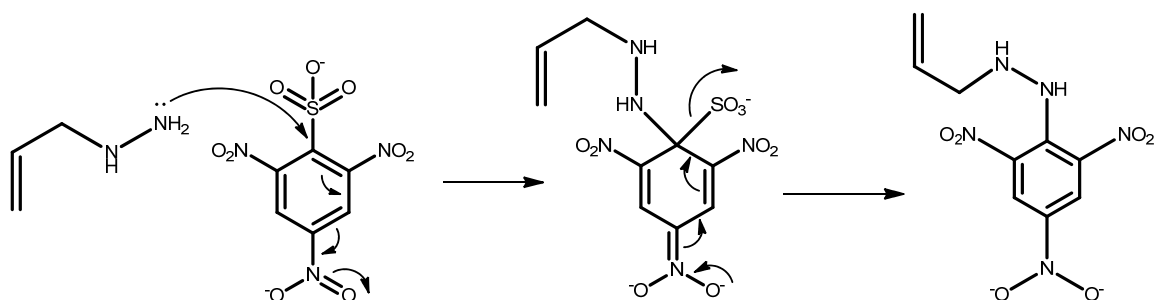


**Figure 3.2.** Reaction of trinitrobenzene sulfonic acid (TNBS) with primary amine on allylhydrazine

### 3.2.3 ABTS assay

Briefly, stock solutions of ABTS (5 mM) and sodium persulfate (68.9 mM) in PBS (pH = 8.0) were prepared. Sodium persulfate stock solution (1 mL) was added to ABTS stock solution (99 mL). The mixture was stored in the dark for 16 hours. This produced a solution of ABTS $\bullet$ + which gave an absorbance of approximately 0.85 at 734 nm. 10 mL stock solutions of neutralized allylhydrazine (pH = 7.0-7.5) were prepared, and several dilutions (10  $\mu$ M, 100  $\mu$ M, 1 mM, 10 mM) were prepared from the stock solution. Filtered DI water was used for all dilution, and all measurements were done at room temperature (20°C). The control is prepared by adding ABTS $\bullet$ + to DI water only (containing no allylhydrazine), and no decrease in absorbance was observed. Negative control is prepared by ABTS solution without sodium persulfate (hence no ABTS $\bullet$ + radical). The absorbance of ABTS solution plus allylhydrazine is nearly zero, indicating ABTS itself does not react with allylhydrazine.

For kinetic measurement, 2 mL of allylhydrazine sample was added to a cuvette, and the absorbance was set to baseline. Next 1 mL of ABTS $\bullet$ + solution was rapidly added to the cuvette and the absorbance reading at 734 nm was taken every second for 5 minutes. The test was repeated four times for each dilution of allylhydrazine. Data was exported to Excel and absorbance versus time graphs were generated. Rate constants



were determined from the slope of the plots, and half-life was determined using the formula  $T_{1/2} = \ln 2/k$ . **Figure 3.3** shows the structure of 2,2'-azinobis-3-ethylbenzothiazoline-6-sulfonic acid radical cation (ABTS<sup>•+</sup>), and it has an absorbance maximum of 734 nm. ABTS<sup>•+</sup> is generated by reaction of ABTS with an oxidizing species.

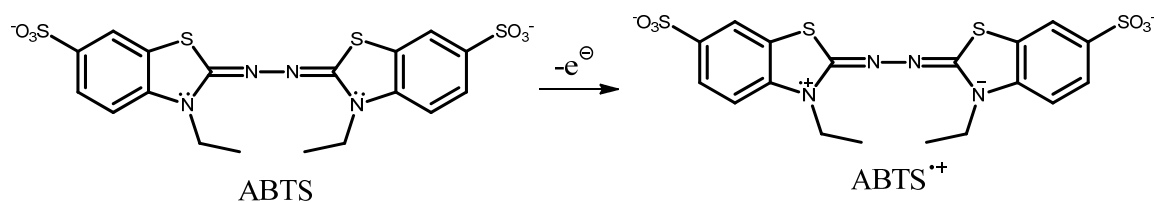


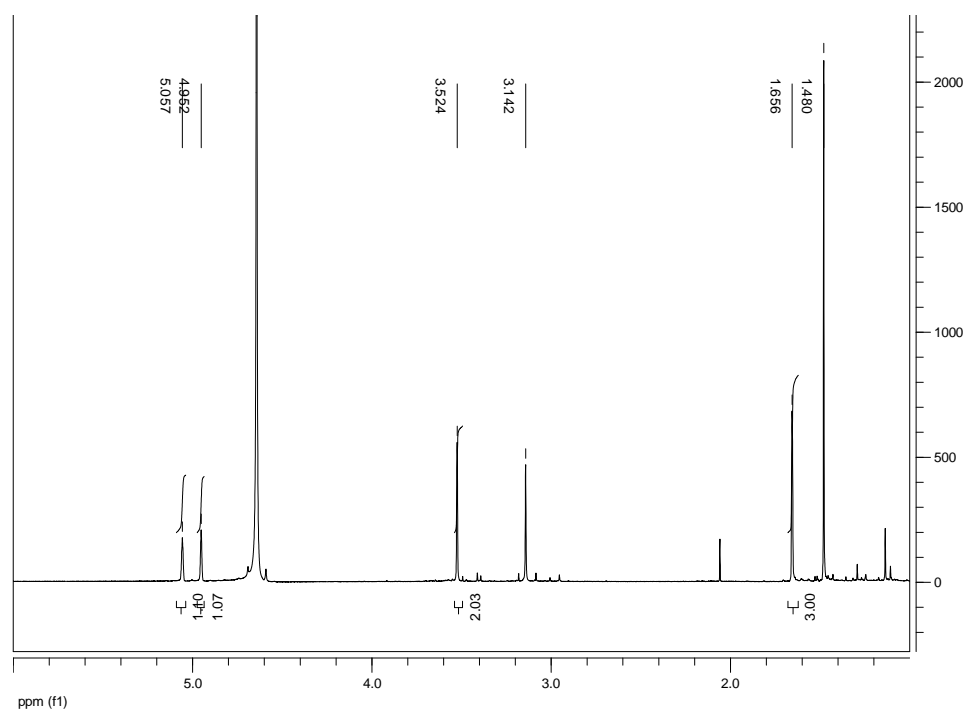
**Figure 3.3.** Structure of 2,2'-azinobis-3-ethylbenzothiazoline-6-sulfonic acid (ABTS)

### 3.3 Results

#### 3.3.1 Synthesis of allylhydrazine analogs

The chemical synthesis was confirmed by proton  $H^1$  NMR and mass spectrometry.

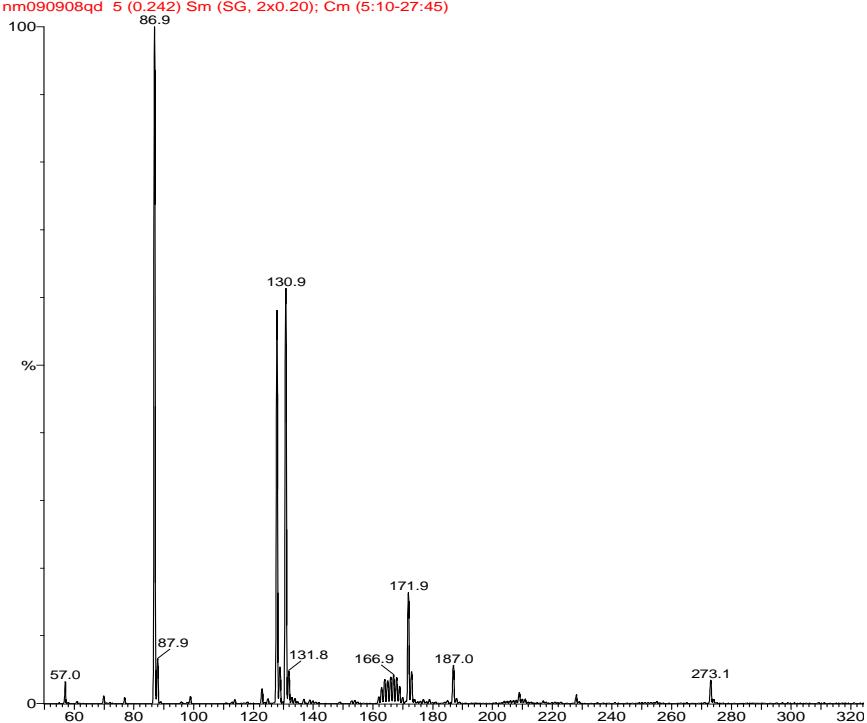
# $H^1$ NMR of 2-methyl-allylhydrazine in methanol-D4 and mass spectrometry data



## GT Mass Spectrometry Laboratory

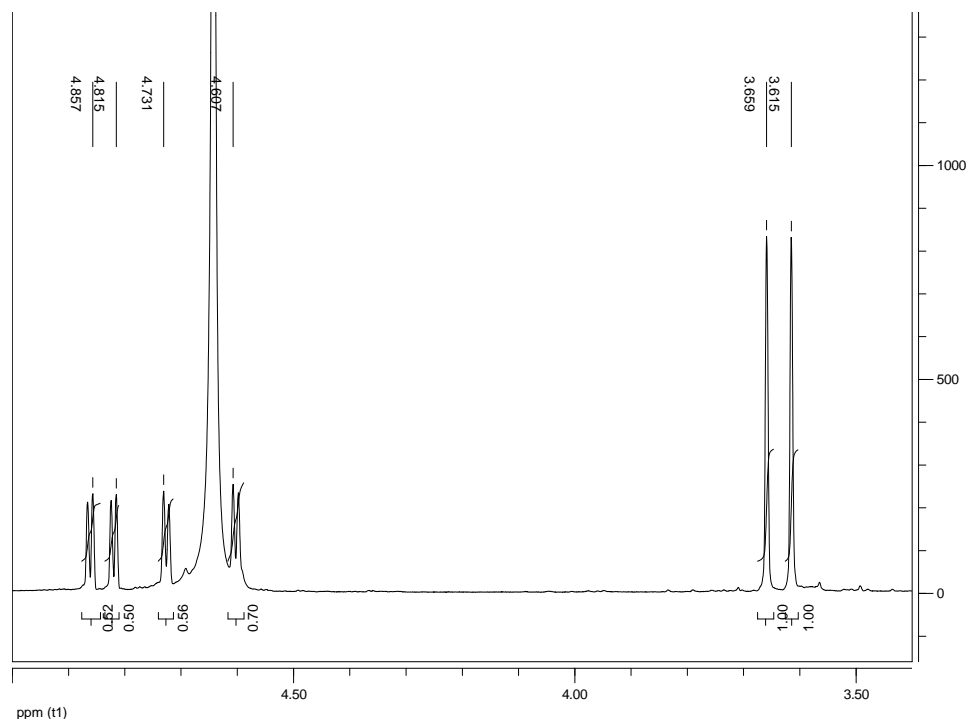
nm090908qd 5 (0.242) Sm (SG, 2x0.20); Cm (5:10-27:45)

## Perng methyl allyl hydrazine



2-methyl-allylhydrazine MW+H = 87

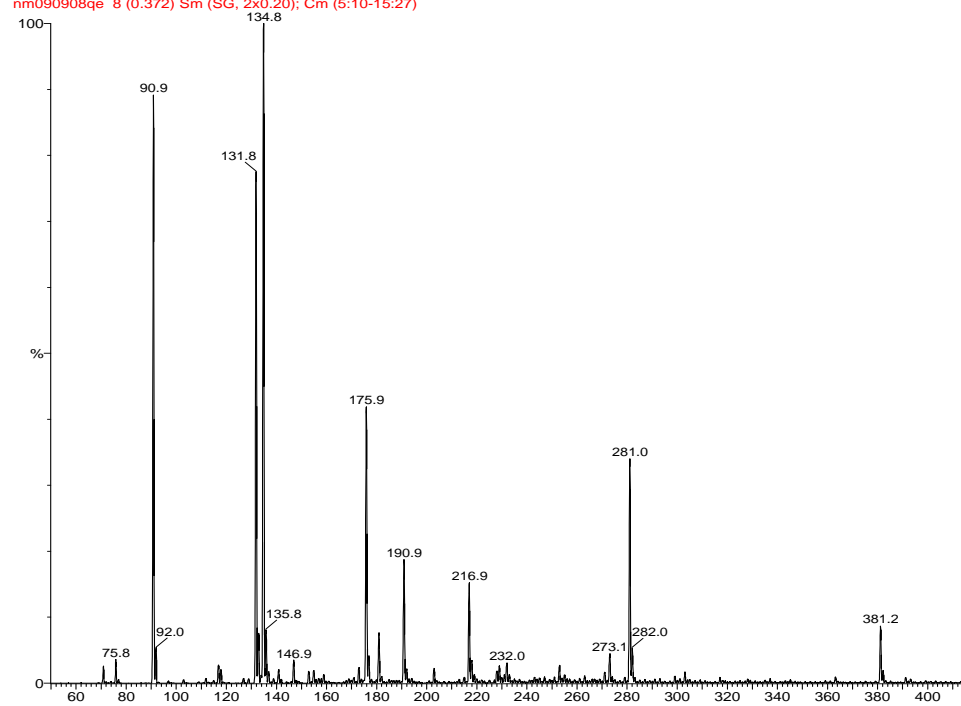
# $^1\text{H}$ NMR of 2-fluoro-allylhydrazine in methanol- $\text{D}_4$ and mass spectrometry data



GT Mass Spectrometry Laboratory

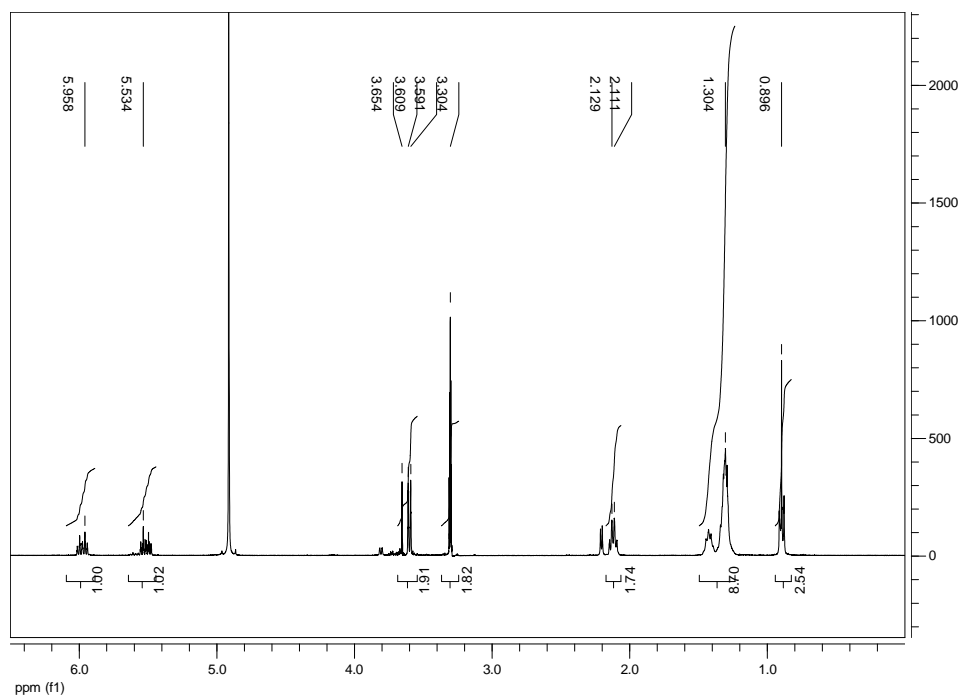
Perng fluoro allyl hydrazine

nm090908qe 8 (0.372) Sm (SG, 2x0.20); Cm (5:10-15:27)



2-fluoro-allylhydrazine  $\text{MW} + \text{H} = 91$

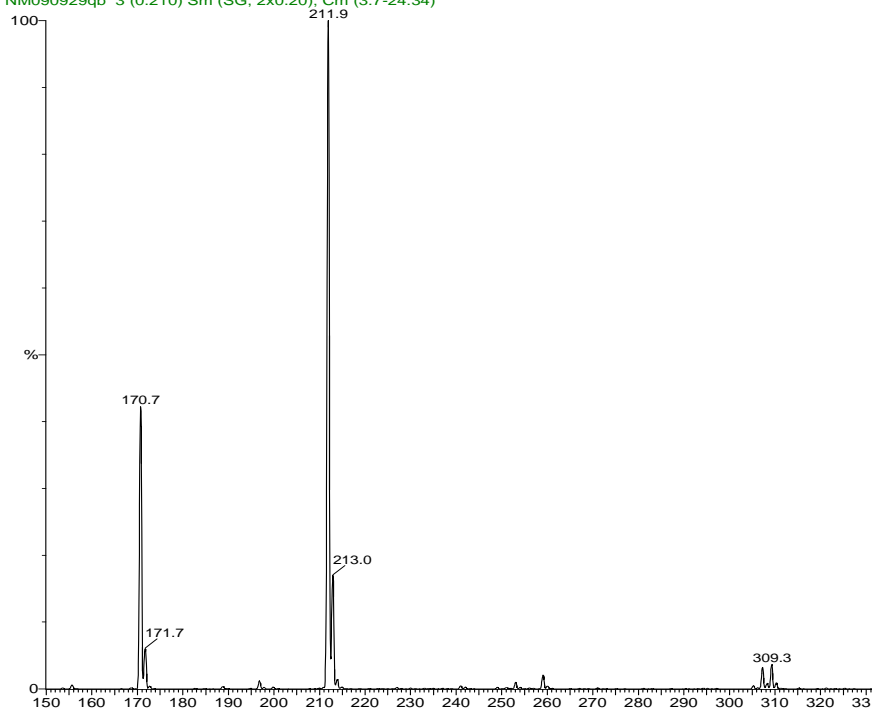
# $^1\text{H}$ NMR of (Z)-dec-2-enylhydrazine in methanol- $\text{D}_4$ and mass spectrometry data



## GT Mass Spectrometry Laboratory

## Perng C7-hydrazine

NM090929qb 3 (0.210) Sm (SG, 2x0.20); Cm (3:7-24:34)



(Z)-dec-2-enylhydrazine  $\text{MW} + \text{H} = 171$

### 3.3.2 Oxidation of allylhydrazine with the hydroxyl radical

We further verified that allylhydrazine can react with a physiological radical oxidant, the hydroxyl radical. Allylhydrazine (25  $\mu\text{M}$ ) was incubated with an excess of hydroxyl radical (10 mM  $\text{H}_2\text{O}_2$  + 10 mM  $\text{Fe}^{2+}$ ) for 1 hour and the depletion of allylhydrazine was determined using the trinitrobenzene sulfonic acid (TNBS) assay [110]. **Figure 3.4** demonstrates that allylhydrazine is decomposed by radical oxidants into a product that has no reactivity with TNBS, presumably nitrogen and propene. TNBS assay of allylhydrazine (25  $\mu\text{M}$ ) generates an absorption peak at 335 nm (blue dash curve). TNBS assay of allylhydrazine (25  $\mu\text{M}$ ) incubated with an excess of hydroxyl radicals (10 mM  $\text{H}_2\text{O}_2$  +  $\text{Fe}^{2+}$ ) for 1 hour, does not generate an absorption peak at 335 nm, indicating the reaction of allylhydrazine (red curve). Based on the results of the oxidation kinetics of allylhydrazine, we assumed that the other allylhydrazine analogs have similar kinetics and were subsequently investigated by acoustic characterization for bubble generation in Chapter 4.

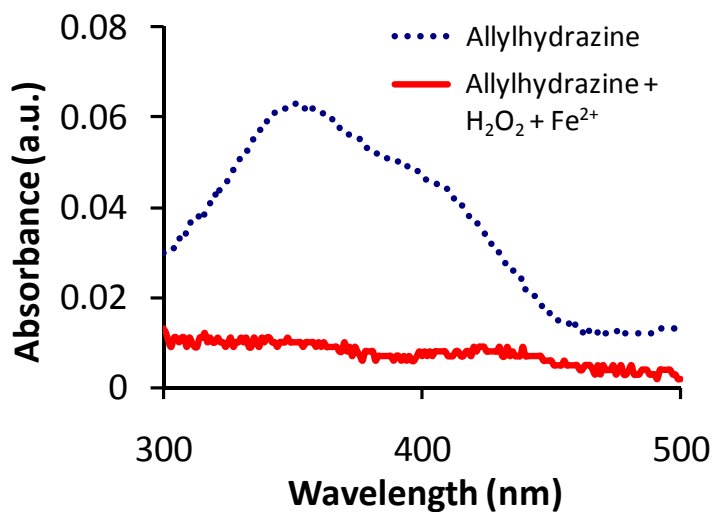


**Figure 3.4.** Allylhydrazine reacts with the hydroxyl radical and is decomposed into a product that has no reactivity with TNBS

### 3.3.3 Oxidation kinetics of allylhydrazine with radical oxidants

**Figure 3.5** demonstrates that allylhydrazine reacts rapidly with radical oxidants. ABTS radical cation has a constant absorbance at 734 nm (dash line). ABTS radical cation (230  $\mu\text{M}$ ) is reduced by excess allylhydrazine (6.6 mM) and loses its absorbance (red curve), with a half-life of  $3.06 \pm 0.0045$  seconds and a pseudo first-order rate constant (k) of  $0.23 \pm 0.0003 \text{ s}^{-1}$  (n = 3).

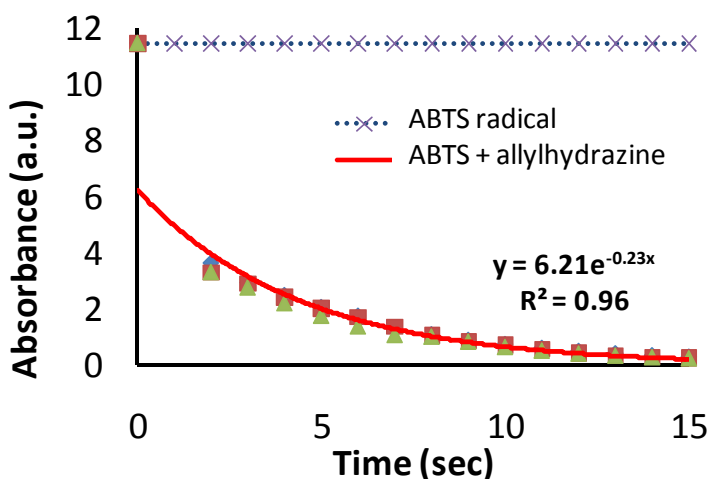


**Figure 3.5.** The absorbance of ABTS assay shows that allylhydrazine reacts rapidly with radical oxidants

## 3.4 Discussion

### 3.4.1 Oxidation kinetics and implication for clinical applications

Allylhydrazine is designed to nucleate gas bubbles in the presence of radical oxidants as shown in **Figure 3.6**. In order to exceed the critical threshold needed for bubble nucleation, the allylhydrazine needs to oxidize rapidly in comparison to the rate of nitrogen diffusion. We therefore investigated the oxidation kinetics of allylhydrazine

with the ABTS, a radical cation that is reduced by single electron oxidation of its substrates [111]. **Figure 3.5** demonstrates that allylhydrazine reacts rapidly with radical oxidants with a pseudo first-order rate constant ( $k$ ) of  $0.23 \pm 0.0003 \text{ s}^{-1}$ , which is consistent with literature values [44]. To compare this result under physiological conditions, we calculated the Thiele modulus,  $\Phi$ , which is a dimensionless number that quantifies the ratio of reaction time to diffusion time, and a value greater than one indicates that the reaction rate is faster than the rate of diffusion [112]. The Thiele modulus is given by the equation:  $\phi = \sqrt{\frac{kL^2}{D}}$  where  $k$  is the first-order rate constant ( $\text{s}^{-1}$ ),  $L$  is the length (m) and  $D$  is the diffusion constant ( $\text{cm}^2/\text{s}$ ). Assuming a 1 mm length of ROS-producing tissue, a rate constant  $k$  of  $0.23 \text{ s}^{-1}$  and a nitrogen diffusion constant of  $2.83 \times 10^{-5} \text{ cm}^2/\text{s}$ , the Thiele modulus was calculated to be 9. Therefore, the rate of nitrogen gas generated by allylhydrazine should be substantially faster than the rate of nitrogen gas diffusion [113], leading to accumulation of nitrogen gas in ROS-producing tissue. This suggests that allylhydrazine has the reactivity needed to nucleate bubbles *in vivo*.

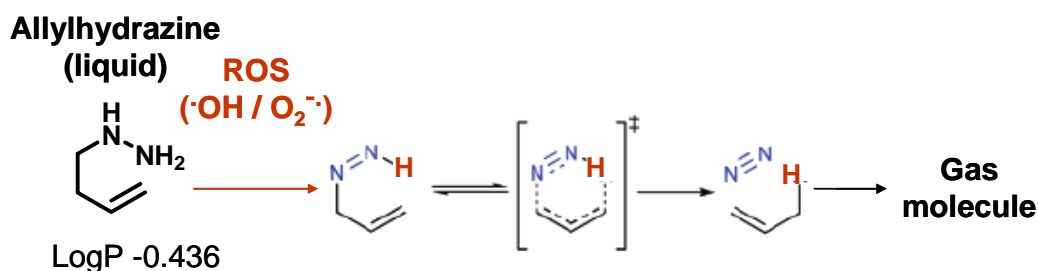


**Figure 3.6.** Generation of gas molecules from the reaction of allylhydrazine with radical oxidants

### 3.4.2 Theoretical prediction for threshold of bubble nucleation

The hydroxyl radical ( $\cdot\text{OH}$ ) was chosen because it is the most abundant radical oxidants in the body, and the major source of hydroxyl radicals in the body mainly derived from hydrogen peroxide ( $\text{H}_2\text{O}_2$ ). Studies suggest that physiological concentrations of hydrogen peroxide are in the nanomolar to micromolar range [114]. Based on this information, we estimated the amount of nitrogen gas that can be generated from hydrogen peroxide:

$$1 \text{ mol of gas} = 22.4 \text{ L (under STP condition)}$$

$$\text{Hydrogen peroxide level: } 1 \text{ nM} - 1 \mu\text{M}$$

Assuming complete reaction of allylhydrazine with the hydroxyl radical ( $\cdot\text{OH}$ ), we determine that:

$$\text{Volume of a single bubble for various bubble sizes } (V = \frac{4}{3}\pi r^3)$$

Diameter of bubble	1um	10um
Volume of single bubble (L)	$5.24 \times 10^{-19}$	$5.24 \times 10^{-13}$

Number of bubbles present in 1mL solution for various hydroxyl radical concentrations and bubble sizes

	Total volume of gas	Number of bubbles (1um diameter)	Number of bubbles (10um diameter)
1uM ( $\cdot\text{OH}$ )	$22.4 \times 10^{-9} \text{ L}$	$4.28 \times 10^{10}$	$4.28 \times 10^4$
1nM ( $\cdot\text{OH}$ )	$22.4 \times 10^{-12} \text{ L}$	$4.28 \times 10^7$	42.8

The theoretical estimation of the amount of gas bubbles that can be generated serve as a reference for the detection limit of ultrasound. The ultrasound detection of bubble nucleation will be investigated in Chapter 4.



## **CHAPTER 4**

### **ULTRASOUND DETECTION OF BUBBLE NUCLEATION**

#### **4.1 Introduction**

Ultrasound is extremely sensitive to gas bubbles and can detect picoliter volume of gas bubbles due to their compressibility and the acoustic impedance mismatch between the gas and the liquid. In this section, we investigated ultrasound detection of bubble nucleation generated from the oxidation of allylhydrazine by radical oxidants. The first task was to examine if the oxidation of allylhydrazine by the hydroxyl radical could chemically generate gas bubbles, using a custom-built system that can simultaneously visualizes gas bubbles and measures their acoustic properties. We showed that bubbles were observed optically and characterized the acoustic signals of the bubbles. The second task was to investigate the acoustic response of bubble nucleation and to study the effects of ultrasound parameters on bubble nucleation. We determined if bubble nucleation can be enhanced by ultrasound. A key parameter determining the feasibility of using chemically-generated microbubbles for ROS imaging is the sensitivity of ultrasound to detect gas molecules above saturation in aqueous solutions. Therefore, we will also investigate the limit of ultrasound, and determine the linear range of hydroxyl radical concentrations that can be detected by ultrasound. Lastly, we will determine if bubble nucleation can be detected *in vitro* using a clinical ultrasound system and correlate the video intensity of the ultrasound image with the hydroxyl radical concentrations.

## 4.2 Materials and Methods

### 4.2.1 Optical observation and acoustic characterization of bubble nucleation

A custom-built optical and acoustic measuring system was developed that can simultaneously visualize bubble nucleation and characterize its acoustic properties (**Figure 4.1**). A solution containing 100 mM allylhydrazine and 1 mM hydroxyl radical ( $\text{H}_2\text{O}_2 + \text{Fe}^{2+}$ ) was pre-mixed in a syringe and injected into a 200  $\mu\text{m}$ -diameter cellulose tube at a controlled flow rate. The tube was also placed at the focal region of the transducer, and interrogated with 1.5 cycle pulses at a 2.25 MHz center frequency with an 80 Hz pulse repetition frequency. The tube was immersed in degassed water and the temperature is set to 37°C. The cellulose tube was placed under a microscope stage linked to a digital camera for optical observation of bubble nucleation. The acoustic data was acquired with an oscilloscope and processed off-line by a computer.

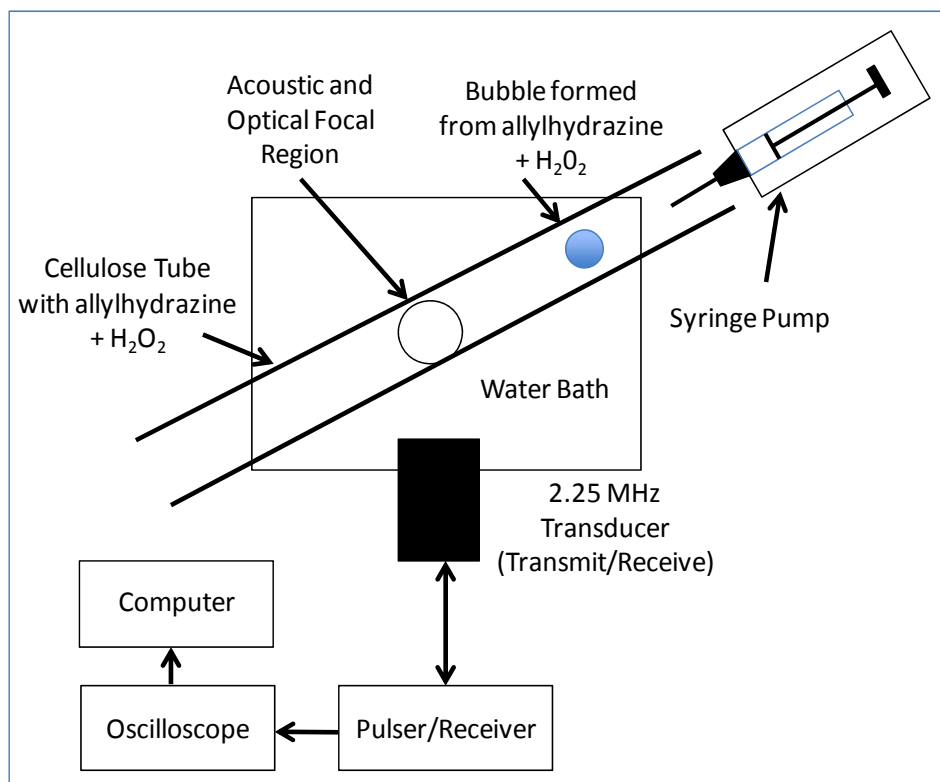


**Figure 4.1.** Measuring system for simultaneous optical observation and acoustic characterization of bubble nucleation.

#### 4.2.2 Ultrasound characterization system

A custom-built ultrasound testing system for *in vitro* characterization of allylhydrazine with the hydroxyl radical is shown in **Figure 4.2**. Ultrasound was produced by a single element flat 2.25 MHz transducer with 0.5" element diameter, and a near field distance of 6 cm. The signal is generated from a HP32250A arbitrary waveform generator and amplified through an ENI 320L RF power amplifier. The ultrasound pulse was generated at 2.075 MHz, 400 mVpp, 10 ms pulse repetition period, 20 cycle pulses and amplified 50 dB by the RF power amplifier. The output signal was calibrated with the hydrophone to ensure operation in the linear region and the output pressure was 0.4 MPa. The ultrasound signal was detected with a calibrated hydrophone.

The hydrophone is connected to a 20 dB gain preamplifier, and the hydrophone sensitivity is 6.2 Vpp/MPa with the preamplifier, and 0.12 Vpp/MPa without the preamplifier. The received signal from the hydrophone is sent to a HP DSO5014A digital oscilloscope and the waveform is transferred to the computer through a GPIB cable.

The contrast agent was placed in a container with acoustically transparent membrane. The holder has a dimension of 59 mm (H) x 60 mm (W) x 10 mm (D), and able to hold 10 mL of solution. For ultrasound testing, the transducer is placed 6 cm in front of the holder at 45° angle, and the hydrophone is placed 3 cm behind the holder at 45° angle. Thus, the transducer is at a 90° angle with respect to the hydrophone. This is done to minimize signal transmitted directly from the transducer. The transducer, hydrophone and holder are positioned and fixed with clamps. The water tank has a dimension of 13' (L) x 12' (W) x 1.5' (D).

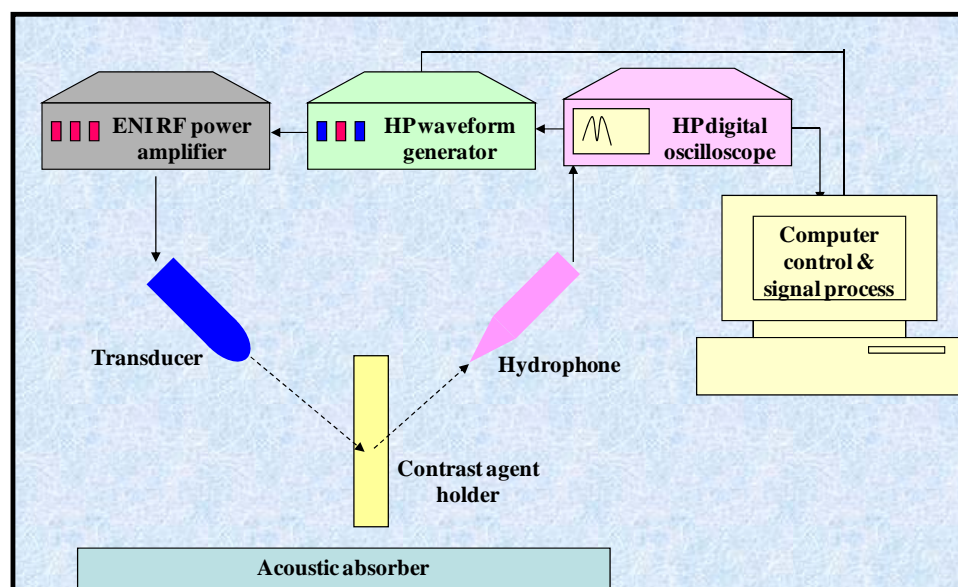


**Figure 4.2.** Ultrasound measurement system for *in vitro* characterization of allylhydrazine with the hydroxyl radical

A Matlab interface was used to control the center frequency, pulse amplitude, input signal offset, burst period, number of cycles, sampling rate, and number of FFT average (**Figure 4.3**). The received echoes were processed with Fast Fourier Transform (FFT) at 100 MHz sampling frequency, and the result of 20 FFT samples were averaged and displayed.

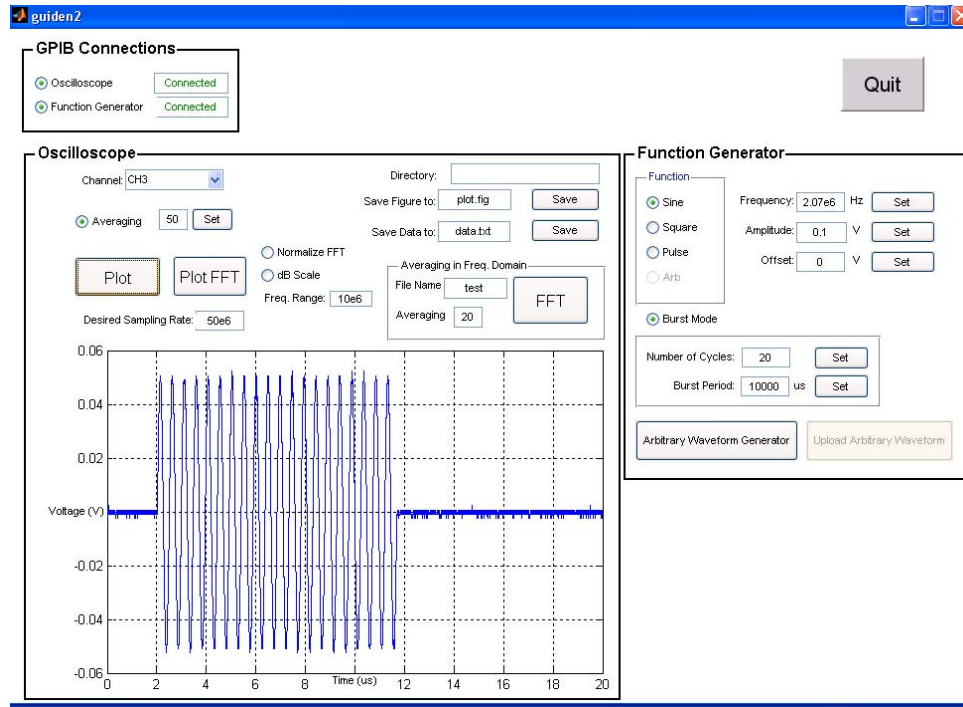


**Figure 4.3.** Matlab user interface for displaying data acquisition and setting ultrasound parameters.

#### 4.2.3 Optimization of ultrasound parameters

Several different pulse sequences were used to investigate the effect of ultrasound parameters on bubble nucleation, including compression-first sinusoidal waves, pulse-inversion waveform and rectified-diffusion corrected waveform. Both focused and unfocused transducers with frequencies ranging from 1 MHz, 2.25 MHz, 5 MHz and 10

MHz were used. The pulse repetition period was varied from 10 Hz to 100 Hz, and the burst period was set to 10 ms but the cycle length was varied from 1-80 cycles. The acoustic pressure was varied from 100 kPa to 2 MPa, and was calibrated by the hydrophone prior to testing. **Table 1** lists the parameters that were explored.

<b>Table 1. Ultrasound parameters that can affect bubble acoustic response</b>	
Ultrasound parameter	Setting
Frequency	1MHz, 2MHz, 5MHz, 10MHz
Peak negative pressure	100kPa, 400kPa, 1MPa, 2MPa
Pulse sequence	Sinusoidal, pulse inversion, rectified-diffusion corrected
Pulse cycle length	1, 1.5, 10, 20, 40, 60, 80 cycles
Pulse repetition period	10, 30, 50, 100Hz
Transducer type	Focused, unfocused

For signal processing, the number of sample averaged by FFT was varied from 20 samples to 50 samples. The region of interest (ROI) was chosen to eliminate unwanted reflections from the wall of the container. The ultrasound parameters were optimized by determining the parameters that result in the greatest change in ultrasound intensity (fold increase) within 10 minutes.

#### **4.2.4 *In vitro* ultrasound characterization of allylhydrazine with the hydroxyl radical**

*In vitro* acoustic characterization of bubble nucleation was done using non-degassed deionized water at 37°C to mimic physiological condition *in vivo*. However, the water tank is filled with degassed deionized (DI) water (except inside the contrast agent holder) to minimize background noise, and the water temperature is controlled by an immersible heater capable of controlling the temperature within +/- 1°C.

The water bath is replaced with fresh degassed DI water each day prior to ultrasound testing. Ten milliliters of filtered non-degassed DI water was added into the holder through a syringe via a 16 gauge needle. The signal was measured and recorded as the baseline. Any abnormality would be noticed here, such as any free gas bubble already present in the holder. Free gas bubble was removed by repeated sonication in sonication bath, until the baseline returns to the noise level. Next, 1 mL of DI water was taken out of the solution through the syringe and 1 mL of (1 M) allylhydrazine solution was added and allowed to mix by diffusion. Then 2 mL of contrast agent solution is taken out from the holder, and 1 mL of H<sub>2</sub>O<sub>2</sub> stock solution and 1 mL of (10 mM) Fe<sup>2+</sup> stock solution was added. Immediately after the injection of H<sub>2</sub>O<sub>2</sub> and Fe<sup>2+</sup>, the signal was measured and recorded at time points: 0, 1, 3, 5, 7, 10, 15 and 20 minutes. The test was repeated at various H<sub>2</sub>O<sub>2</sub> concentrations from 1 μM to 1 mM, with fixed concentration of Fe<sup>2+</sup> at 1 mM. DI water was used instead of H<sub>2</sub>O<sub>2</sub> as the control for no radical oxidants. The test was repeated to obtain 4 data sets for each H<sub>2</sub>O<sub>2</sub> concentration, and the result of ultrasound intensity versus H<sub>2</sub>O<sub>2</sub> concentration was plotted with standard error for each time point.

#### **4.2.5 *In vitro* characterization with clinical ultrasound system**

A Siemens Antares clinical ultrasound machine was used to image bubble nucleation inside the holder. Allylhydrazine was placed inside the custom-made acoustic holder and various concentrations of hydroxyl radicals were used: 1 μM, 10 μM, 100 μM. Deionized water was used as the control for no radical oxidants.

**Figure 4.4** shows the *in vitro* system for imaging bubble nucleation with the Siemens clinical ultrasound probe. The ultrasound probe is placed in front of the acoustic opening in the water bath container, and the acoustic gel is applied at the interface between the ultrasound probe and the acoustic window. Hot water running through a copper heat coil was used to maintain the water temperature at 37°C. An acoustic absorber was placed behind the contrast agent holder to minimize standing wave and reflection. Briefly, 10 mL of 100 mM allylhydrazine solution was prepared inside the holder. Then, 2 mL of solution was taken out with a syringe and replaced with 1 mL of  $\text{Fe}^{2+}$  (1 mM) and 1 mL of  $\text{H}_2\text{O}_2$  at various concentrations into the holder. The video intensity was recorded before and after the addition of  $\text{Fe}^{2+}$  and  $\text{H}_2\text{O}_2$  solution at time points from 0, 1, 3, 5, 7, 10, 12 to 15 minutes.



**Figure 4.4.** In vitro characterization system of bubble nucleation using clinical ultrasound system (A) Side view.



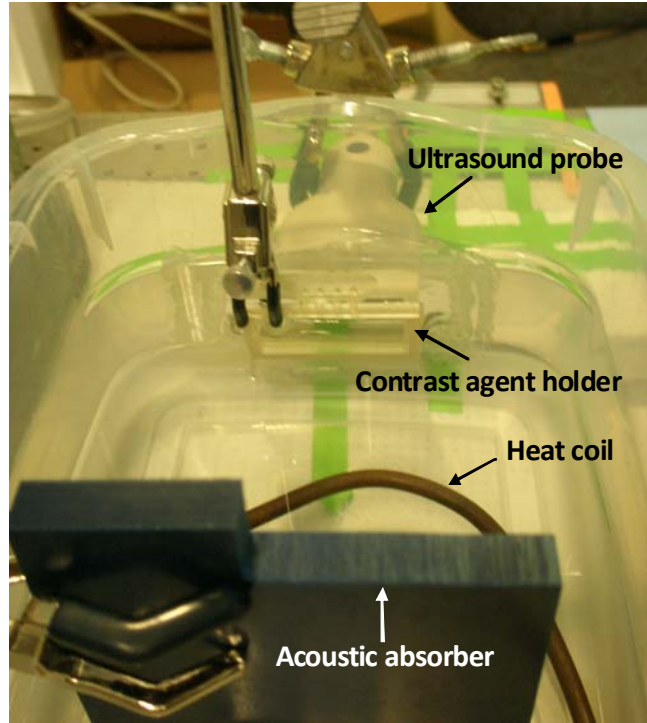


**Figure 4.4.** (B) Top view

The clinical ultrasound setting was 5.71 MHz transmitted frequency,  $MI = 1.5$  (3.58 MPa peak negative pressure), 6 cm depth, and 50 dB receiving gain. **Figure 4.5** illustrates the video intensity of the holder recorded on the screen. The probe is on the top, and the middle two lines are the boundary of the holder membrane. The region of interest is between the boundaries marked by the red box.

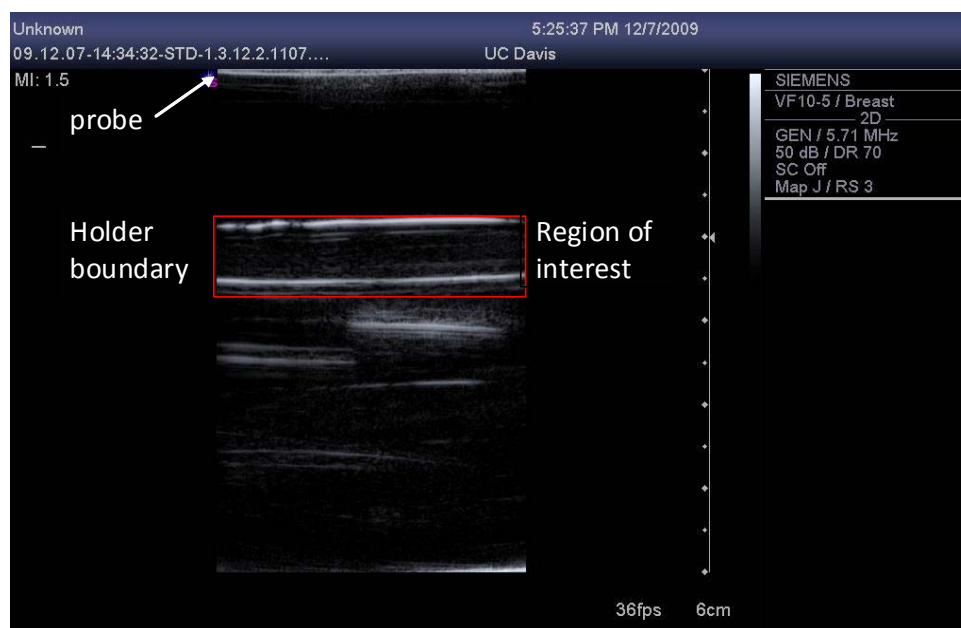


**Figure 4.5.** Representative ultrasound image showing the region of interest

The experiments were repeated in triplicate at each concentrations of the hydroxyl radical and image analysis was performed using the ImageJ software to quantify the change in video intensity. The background signal was subtracted from the image as illustrated in **Figure 4.6**. The result of change in mean video intensity versus time for each  $\text{H}_2\text{O}_2$  concentration was plotted.

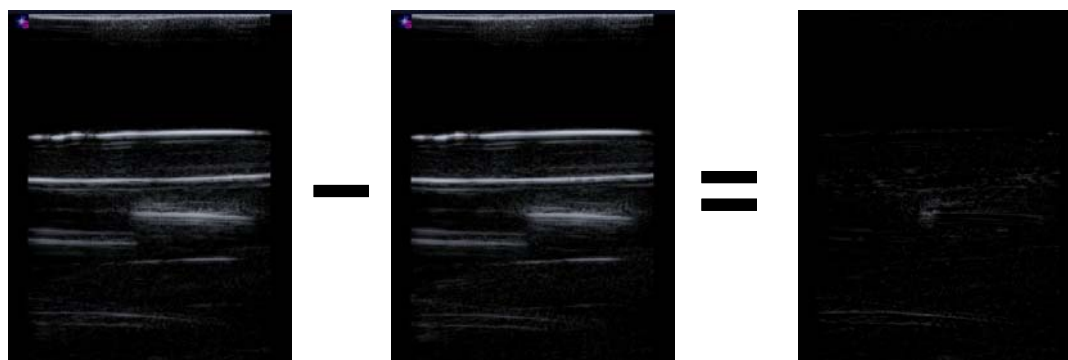


**Figure 4.6.** Background subtraction of ultrasound video images

## 4.3 Results

### 4.3.1 Optical confirmation of bubble nucleation

We examined if the oxidation of allylhydrazine by the hydroxyl radical could chemically generate gas bubbles, using a custom-built system that simultaneously visualizes gas bubbles and measures their acoustic properties. For these experiments, a 100 mM allylhydrazine solution containing a 1 mM hydroxyl radical concentration was injected into a 200  $\mu\text{m}$ -diameter cellulose tube and then imaged. **Figure 4.7** demonstrates that allylhydrazine can nucleate bubbles in the presence of hydroxyl radicals. **Fig. 4.7** frame 1 shows an image of the cellulose tube containing deionized water, and has no evidence of bubble formation. In contrast, after injecting allylhydrazine and Fenton's reagent into the cellulose tube, bubbles became optically visible. For example, **Figures 4.7** frames 2-4 show a bubble flowing through the cellulose tube generated from the oxidation of allylhydrazine with the hydroxyl radical. Chemically generated gas bubbles were also observed at lower hydroxyl radical concentrations (100  $\mu\text{M}$ ), albeit at a slower rate.

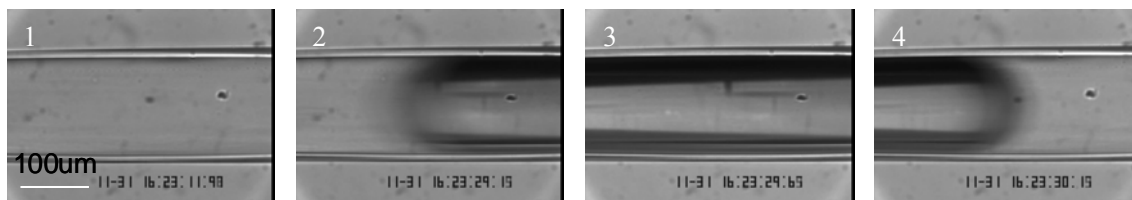


**Figure 4.7.** Video images of the cellulose tube showing that allylhydrazine can nucleate gas bubbles in the presence of the hydroxyl radical. There was no evidence of bubble formation inside the cellulose tube prior to the hydroxyl radical injection (1). After the injection, gas bubbles became visible inside the cellulose tube, and video images (2-4) demonstrate a single gas bubble flowing through the cellulose tube.

We further investigated if the gas bubbles generated from the oxidation of allylhydrazine by the hydroxyl radical could be detected acoustically. **Figure 4.8** demonstrates that strong acoustic echoes are generated from a microbubble identified by optical observation (55-58  $\mu$ s). For example, the microbubble identified in **Figure 4.7** frames 2-4 displayed a 20 fold increase in acoustic signal intensity in comparison to adjacent fluid at 2.25 MHz frequency using a 0.5” diameter transducer at a distance of 5.1 cm. These results suggest that allylhydrazine has the potential for imaging ROS.

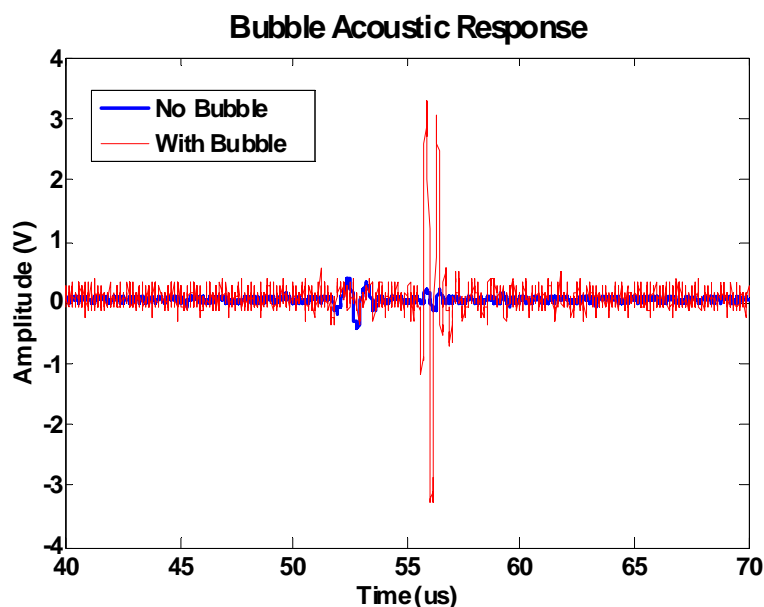


**Figure 4.8.** The microbubble identified by optical observation inside the cellulose generated a strong acoustic echo (55 – 58  $\mu$ s). The microbubble displayed a 20 fold increase in acoustic signal intensity compared to adjacent fluid.

#### 4.3.2 Optimization of ultrasound parameters

We found that the focused transducer produced more energy but was limited to a smaller excitation region. Higher frequency produced better spatial resolution, but suffered from shorter penetration depth and weaker signal. The output of the transducer

became saturated above 400 kPa peak negative pressure. Pulse inversion and rectified-diffusion enhanced waveform did not generate significant difference compared with sinusoidal waveform. Using pulse cycle length greater than 80 cycle pulses resulted in multiple reflections and the returned signals became convoluted. However, using cycle length shorter than 10 cycles resulted in a very weak returned signal. A 100 Hz pulse repetition frequency was sufficient for the returned signal to attenuate completely before the next pulse and reducing the FFT average from 50 samples to 20 samples produced similar results. The optimal ultrasound parameters for a 2.25 MHz unfocused transducer are 400 kPa acoustic pressure, sinusoidal waveform, 20 cycle pulse length, and 100Hz pulse repetition period.

#### **4.3.3 Acoustic response of allylhydrazine with the hydroxyl radical**

The acoustic responses of allylhydrazine before and after the addition of the hydroxyl radical are shown in **Figures 4.9** and **4.10**. **Figure 4.9a** shows the received ultrasound echoes in the time domain, and the region of interest (ROI) between 40 – 80  $\mu$ s corresponded to the acoustic signal generated from the contrast agent holder containing 100 mM allylhydrazine. **Figure 4.9b** shows the processed ultrasound signals in the frequency domain after taking the Fast Fourier Transform of 20 individual timeframes in the ROI sampling at 100 MHz, and then taking the average of 20 frequency responses. The peak amplitude at 2.08 MHz before the addition of the hydroxyl radical was recorded as the baseline intensity. **Figure 4.10a** shows that after the hydroxyl radical (100  $\mu$ M) was added to the allylhydrazine inside the contrast agent holder, there was significant increase in the ultrasound echoes after 10 minutes. **Figure 10b** shows the

processed ultrasound signal in the frequency domain after taking the Fast Fourier Transform of 20 individual timeframes in the ROI sampling at 100 MHz, and then taking the average of 20 frequency responses. The peak amplitude at 2.08 MHz increased by 22 dB, and the presence of 2<sup>nd</sup> and 3<sup>rd</sup> harmonics indicate strong acoustic response generated from the reaction of allylhydrazine with radical oxidants.

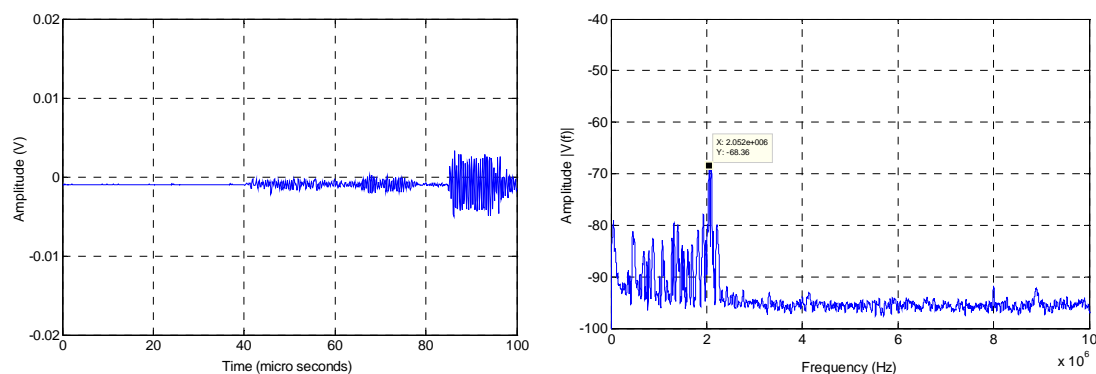


**Figure 4.9.** Acoustic characterization of allylhydrazine before the addition of the hydroxyl radical. A) Acoustic response of allylhydrazine in the time domain. B) Acoustic response of allylhydrazine in the frequency domain after Fast Fourier transform in the region of interest (40 – 80  $\mu$ s).

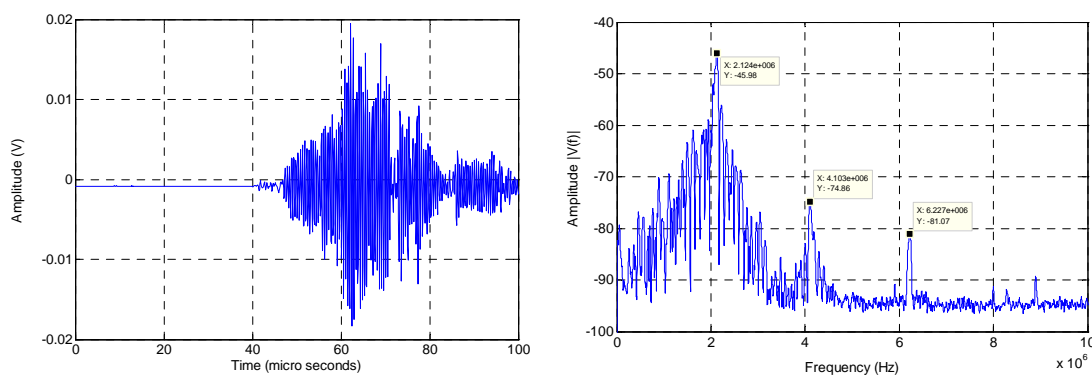


**Figure 4.10.** Acoustic characterization of allylhydrazine after the addition of the hydroxyl radical (100  $\mu$ M). A) Acoustic response of allylhydrazine in the time domain. B) Acoustic response of allylhydrazine in the frequency domain after Fast Fourier transform in the region of interest (40 – 80  $\mu$ s).

The acoustic response generated from allylhydrazine and the hydroxyl radical ( $\text{Fe}^{2+} + \text{H}_2\text{O}_2$ ) over time is shown in **Figure 4.11**. The fold increase in ultrasound intensity was calculated by dividing the acoustic intensity with radical oxidants (I) by the baseline intensity before the addition of radical oxidants ( $I_0$ ). The ultrasound echo reached peak intensity within 10 minutes for 10  $\mu\text{M}$ , 50  $\mu\text{M}$  and 100  $\mu\text{M}$  concentrations of hydroxyl radical. The vertical bars represent standard error of the mean, with  $n = 4$  for each data point.

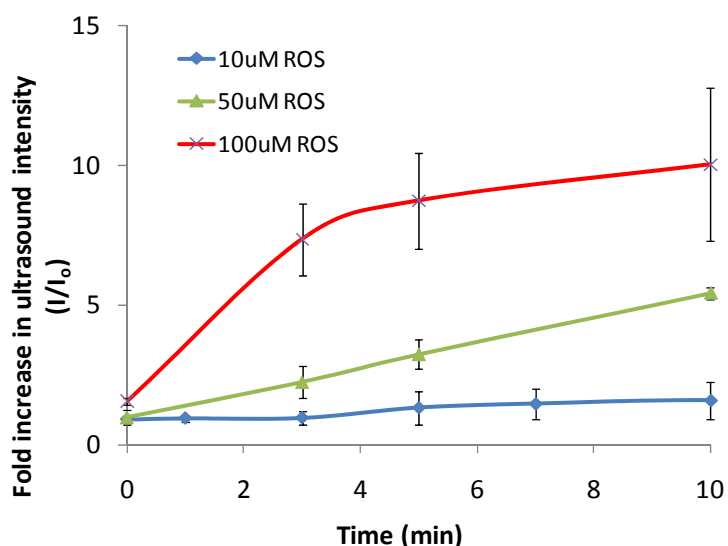


**Figure 4.11.** Allylhydrazine can react with hydroxyl radicals to generate bubbles and reach its peak acoustic intensity within a 10 minute period.

Physiologic radical oxidants concentrations are speculated to occur in the nanomolar to micromolar range [114], and we investigated if allylhydrazine could detect radical oxidants at this low concentration. Excess allylhydrazine (100 mM) was mixed with various concentrations of the hydroxyl radical (10  $\mu\text{M}$  - 1 mM) and the ultrasound

echo response was transmitted and received at 2.25 MHz (Mechanical Index = 0.28).

**Figure 4.12** demonstrates that allylhydrazine can detect a 10  $\mu\text{M}$  hydroxyl radical concentration, and displays a linear correlation between ultrasound intensity and hydroxyl radical concentrations within the range of 10  $\mu\text{M}$  - 1 mM ( $R^2 = 0.98$ ).

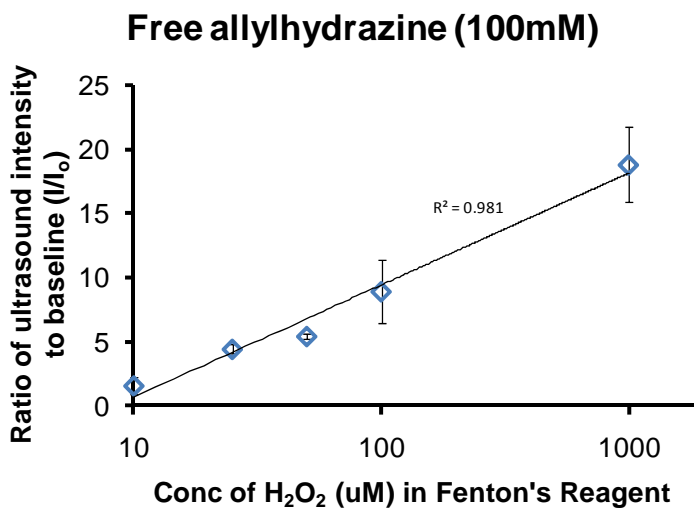


**Figure 4.12.** Allylhydrazine can detect micromolar concentrations of ROS and showing a linear correlation between ultrasound intensity and the hydroxyl radical concentration within the concentration range of 10  $\mu\text{M}$  - 1 mM ( $R^2 = 0.98$ ).



The effects of various ultrasound parameters and the acoustic response of allylhydrazine with various concentrations of the hydroxyl radical are summarized in

**Table 2.**

<b>Table 2. Summary of ultrasound parameters and acoustic response of allylhydrazine with various concentrations of the hydroxyl radical</b>							
[Allylhydrazine]	[•OH]	Freq (MHz)	Pressure (MPa)	cycle	Pulse sequence	FFT avg	Average Gain
100mM	100uM	2.07	0.4	20	sinusoidal	50	11.3
100mM	50uM	2.07	0.4	20	sinusoidal	50	5.4
100mM	25uM	2.07	0.4	20	sinusoidal	50	4.4
100mM	100uM	2.07	0.4	40	sinusoidal	50	14.5
100mM	20uM	2.07	0.4	40	sinusoidal	50	4.6
100mM	10uM	2.07	0.4	40	sinusoidal	50	1.3
100mM	10uM	2.07	0.4	60	sinusoidal	50	3.6
100mM	5uM	2.07	0.4	60	sinusoidal	50	1.0
100mM	0uM	2.07	0.4	20	sinusoidal	20	1.2
100mM	10uM	2.07	0.4	60	Pulse inversion	20	1.4
100mM	5uM	2.07	0.4	60	Pulse inversion	20	1.9
100mM	5uM	2.07	0.4	60	Pulse inversion	20	1.7

The acoustic responses of allylhydrazine analogs with various concentrations of the hydroxyl radical were investigated, and **Table 3** provides a summary of the acoustic response of 2-fluoro-allylhydrazine, 2-methyl-allylhydrazine, and (Z)-dec-2-enylhydrazine. The addition of methyl or fluorine group on the 2' carbon position did not enhance the acoustic response of bubble nucleation significantly, and the results were similar to allylhydrazine.

<b>Table 3. Summary of acoustic response of allylhydrazine analogs with various concentrations of the hydroxyl radical</b>							
[2-methyl-allylhydrazine]	[•OH]	Freq (MHz)	Pressure (MPa)	cycle	Pulse sequence	FFT avg	Average Gain
250mM	50uM	2.07	0.4	20	sinusoidal	50	1.2
100mM	100uM	2.07	0.4	20	sinusoidal	50	1.5
95mM	100uM	2.07	0.4	20	sinusoidal	50	1.4
25mM	100uM	2.07	0.4	20	sinusoidal	50	3
5mM	50mM	2.07	0.4	20	sinusoidal	50	6.1
5mM	1mM	2.07	0.4	20	sinusoidal	50	2.5
5mM	0.5mM	2.07	0.4	20	sinusoidal	50	2.3
5mM	50uM	2.07	0.4	20	sinusoidal	50	1
0.5mM	5mM	2.07	0.4	20	sinusoidal	50	1.3
[2-fluoro-allylhydrazine]	[•OH]	Freq (MHz)	Pressure (MPa)	cycle	Pulse sequence	FFT avg	Average Gain
100mM	100uM	2.07	0.4	20	sinusoidal	50	3.2
62mM	100uM	2.07	0.4	20	sinusoidal	50	3
50mM	100uM	5MHz	0.4	20	sinusoidal	50	1.6
25mM	100uM	2.07	0.4	20	sinusoidal	50	1
[(Z)-dec-2-enylhydrazine]	[•OH]	Freq (MHz)	Pressure (MPa)	cycle	Pulse sequence	FFT avg	Average Gain
250mM	200uM	2.07	0.4	20	sinusoidal	50	2.1
200mM	100uM	2.07	0.4	20	sinusoidal	50	1.2
50mM	1.5mM	2.07	0.4	20	sinusoidal	50	26.9
40mM	1mM	2.07	0.4	20	sinusoidal	50	3.5
25mM	3mM	2.07	0.4	20	sinusoidal	50	15.5
25mM	1mM	2.07	0.4	20	sinusoidal	50	2.2
20mM	5mM	2.07	0.4	20	sinusoidal	50	18.9
10mM	10mM	2.07	0.4	20	sinusoidal	50	11.05
5mM	10mM	2.07	0.4	20	sinusoidal	50	1

#### **4.3.4 *In vitro* characterization of bubble nucleation with clinical ultrasound system**

Representative results of detecting bubble nucleation with a clinical ultrasound system at various concentrations of the hydroxyl radical are shown in **Figure 4.13**. The background signals have been subtracted from the ultrasound images and shown over 10 minutes. Over time, bright spots began to accumulate on the holder membrane that was further away from the ultrasound probe. Interestingly, the location of the bubbles aligned directly with the area where the ultrasound probe was focused. This indicated that ultrasound enhanced bubble nucleation and regions outside the focal region of the ultrasound probe had less bubbles. At higher concentrations of hydroxyl radicals, stronger video intensity and more bubble formation were observed. For example, a 10  $\mu\text{M}$  hydroxyl radical concentration produced stronger video intensity than a 1  $\mu\text{M}$  hydroxyl radical concentration after 10 minutes.

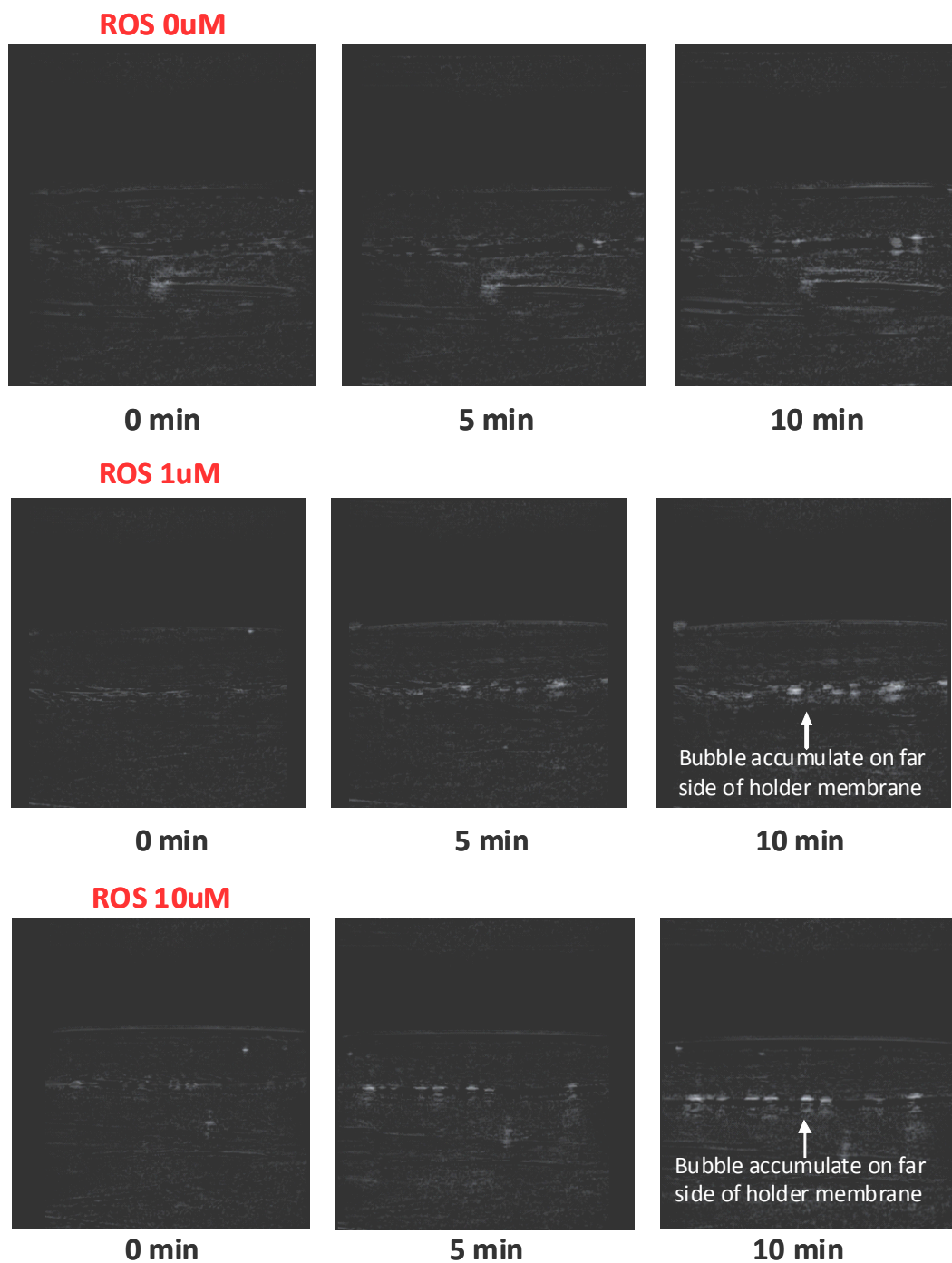


**Figure 4.13.** Representative ultrasound images of bubble detection with a clinical ultrasound system at various concentrations of the hydroxyl radical with allylhydrazine

These video images showed that bubble nucleation can be detected with a clinical ultrasound probe. To quantify the change in video intensity from bubble nucleation, the mean video intensity in the region of interest was measured over time for each hydroxyl radical concentration. **Figure 4.14** shows that higher hydroxyl radical concentrations correlated with stronger video intensity.

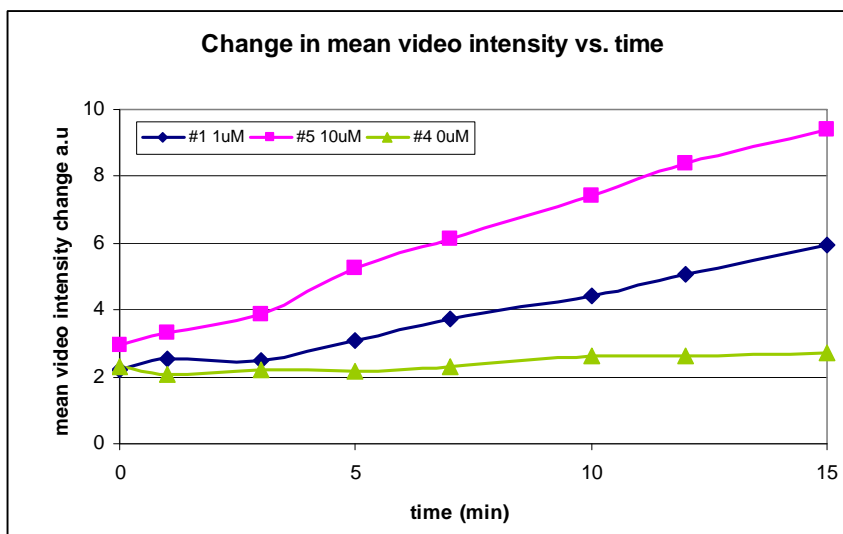
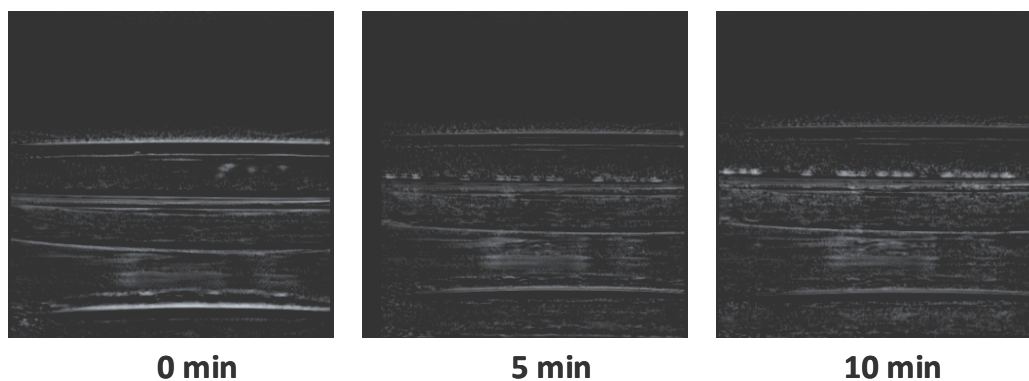


**Figure 4.14.** Bubble generation from the reaction of allylhydrazine with the hydroxyl radical can be detected in vitro by a clinical ultrasound system. Higher hydroxyl radical concentration results in greater change in mean video intensity within 15 minutes.

We also investigated if ultrasound can enhance bubble formation. The experiments were measured at 5.71 MHz using mechanical index (MI) = 1.5 (3.58 MPa) and MI = 0.6 (1.43 MPa). **Figure 4.15** shows that more bubbles accumulated inside the holder at higher MI = 1.5 compared to lower MI = 0.6. This indicates that stronger ultrasound power enhance bubble nucleation.

ROS 100 $\mu$ M (MI=1.5, 3.58MPa)



ROS 100 $\mu$ M (MI=0.6, 1.43MPa)

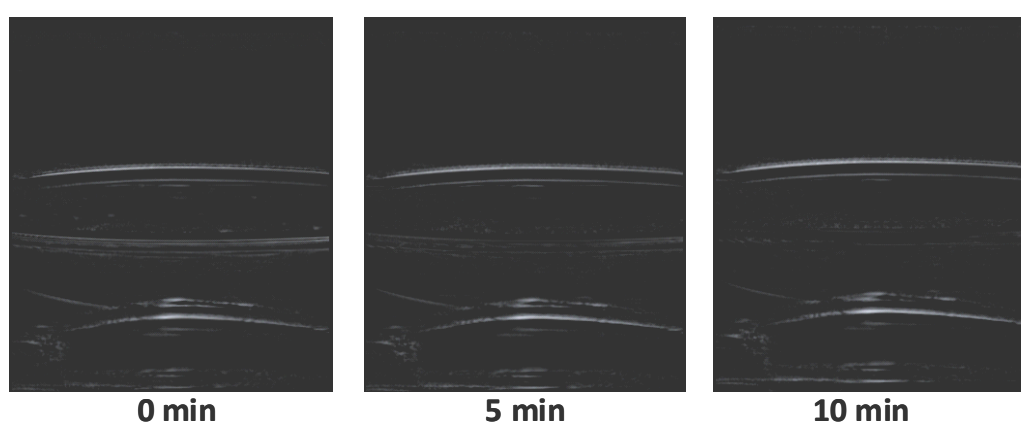


**Figure 4.15.** Representative ultrasound images showing that more bubbles are generated inside the holder at higher mechanical index (MI)

The quantitative analysis of the effect of mechanical index on video intensity is plotted in **Figure 4.16**. For a MI of 0.6 and a 100  $\mu$ M hydroxyl radical concentration, the mean video intensity remained constant. However, for a MI of 1.5, the mean video intensity increased by more than 40%, which suggested that ultrasound power can enhance bubble nucleation. The error bar represent standard error ( $n = 3$ ).

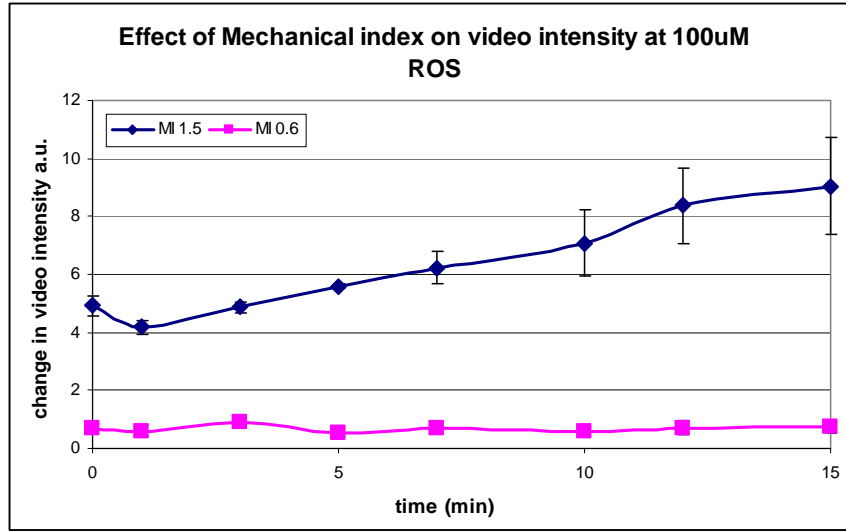


**Figure 4.16.** Stronger ultrasound power (higher MI) resulted in larger change in video intensity, suggesting enhancement of bubble nucleation

## 4.4 Discussion

### 4.4.1 Optical observation of bubble nucleation

We were able to observe and record optically large bubbles ( $>50 \mu\text{m}$ ) using the custom-built ultrasound testing system. Although smaller bubbles were also observed, they were not captured due to the limitation of the testing system. Smaller bubbles were more unstable and collapsed quickly once they are formed; however, larger bubbles coalesced from smaller bubbles were more stable and easier to capture optically. Using lower hydroxyl radical concentration resulted in fewer bubbles observed. The acoustic characterization of the microbubble identified by optical observation inside the cellulose tube demonstrated bubble-specific acoustic signal. Fast Fourier transform of the region of interest showed that the amplitude at 2.25 MHz (the interrogation frequency) increased by 15 dB (5 fold) when the bubble was present. These studies confirmed that the

oxidation of allylhydrazine by radical oxidants can nucleate bubbles and can be detected with ultrasound.

#### **4.4.2 Classical nucleation theory and observed results**

Classical bubble nucleation theory predicted that homogenous bubble nucleation occurs at exceedingly high concentrations above gas supersaturation [49-50]. However, physiological concentrations of ROS are believed to occur in the nanomolar to micromolar range, and to detect this level of radical oxidants can be challenging because this concentration represents a small change above gas saturation. The *in vitro* acoustic characterization showed that ultrasound was able to detect a 10  $\mu\text{M}$  radical oxidant concentration (**Fig. 4.12**). This concentration represents a small increase above the nitrogen gas saturation concentration, which is 450  $\mu\text{M}$ , and it is unclear if full bubble nucleation is occurring at this low level of supersaturation. Furthermore, the production of hydroxyl radical from Fenton's reagent is not a 100% yield process [115], which means that the actual concentrations of hydroxyl radical could be much lower.

To address the issue of bubble nucleation, many have shown that in the presence of pre-existing bubble nuclei, such as on the surfaces of the container or in the bulk solution, bubble nucleation occurs at much lower concentrations than theoretical prediction [49, 51]. These bubble nuclei or 'embryos' enhance bubble nucleation by lowering the energy barrier required to reach the critical nuclei radius [50, 53]. It has also been reported that bubble nucleation generated from chemical reactions occurs at much lower concentrations than theoretical prediction [52]. These evidences show that



although classical bubble nucleation theory is useful in predicting homogenous bubble nucleation, it has limited applications in heterogeneous conditions [51].

Furthermore, from the acoustic perspective, the pressure required for bubble nucleation in homogeneous water has been widely reported to exceed 10 MPa [116-117]. With the inclusion of physiologically-relevant nuclei, gas saturation and interfacial tension, the cavitation threshold decreases to hundreds of kilopascals at 0.75 or 1 MHz [118-119]. Ultrasound is extremely sensitive to the presence of small gas bubbles due to the large change in density and compressibility of such bubbles as compared with saline or plasma, and ultrasound detection of individual micron-sized gas bubble on the order of pL ( $10^{-12}$  L) volume has been demonstrated [55-57]. Here, nitrogen gas were generated in the presence of radical oxidants and increase the gas saturation beyond the saturation limit, creating a state in which small perturbations are expected to result in bubble nucleation. We hypothesize that the perturbations induced by ultrasound could enhance the nucleation rate under such conditions, and at low radical oxidant concentrations, ultrasound detected mixed states of gases and liquids [120]. Bubble nucleation can also be enhanced by ultrasound via rectified diffusion or inertial cavitation [121].

#### **4.4.3 Effect of ultrasound parameters on bubble nucleation and rectified diffusion**

The purpose of studying the effect of ultrasound parameters was to determine if bubble nucleation could be enhanced by ultrasound. It is known that bubble behavior can be affected by ultrasound such as rectified diffusion and inertial cavitation. In rectified diffusion, bubbles can grow in size after the acoustic pressure exceeds above a certain threshold. On the other hand, if the acoustic pressure is too high, the bubbles can expand

and collapse violently, resulting in cavitation. Therefore, various ultrasound parameters were investigated, including different frequencies (1-10 MHz), pulse sequences, pressure (100 kPa - 2 MPa), pulse repetition period (10-100 Hz), frequency modulation (chirp), and power modulation (strong pulse followed by weak intensity pulse). The goal was to optimize the ultrasound setting to detect bubble nucleation generated from the oxidation of allylhydrazine by radical oxidants.

To understand the interaction between ultrasound beam and bubble formation, we received help from our collaborator, Dr. Shengpin Qin in Dr. Catherine Ferrara's lab. He provided some theoretical explanations to our observation. In essence, the change in bubble radius can be modeled by the gas diffusion equation for acoustically-driven diffusion developed by Eller and Flynn [122]:

$$\frac{dR_o}{dt} = \frac{DR_g T}{R_o} \left( P_o + \frac{4\sigma}{3R_o} \right)^{-1} \left( A + R_o \left( \frac{B}{\pi D t} \right)^{1/2} \right) C_{sn} \left( \frac{C_i}{C_{sn}} - \frac{A}{B} \right)$$

$$A = \frac{1}{T_b} \int_0^{T_b} \frac{R}{R_n} dt \quad B = \frac{1}{T_b} \int_0^{T_b} \left( \frac{R}{R_n} \right)^4 dt \quad C_{sn} = C_o \left( 1 + \frac{2\sigma}{R_o P_o} \right)$$

Where  $R_o$  is the initial bubble radius,  $D$  is the gas diffusion coefficient,  $T$  is the temperature,  $\sigma$  is the surface tension coefficient,  $P$  is the internal pressure,  $R_g$  is the universal gas constant,  $C_i$  is the concentration of gas dissolved in the liquid far from the bubble,  $C_o$  is the saturation concentration of gas in the liquid.  $A$  and  $B$  are the time-dependent radial expansions of bubble radius and the ratio of  $A/B$  is governed by the radius-time curves from the radial equation:

$$\rho_L \left[ \left( 1 - \frac{\dot{R}}{c} \right) R \ddot{R} + \frac{3}{2} \dot{R}^2 \left( 1 - \frac{\dot{R}}{3c} \right) \right] = \left( 1 + \frac{\dot{R}}{c} \right) [p_g - p_o - p_{ac}(t)] + \frac{R}{c} \frac{dp_g}{dt} - 4\eta \frac{\dot{R}}{R} - \frac{2\sigma}{R}$$

The last two terms in the Eller-Flynn equation indicate that the rate of change of radius is positive if  $C_i/C_{sn} > A/B$ , meaning that bubble will grow. On the other hand, if the rate of change of radius is negative, bubble will dissolve. The condition when  $C_i/C_{sn} - A/B = 0$  is the threshold for rectified diffusion.

The threshold for rectified diffusion was modeled in **Figure 4.17**, which displayed the threshold for rectified diffusion with sinusoidal oscillation at 1 MHz frequency. The region above the curve shows the condition for rectified diffusion, and the region below the curve shows where bubble dissolution occurs. For bubbles smaller than 1  $\mu\text{m}$ , the acoustic pressure needed to generate rectified diffusion is very high, and bubbles can also fragment. However, the pressure required to generate rectified diffusion for bubbles larger than 1  $\mu\text{m}$  is significantly lower. Furthermore, larger bubbles are more stable because of lower surface tension. This explains why bubbles smaller than 10  $\mu\text{m}$  were not easily observed.

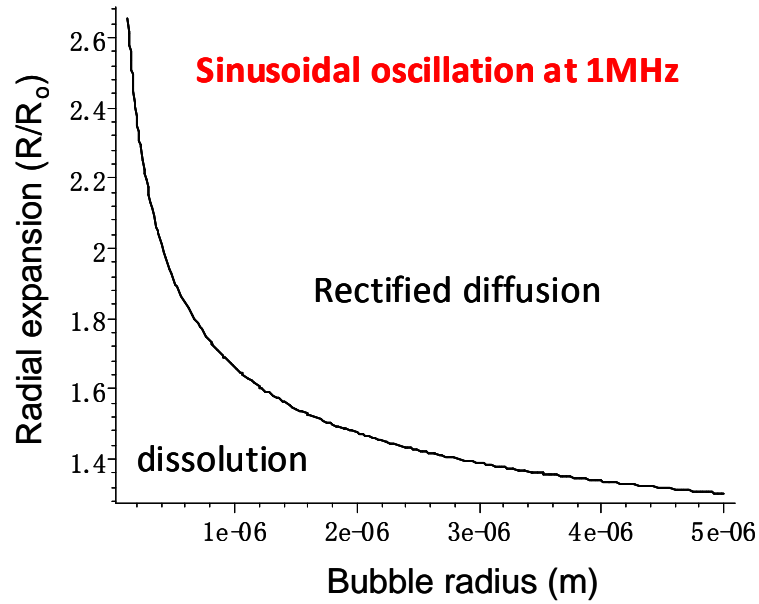


**Figure 4.17.** Threshold for rectified diffusion at 1 MHz sinusoidal oscillation frequency. The region above the curve is the condition for rectified diffusion, and the region below the curve is the condition for bubble dissolution.

The threshold for rectified diffusion at 2.25 MHz and 5 MHz sinusoidal frequencies were also modeled and displayed in **Figures 4.18** and **4.19**. The results were similar to the threshold at 1 MHz, and this explained why different frequencies and pulse sequences did not have significant contribution to bubble nucleation. Other factors in the Eller-Flynn equation can also contribute to bubble dissolution, such as the degree of gas saturation, initial bubble size, surface tension coefficient, and bubble expansion.

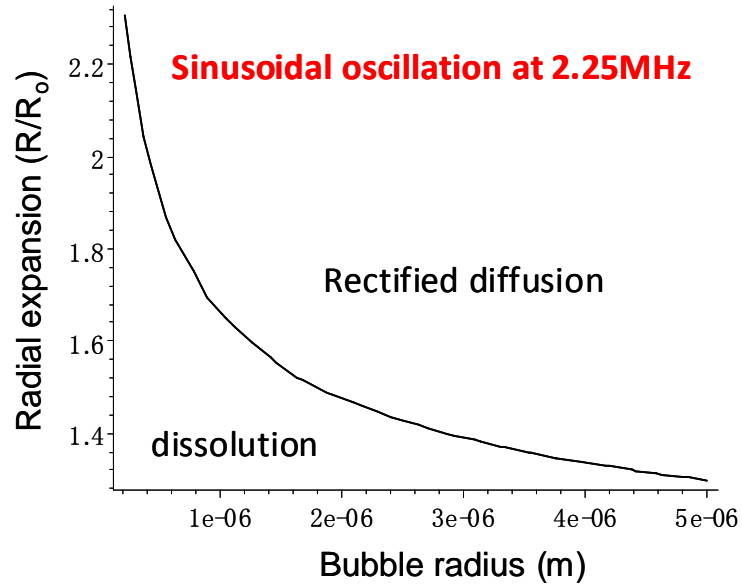


**Figure 4.18.** Threshold for rectified diffusion at 2.25 MHz sinusoidal oscillation frequency. The region above the curve is the condition for rectified diffusion, and the region below the curve is the condition for bubble dissolution.

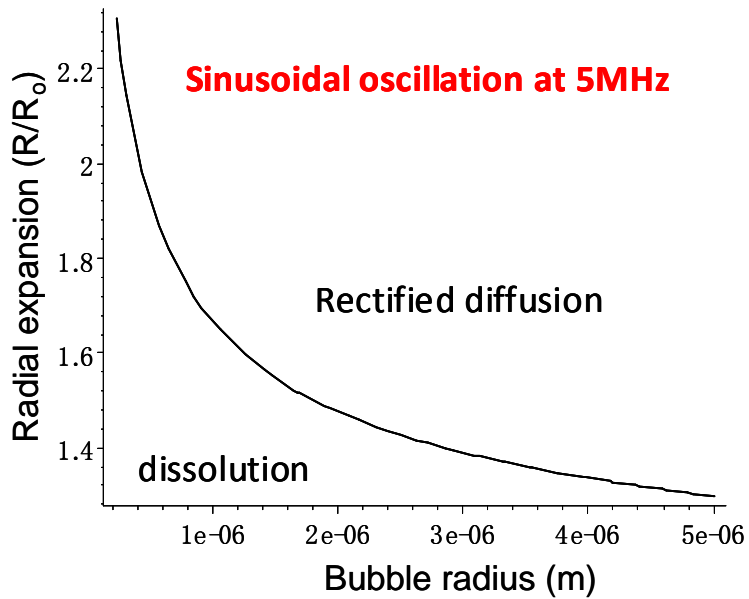


**Figure 4.19.** Threshold for rectified diffusion at 5 MHz sinusoidal oscillation frequency. The region above the curve is the condition for rectified diffusion, and the region below the curve is the condition for bubble dissolution.

## CHAPTER 5

### LIPOSOMAL ENCAPSULATION AND STABILIZATION OF ROS-INDUCED MICROBUBBLE

#### 5.1 Introduction

In order to reduce bubble dissolution and increase bubble stability, many have found that encapsulating gas microbubbles inside an amphiphilic biocompatible phospholipid shell can effectively lower the interfacial tension, adding rigidity and reducing gas escape [123-124]. Microbubbles encapsulated within liposomes smoothly expand and contract, and instantaneously self-assemble to repair membrane structure even during the ultrasound pulse. Furthermore, liposomes have been used in many applications of drug delivery, and their *in vivo* characteristics have been studied extensively, including biodistribution, biocompatibility, degradation and excretion pathways.

To test the hypothesis that liposome encapsulation of microbubbles can improve bubble stability and enhance *in vivo* efficacy, we adapted the liposome composition from a FDA-approved commercial contrast agent, Definity [86]. Definity is composed of 10 mol % 1,2-dipalmitoyl-sn-glycero-3-phosphoethanolamine (DPPE), 10 mol % 1,2-dipalmitoyl-sn-glycero-3-phosphatidic acid (DPPA), and 80 mol % 1,2-Dipalmitoyl-sn-glycero-3-phosphocholine (DPPC). The main phospholipid in this formulation is a neutral 16-carbon chain, and the charged DPPA phospholipid is designed to enhance bubble dispersion by adding a repulsive columbic force around the gas bubbles. In addition, liposomes with poly-ethyl-glycol (PEG) chains can prevent bubble coalescence and provide longer circulation time for *in vivo* applications. Another advantage of

encapsulating allylhydrazine inside the liposomes is to increase the local concentration of allylhydrazine and the probability for bubble nucleation.

In order to generate the hydroxyl radical ( $\bullet\text{OH}$ ) from hydrogen peroxide ( $\text{H}_2\text{O}_2$ ), iron is needed. However, sufficient amount of iron may not be present in areas with high production of ROS. One strategy is to incorporate iron complexed with hydrophobic porphyrin in the lipid bilayer. This will increase the sensitivity of allylhydrazine toward hydrogen peroxide.

We therefore investigated several liposomes formulation strategies, including the concentration of individual phospholipid, the phospholipid chain length, the amount of charged phospholipid, incorporating PEG chains and iron-porphyrin. The sizes of the liposomes and their encapsulation efficiency for allylhydrazine were also studied, and the final composition was optimized for *in vivo* applications. The acoustic response of allylhydrazine encapsulated within liposomes (APLs) reacting with the hydroxyl radical was characterized, and we found that APLs displayed stronger ultrasound intensity than free allylhydrazine. Finally, biodistribution of liposomes loaded with a fluorescent dye was investigated *in vivo*, and the liver was identified as an appropriate target for *in vivo* imaging.

## 5.2 Materials and Methods

### 5.2.1 Liposome composition and formulation

Various types of phospholipids were used, and **Table 4** provides a list of all the phospholipids used in this work and their abbreviation. All phospholipids were purchased from Genzym (Pittsburgh, PA).

**Table 4.** Phospholipid types and abbreviation

Abbreviation	Lipid Name
DPPE	1,2-Dipalmitoyl-sn-glycero-3-phosphoethanolamine
DSPE	1,2-Distearoyl-sn-glycero-3-phosphoethanolamine
DPPA	1,2-Dipalmitoyl-sn-glycero-3-phosphatidic acid
DSPA	1,2-Distearoyl-sn-glycero-3-phosphatidic acid
DSPC	1,2-Distearoyl-sn-glycero-3-phosphocholine
DPPC	1,2-Dipalmitoyl-sn-glycero-3-phosphocholine
DAPC	1,2-Diarachidoyl-sn-glycero-3-phosphocholine
DPPE-PEG5k	N-(Carbonyl-methoxypolyethyleneglycol 5000)-1,2 dipalmitoyl-sn-glycero-3- phosphoethanolamine
DPPE-PEG2k	N-(Carbonyl-methoxypolyethyleneglycol 2000)-1,2 dipalmitoyl-sn-glycero-3- phosphoethanolamine
DSPE-PEG2k	N-(Carbonyl-methoxypolyethyleneglycol 2000)-1,2 distearoyl-sn-glycero-3- phosphoethanolamine

The standard liposome formulation is composed of 80 mol % DPPC, 10 mol % DPPE and 10 mol % DPPA. For PEGylated lipid formulation, DPPE is replaced with DPPE-PEG5000. Briefly, 100 mg lipids were dissolved in chloroform in a 250 mL round bottom flask, and the solvent is evaporated on a rotovap to form a thin film on the wall of the flask, followed by drying over high vacuum for at least 8 hours. The lipid film is reconstituted with allylhydrazine solution, and heated to 5°C above the phospholipids main phase transition temperature ( $T_m = 41^\circ\text{C}$  for DPPC,  $55^\circ\text{C}$  for DSPC), followed by rapid quenching to 0°C in an ice-water bath. The heat/thaw cycle is repeated for at least 3



times over a period of 1 hour, until a clear/semi-transparent solution is observed. The solution is then sonicated in a sonicator bath for 1-2 minutes, and subjected to ultrasound testing immediately. **Table 5** lists the composition and the final lipid concentrations examined in this work.

**Table 5.** Liposomes compositions

Composition	Lipid concentration
10% DPPA, 10% DPPE, 80%DPPC	1mg/mL
10% DPPA, 10% DPPE, 80%DPPC	0.5mg/mL
10% DPPA, 10% DPPE, 80%DPPC	0.4mg/mL
10% DPPA, 80% DPPC, 10% DPPE-PEG5K	1mg/mL
80% DSPC, 10% DPPA, 10% DPPE-PEG5k + porphyrin (1mM)	1mg/mL
90% DAPC, 10% DSPE-PEG2k	1mg/mL
10% DSPE, 90% DSPC	0.5mg/mL

### Liposome Dialysis

The liposomes were injected into 2000 MWCO Dialysis Cassettes (Pierce Slide-A-Lyzer, Thermo Fisher) and dialyzed in 3 L of deionized water for 6-8 hours. The deionized water was replaced with fresh deionized water every hour.

### **5.2.2 Liposome characterization**

The sizes of liposome were characterized by a Brookhaven Particle Size Analyzer instrument based on DLS (dynamic light scattering) measurement.

The encapsulation efficiency of allylhydrazine inside liposomes was characterized. Two stock solutions of liposomes were prepared: one before dialysis and the other after dialysis. The liposomes in both stock solutions were lysed with 2 % Triton. The undialyzed liposomes were incubated with the TNBS assay to determine the

concentrations of amine present in the solution and the measured absorbance was taken as 100 % encapsulation efficiency. The dialyzed liposomes were also incubated with the TNBS assay to determine the concentration of amine present in the solution. The encapsulation efficiency was calculated by dividing the absorbance of undialyzed liposomes over the absorbance of dialyzed liposomes. Appropriate blank controls were used to correct for background absorbance.

### **5.2.3 *In vitro* acoustic characterization of allylhydrazine encapsulated in liposomes**

The *in vitro* acoustic characterization of APLs was performed using the same protocols for free allylhydrazine (section 4.2.4). Briefly, the water tank is filled with fresh degassed DI water at 37°C and the water temperature is controlled by an immersible heater capable of controlling the temperature within +/- 1°C. The contrast agent holder was filled with 10mL filtered non-degassed DI water, and the background acoustic signal was measured and recorded. Next, 1 mL of DI water was taken out of the holder through a 16-gauge needle syringe and 1 mL APL solution was added into the holder and allowed mixing by diffusion for 5 minutes. Then 2 mL solution is taken out of the holder, and 1 mL of H<sub>2</sub>O<sub>2</sub> stock solution and 1 mL of Fe<sup>2+</sup> stock solution (10 mM) were added. Immediately after the injection of H<sub>2</sub>O<sub>2</sub> and Fe<sup>2+</sup>, the acoustic signal was measured and recorded at time points: 0, 1, 3, 5, 7, 10, 15 and 20 minutes. The test was repeated at various H<sub>2</sub>O<sub>2</sub> concentrations from 1 µM to 1 mM, with fixed concentration of Fe<sup>2+</sup> (1 mM). DI water was used instead of H<sub>2</sub>O<sub>2</sub> as the control for no radical oxidants.

Two independent controls were used to verify bubble nucleation from the oxidation of allylhydrazine with radical oxidants. To investigate if liposomes alone could

be echogenic and generate acoustic signal, empty liposomes (without allylhydrazine) were tested at various concentrations of  $\text{H}_2\text{O}_2$  and  $\text{Fe}^{2+}$  (1 mM). To investigate if allylhydrazine is specific toward hydroxyl radical and not reacting with hydrogen peroxide alone, various  $\text{H}_2\text{O}_2$  concentrations (10  $\mu\text{M}$ , 100  $\mu\text{M}$ , 1 mM) were added to the solution containing APLs (100 mM) without  $\text{Fe}^{2+}$ .

#### **5.2.4 *In vivo* biodistribution of liposomes loaded with fluorescent marker**

To determine the biodistribution of liposomes and whether they can reach the liver within 10 minutes, the liposomes were loaded with IR-786 dye and injected intravenously into a mouse for near-IR fluorescence imaging. The mouse was sacrificed 10 minutes after liposomes injection, and the chest was opened and imaged with an Olympus OV100 fluorescence imaging system.

To determine if the dye-loaded liposomes only remained in the circulation or also accumulated in the tissue in the previous experiment, the vena cava was ligated and the heart was perfused with 5 mL of saline until the liver turned from reddish pink to pale white. As a control to remove auto-fluorescence, the same experiment was performed on another mouse injected with saline instead of liposomes loaded with fluorescent dye. The heart, liver, lung and kidney from both mice were harvested and placed in a Petri dish side by side for comparison.

In another study to determine the biodistribution of liposomes more accurately, one group of mice ( $n = 3$ ) were injected intravenously with liposomes loaded with Rhodamine B, and another group of mice ( $n = 3$ ) were injected with empty liposome. 10 minutes after liposome injection, the mice were sacrificed and the liver, lung, heart,

kidney and blood were harvested. The blood was drawn from the right ventricle of the heart directly and mixed with heparin to prevent blood coagulation. The organs were weighed and added with 1 mL of RIPA buffer, homogenized, and centrifuged for 2.5 min at 9000 rpm. The supernatant were aliquoted unto a microplate, and the fluorescence was measured using a filter setting for Rhodamin B (Ex: 540/Em: 625). The fluorescence was normalized to the tissue weight and plotted after subtracting background auto-fluorescence.

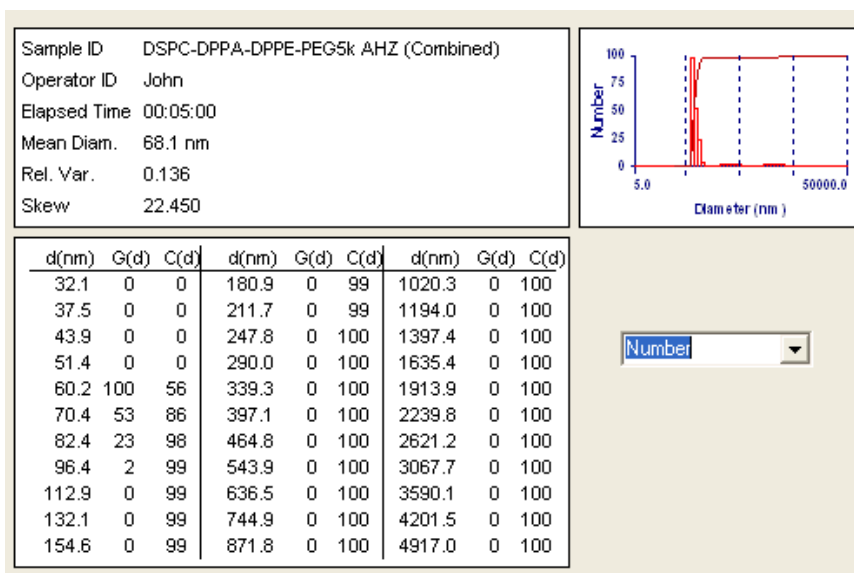
## 5.3 Results

### 5.3.1 Physical characterization of liposomes

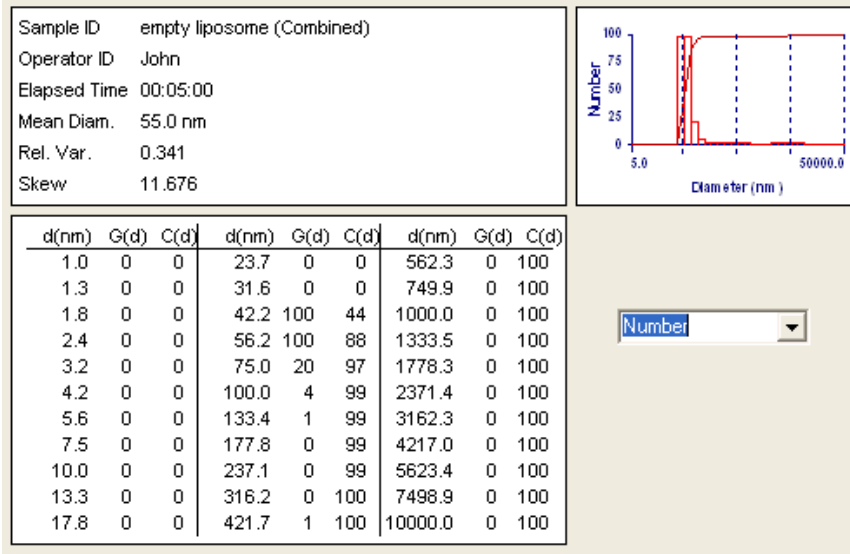
The liposomes sizes were characterized by DLS and were in the range between 30-100nm. The figures below displayed the results from various liposome formulations.

#### Allylhydrazine encapsulated within liposomes versus empty liposome

Liposomes with 1 M allylhydrazine: 80 % DSPC, 10 % DPPA, 10 % DPPE-PEG5K (10 mg/mL), mean diameter = 68 nm

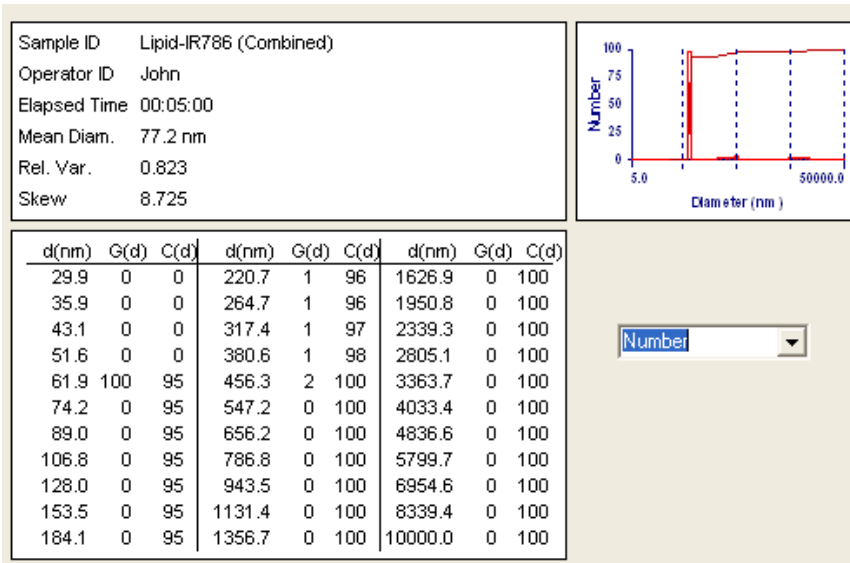


Empty liposomes: 80 % DSPC, 10 % DPPA, 10 % DPPE-PEG5K (10 mg/mL), mean diameter = 55 nm



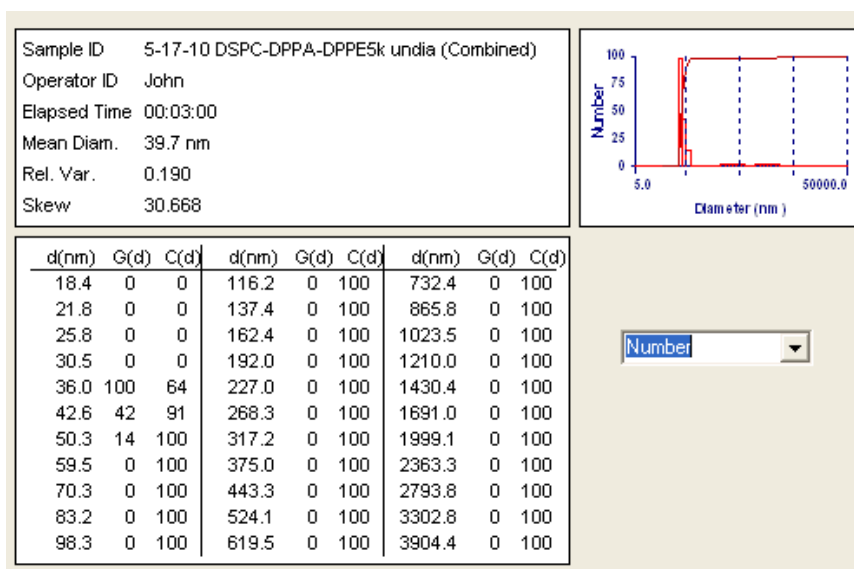
### Liposomes loaded with IR-786 dye

Liposomes loaded with IR-786: 80 % DSPC, 10 % DPPA, 10 % DPPE-PEG5K (10 mg/mL), mean diameter = 77 nm

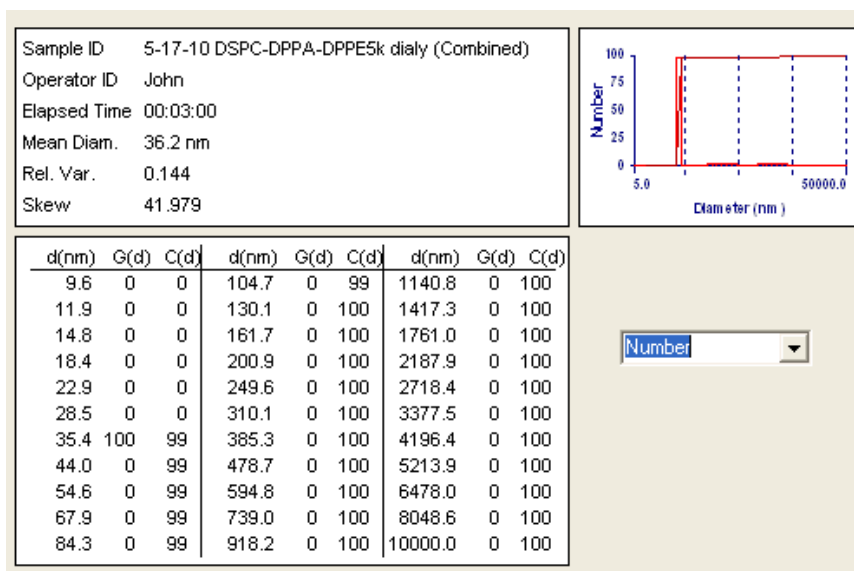


## Liposomes before and after dialysis

Liposomes before dialysis: 80 % DSPC, 10 % DPPA, 10 % DPPE-PEG5K (10 mg/mL) and 1 M allylhydrazine, mean diameter = 40 nm

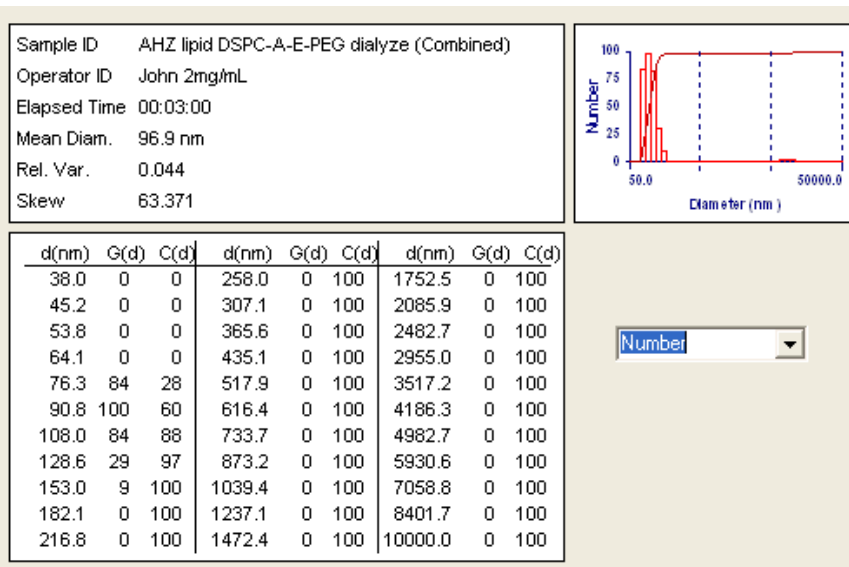


Liposomes after dialysis: 80 % DSPC, 10 % DPPA, 10 % DPPE-PEG5K (10 mg/mL) and 1 M allylhydrazine, mean diameter = 36 nm



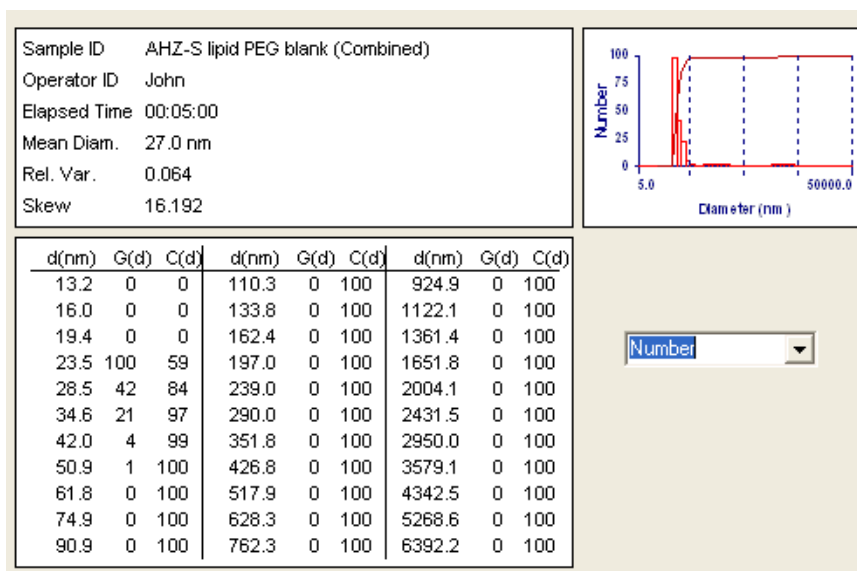
### Liposomes at lower lipid concentration

80 % DSPC, 10 % DPPA, 10 % DPPE-PEG5K (2 mg/mL) and 1 M allylhydrazine, mean diameter = 97 nm



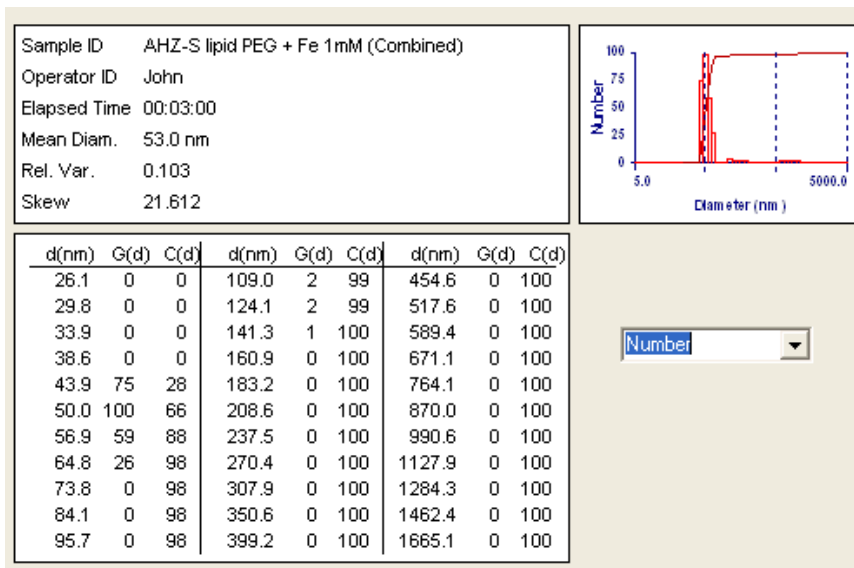
### Liposomes with Fe<sup>2+</sup> and H<sub>2</sub>O<sub>2</sub>

Liposomes without Fe<sup>2+</sup>: 80 % DPPC, 10 % DPPA, 10 % DPPE-PEG5K (10 mg/mL) and 1 M allylhydrazine, mean diameter = 27 nm

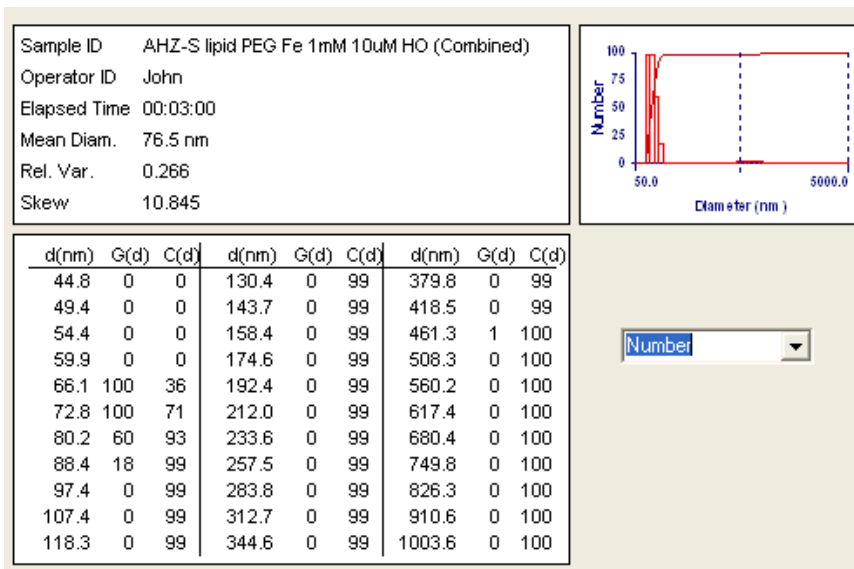




Liposomes with 1 mM  $\text{Fe}^{2+}$ : 80 % DPPC, 10 % DPPA, 10 % DPPE-PEG5K (10 mg/mL) and 1 M allylhydrazine, mean diameter = 53 nm



Liposomes with 1 mM  $\text{Fe}^{2+}$  and 10  $\mu\text{M}$   $\text{H}_2\text{O}_2$ : 80 % DPPC, 10 % DPPA, 10 % DPPE-PEG5K (10 mg/mL) and 1 M allylhydrazine, mean diameter = 77 nm



### Encapsulation efficiency

The encapsulation efficiency of liposomes was determined by the TNBS assay. Both dialyzed and undialyzed liposomes were lysed with 3% Triton to release the free allylhydrazine, which can react with the TNBS assay and produce an absorbance at 335 nm. The encapsulation efficiency of liposomes composed of 80% DSPC, 10% DPPA, 10% DPPE-PEG5000, and 1 M allylhydrazine typically ranged from 50% - 65%. The encapsulation efficiency was calculated from the absorbance of dialyzed liposomes divided by the absorbance of undialyzed liposomes at 335 nm absorbance wavelength. **Figure 5.1** shows a representative plot of the TNBS assay that was used to determine the encapsulation efficiency.

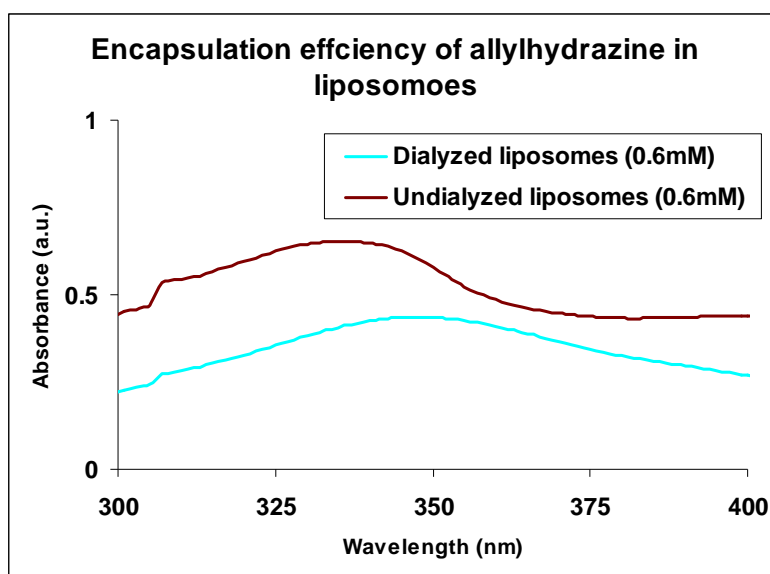


**Figure 5.1.** Liposomes encapsulation efficiency of allylhydrazine determined by the TNBS assay

### 5.3.2 *In vitro* acoustic response of allylhydrazine encapsulated within liposomes

Overall, allylhydrazine encapsulated within liposomes are more effective at detecting the hydroxyl radical than free allylhydrazine. PEGylated liposomes exhibited stronger acoustic response than non-PEGylated liposomes. Incorporating  $\text{Fe}^{2+}$  or porphyrin in the liposome compositions did not increase the sensitivity toward hydrogen peroxide because the iron was partially oxidized during the heat/thaw cycles in the formulation step. Moreover, adding excess  $\text{Fe}^{2+}$  in the liposomes resulted in precipitation during ultrasound testing. We found that the optimal liposome composition is 80 % DSPC, 10 % DPPA and 10 % DPPE-PEG5K (10 mg/mL). The final concentrations of liposomes and allylhydrazine were diluted 10 times during ultrasound testing. The acoustic response of allylhydrazine encapsulated within liposome with the hydroxyl radical is summarized in **Table 6**.

**Table 6.** Acoustic response of allylhydrazine encapsulated within various liposome compositions at various hydroxyl radical concentrations

	[AHZ]	[•OH]	Pressure (MPa)	cycle	Temp	Average Gain
DPPA/DPPC/DPPE (1mg/mL)	20mM	10uM	0.1	40	37°C	3.1
	20mM	1uM	0.1	40	37°C	1.3
	20mM	0uM	0.1	40	37°C	1.5
DPPA/DPPE/DPPC (0.5mg/mL)	10mM	100uM	0.1	40	37°C	23.3
	10mM	10uM	0.1	40	37°C	9.4
	10mM	1uM	0.1	40	37°C	4.3
	10mM	0uM	0.1	40	37°C	2.9
DPPA/DPPE/DPPC (0.4mg/mL)	10mM	10uM	0.1	40	37°C	1.9
	50mM	1uM	0.1	40	37°C	3.8
	50mM	0uM	0.1	40	37°C	4.0
DPPA/DPPC/DPPE-PEG5K (1mg/mL)	20mM	10uM	0.1	40	37°C	12.4
	20mM	1uM	0.1	40	37°C	7.2
	20mM	0uM	0.1	40	37°C	6.9
DPPA/DPPC/DPPE-PEG5k (1mg/mL)	20mM	10uM	0.1	40	37°C	5.4
	20mM	1uM	0.1	40	37°C	7.5
	20mM	0uM	0.1	40	37°C	7.4
DPPA/DPPC/DPPE-PEG5K (1mg/mL)	20mM	1uM	0.1	40	37°C	7.2
	20mM	0uM	0.1	40	37°C	1.1
DPPA/DPPC/DPPE-PEG5K (1mg/mL)	20mM	1uM	0.1	40	22oC	6.3
	20mM	0uM	0.1	40	37°C	2.9
DPPA/DPPC/DPPE-PEG5K (1mg/mL)	20mM	1mM	0.4	20	37°C	9.9
	20mM	10uM	0.4	20	37°C	2.6
	20mM	0uM	0.4	20	37°C	2.2
DSPC/DPPA/DPPE-PEG5k (1m/mL) + porphyrin (<1mM)	20mM	1mM	0.1	40	37°C	5.7
	20mM	10uM	0.1	40	37°C	2.1
	20mM	1uM	0.1	40	37°C	1.5
	20mM	0uM	0.1	40	37°C	1.7
DAPC-DSPE-PEG2k (1mg/mL)	20mM	10uM	0.1	40	37°C	2.4
	20mM	1uM	0.1	40	37°C	7.0
	20mM	0uM	0.1	40	37°C	7.7
DSPE/DSPC (0.5mg/mL)	10mM	1mM	0.1	40	37°C	6.0
	10mM	100uM	0.1	40	37°C	4.4

We examined if the APLs would produce a stronger acoustic signal in response to radical oxidants compared to free allylhydrazine. **Figure 5.2** shows that the APLs are more effective at detecting the hydroxyl radical than free allylhydrazine *in vitro*, and displays a linear correlation between ultrasound intensity and the hydroxyl radical concentration within the concentration range of 10  $\mu\text{M}$  - 1 mM ( $R^2 = 0.97$ ). For example, for a 10  $\mu\text{M}$  hydroxyl radical concentration the ultrasound intensity of the APLs increased 5.6 fold compared to only 1.6 fold for free allylhydrazine. Therefore, the APLs have the potential to improve the ability of allylhydrazine to detect radical oxidants *in vivo*.

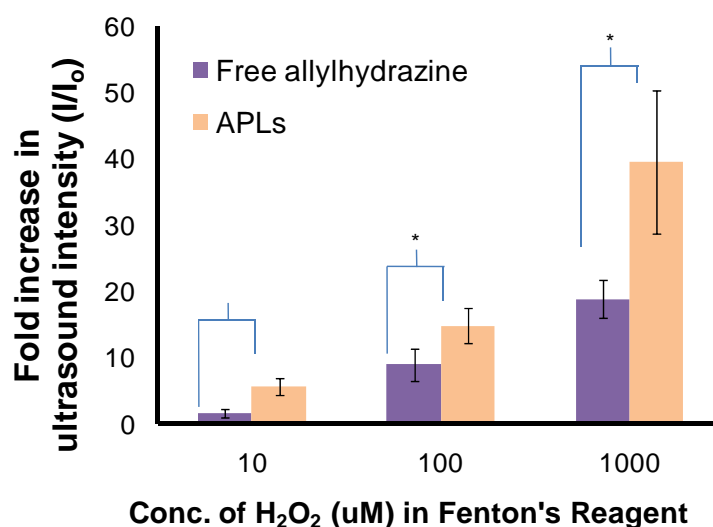


**Figure 5.2.** Acoustic response of allylhydrazine encapsulated within liposomes (APLs) showing linear correlation between ultrasound intensity and hydroxyl radical concentrations

Some phospholipids can trap gas bubbles during the preparation of the liposomes and induce echogenicity. Therefore, to investigate if liposomes alone contributed to an increase in ultrasound signal, empty liposomes with the same compositions as the APLs

(but without allylhydrazine) were investigated with various concentrations of  $\text{H}_2\text{O}_2$  and  $\text{Fe}^{2+}$  (1 mM). No increase in ultrasound intensity was observed, confirming that the liposomes themselves did not contribute to the increase in ultrasound echogenicity. Comparison of empty liposomes with the APLs demonstrated that allylhydrazine is the source of bubble nucleation and ultrasound signal (**Figure 5.3**).

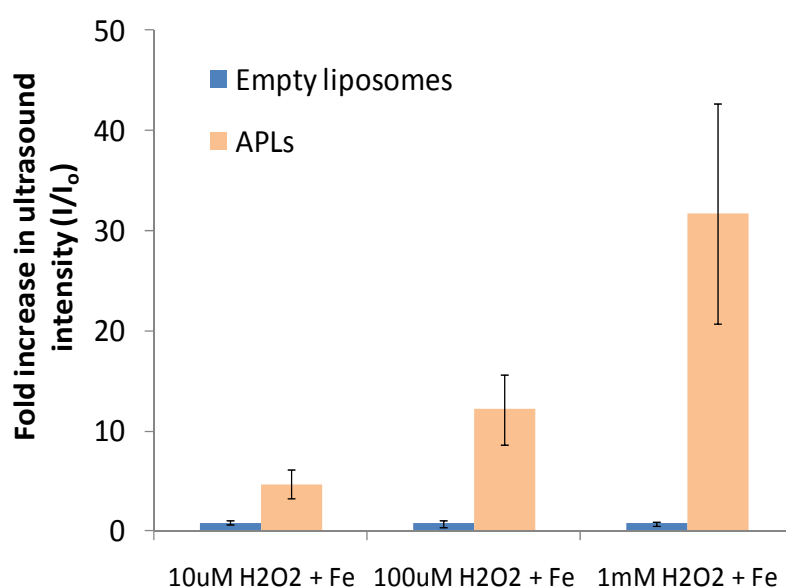


**Figure 5.3.** Hydroxyl radical added to empty liposomes did not show increase in ultrasound intensity

To investigate the specificity of the APLs toward the hydroxyl radical versus hydrogen peroxide, various  $\text{H}_2\text{O}_2$  concentrations (10  $\mu\text{M}$ , 100  $\mu\text{M}$  and 1 mM) were added to the APLs with 100 mM allylhydrazine. **Figure 5.4** showed that adding only  $\text{H}_2\text{O}_2$  (without  $\text{Fe}^{2+}$ ) to the APLs did not increase the ultrasound signal. This study demonstrated that the ultrasound response of allylhydrazine is specific toward radicals.

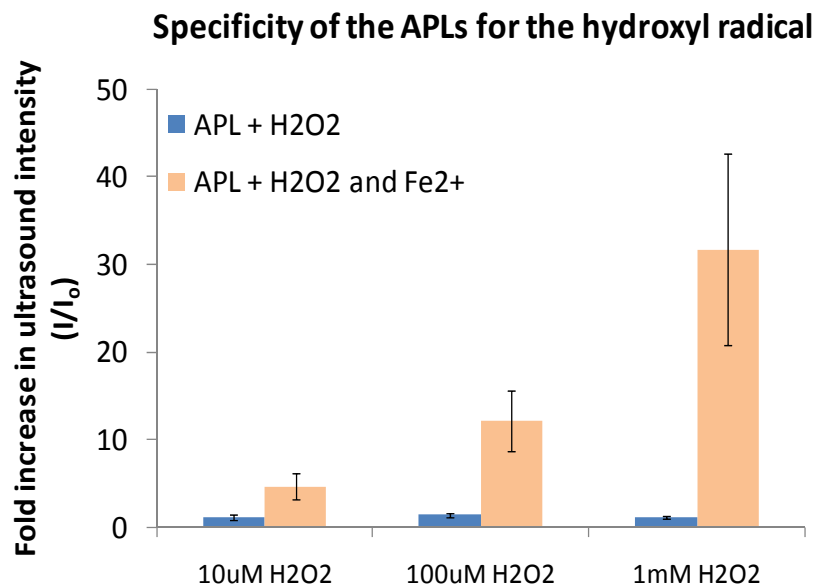


**Figure 5.4.** Control experiments demonstrating that the APLs are specific toward the hydroxyl radical. The APLs (100 mM) were mixed with various H<sub>2</sub>O<sub>2</sub> concentrations (10 μM, 100 μM, 1 mM) with Fe<sup>2+</sup> versus without Fe<sup>2+</sup>. The acoustic response showed that the ultrasound intensity increase with H<sub>2</sub>O<sub>2</sub> and Fe<sup>2+</sup>, but not with H<sub>2</sub>O<sub>2</sub> alone.

### 5.3.3 *In vivo* biodistribution of liposomes

To determine the biodistribution of the liposomes, the mice were injected with APL-based liposomes loaded with IR-786 dye and sacrificed after 10 minutes. **Figure 5.5** revealed that strong fluorescence were present in the liver and lung (upper right: bright field, lower left: near-infrared, upper left: merged image). This result confirmed that the liposomes can reach the liver within 10 minutes, which is a suitable timeframe for clinical ultrasound imaging.

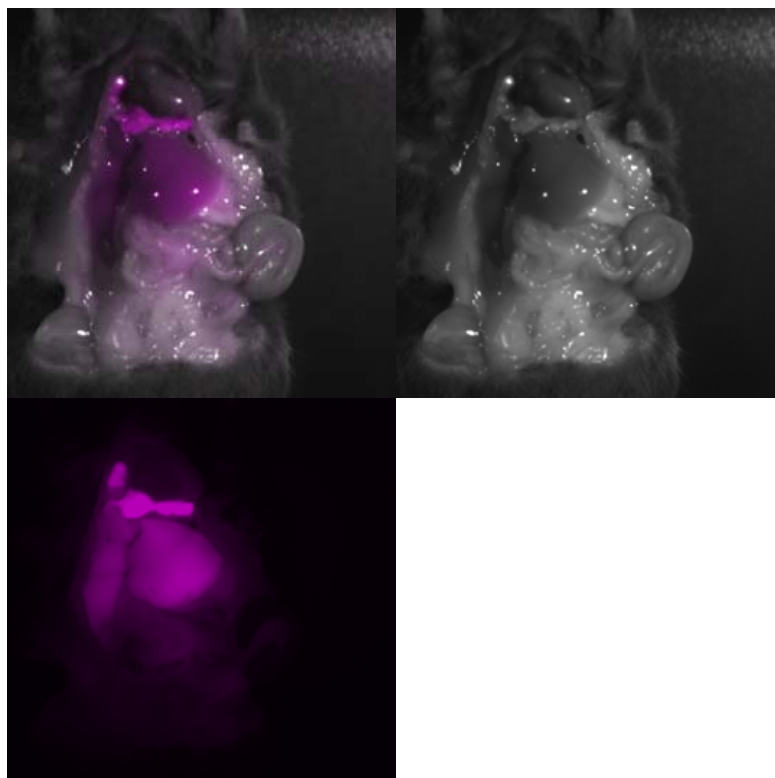


**Figure 5.5.** Fluorescence imaging revealed that liposomes loaded with IR-786 dye can reach the liver in 10 minutes

We also examined if the liposomes only remained in the circulation or also accumulated in the tissue. After the mice were sacrificed, the heart, liver, lung and kidney were perfused with saline and harvested. As a control to remove auto-fluorescence, the organs from another mouse injected with saline were also harvested and placed in a Petri dish for comparison. **Figure 5.6** showed that the organs from the mouse injected with liposomes loaded with IR-786 dye (left column) revealed stronger fluorescence than the organs from the control mouse injected with saline (right column). The fluorescence image also revealed that more liposomes accumulated in the liver and the lung than the heart or the kidney (upper right: bright field, lower left: near-infrared, upper left: merged image, lower right: heat map with color thresh).



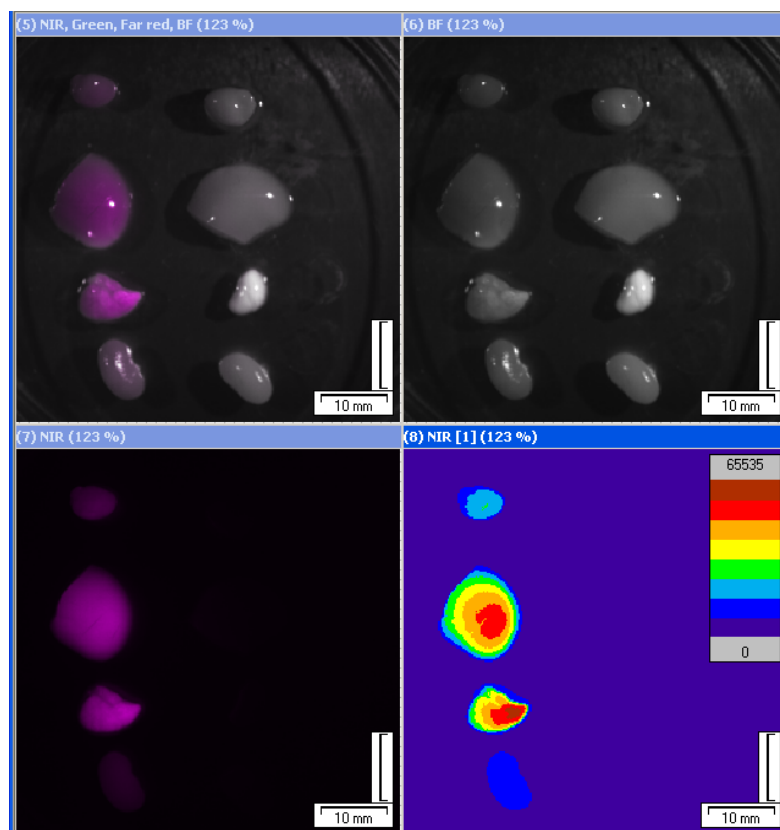


**Figure 5.6.** Fluorescence imaging liposomes loaded with IR-786 in the heart, liver, lung and kidney

In a separate study, the biodistribution of the liposomes was determined by injecting APL-based liposomes loaded with Rhodamine B dye intravenously into mice ( $n = 3$ ). The mice were sacrificed after 10 minutes, and **Figure 5.7** showed that large amount of liposomes accumulated in the liver, followed by the lung, the heart and the kidney. The Rhodamine B absorbance was normalized by tissue weight and compared to blood as well.

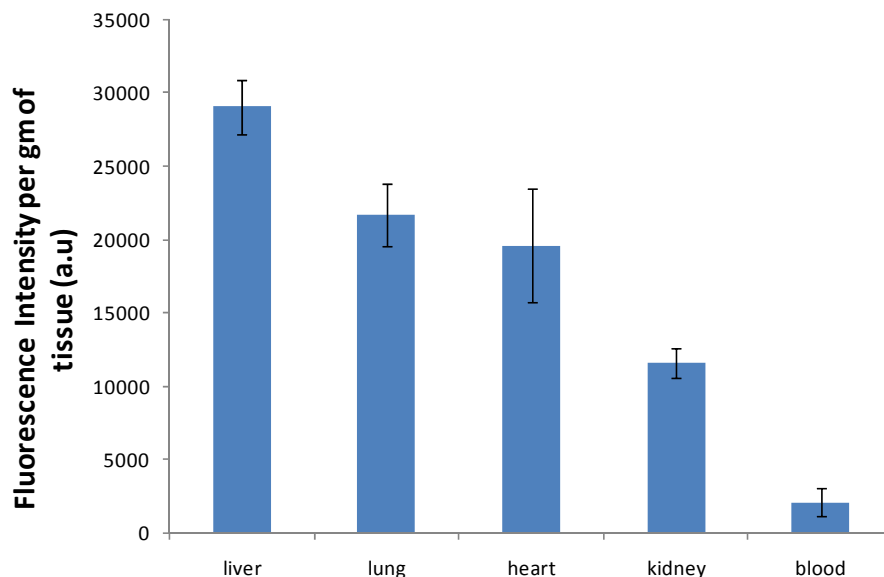


**Figure 5.7.** Biodistribution of APL-based liposomes loaded with Rhodamine B dye 10 minutes after injection

## 5.4 Discussion

### 5.4.1 Acoustic improvement of liposomal encapsulation

We expected enhanced bubble stability and stronger ultrasound signal from the APLs compared to free allylhydrazine for the same hydroxyl radical concentration. We also expected that longer phospholipid chain can provide more resistance against bubble dissolution by reducing the membrane permeability of gas. We found that DSPC (18C) was the optimal chain length with DPPA (16C) and DPPE-PEG5k (16C).

Both charged phospholipid and PEGylated liposomes can enhance bubble stability by improving bubble dispersion. However, we noticed that when PEGylated liposomes exceeded 10 mol % of the total liposome composition, they could come off of the liposomes and formed micelles on their own.

#### **5.4.2 Biodistribution of liposomes and *in vivo* implication**

The biodistribution studies showed that the liposomes can reach the liver within 10 minutes and accumulate locally. Since macrophages are the major sources of radical oxidants production in the body and they mostly reside in the liver, we expect that the liver could be a suitable organ for *in vivo* imaging of oxidative stress. The lung is another major source of macrophage, as confirmed by the *in vivo* biodistribution study. However, the lung is filled with air sacs that will generate strong background during ultrasound imaging, and this could present challenges for *in vivo* study. The heart and the kidney did not exhibit significant accumulation of liposomes *in vivo*, so they were not considered in the present study.

## **CHAPTER 6**

### **IN VIVO IMAGING OF OXIDATIVE STRESS USING CLINICAL ULTRASOUND SYSTEM**

#### **6.1 Introduction**

Reactive oxygen species are associated with many diseases, and the ability to detect oxidative stress *in vivo* can enhance the diagnosis of many diseases at an early stage. In order to assess the feasibility of using gas-forming reaction to image oxidative stress *in vivo* with ultrasound, several studies were performed. The goal of these studies was to apply the *in vitro* characterization under appropriate *in vivo* conditions, which are very dynamic and complex.

The first task is to determine if bubbles can be generated from the oxidation of allylhydrazine with radical oxidants inside the intraperitoneal (IP) cavity of mice and also be imaged with a clinical ultrasound system. Since the abdominal region is full of gastric gases, we need to determine if ultrasound can differentiate the signal from bubble nucleation versus the background. To examine this issue, allylhydrazine and hydroxyl radical were injected locally into the mice IP cavity, and the video intensity was recorded for 10 minutes. Detail results are discussed in the chapter.

For *in vivo* studies involving oxidative stress, the liver is a suitable organ for ultrasound imaging because: 1) the large size of liver makes it easy to identify, and 2) the liver is composed of tissue filled with vasculature and no air gaps, so it should present low background signal during ultrasound imaging, and 3) liver macrophages are a major source of ROS production in the body, and animal studies that induce inflammation in the liver are well-established. Hence, a Lipopolysaccharide (LPS) model of inflammation

was used to investigate the feasibility of imaging oxidative stress *in vivo* with allylhydrazine.

Our *in vivo* studies demonstrate that allylhydrazine can image oxidative stress in mice liver with good spatial resolution. To enhance targeting to the liver and to improve bubble stability, allylhydrazine was encapsulated inside phospholipid liposomes (APLs). The rationale for this approach was confirmed by both *in vitro* acoustic characterization and *in vivo* biodistribution studies described in the previous chapter. The *in vivo* studies using the APLs to image oxidative stress displayed improvement with reduction in background signal. Appropriate controls were also examined by injecting empty liposomes in mice treated with LPS to confirm that the ultrasound signal was not generated by empty liposomes or inflammation alone. Finally, a clinical contrast agent, Definity was used as a comparison with the results from *in vivo* studies using the APLs.

## **6.2 Materials and Methods**

### **6.2.1 *In vivo* study with intraperitoneal injection of allylhydrazine and hydroxyl radical**

Two C57Bl/6 male mice, aged 8-10 weeks, were house-bred in Emory University Animal Care facility. The mice were anaesthetized with isofluorane and the fur on the chest and abdomen was removed. Two clay-dough potties were pressed against the mice abdomen from both sides to stabilize the mice. An ultrasound probe was placed horizontally across the ventral surface of the mice intraperitoneal (IP) cavity. In the first study, 4 mL saline was injected into the IP cavity of the mice using an insulin syringe, followed by injection of 1 mL allylhydrazine (1 M). Next, 0.5 mL of H<sub>2</sub>O<sub>2</sub> (10 mM) and

0.5 mL  $\text{Fe}^{2+}$  (10 mM) were injected into the IP cavity with an insulin syringe, and constituted a final hydroxyl radical concentration of 1 mM inside the IP cavity.

In the second study, lower hydroxyl radical concentration was investigated, and 4 mL saline was injected into the IP cavity of the mice using an insulin syringe, followed by injection of 1 mL allylhydrazine (1 M). Next, 0.5 mL of  $\text{H}_2\text{O}_2$  (1 mM) and 0.5 mL  $\text{Fe}^{2+}$  (10 mM) were injected into the IP cavity with an insulin syringe, and constituted a final hydroxyl radical concentration of 86  $\mu\text{M}$  inside the IP cavity.

The IP cavity was imaged using a 14 MHz Siemens Acuson Sequoia 512 clinical ultrasound system (Siemens, USA) at various time points before and after each injection (MI = 0.05, 187 kPa pressure, 1.5 cycle pulses and 70 Hz pulse repetition frequency). The ultrasound transmitted power was minimized and a linear relationship between transmitted power (dB) and video intensity was observed. DICOM image data were processed with ImageJ software (NIH). All animal studies were conducted under a protocol that was approved by the Animal Use and Care Committee of Emory University.

### **6.2.2 *In vivo* LPS model with allylhydrazine**

Two groups of C57Bl/6 male mice (n = 5 per group), aged 8-10 weeks, were obtained from Jackson Labs. Inflammation was induced by injecting 200  $\mu\text{L}$  of LPS in saline (2 mg/mL) into the peritoneal cavity of the mice, 200  $\mu\text{L}$  of saline was injected into control mice. 20 hours later the mice were anaesthetized with isofluorane and the fur on the chest and abdomen was removed. An ultrasound probe was placed horizontally across the ventral surface of the mice chest, and 100  $\mu\text{L}$  of allylhydrazine solution (14 mg/mouse) was injected intravenously into the retro-orbital capillary bed. The mouse

liver was imaged using a 14 MHz Siemens Acuson Sequoia 512 clinical ultrasound system (Siemens, USA) for 10 minutes after allylhydrazine injection (MI = 0.05, 187 kPa pressure, 1.5 cycle pulses and 70 Hz pulse repetition frequency). The ultrasound transmitted power was minimized and a linear relationship between transmitted power (dB) and video intensity was observed. DICOM image data were processed with ImageJ software (NIH). The region of interest in the liver was analyzed and the mean video intensity was normalized. All animal studies were conducted under a protocol that was approved by the Animal Use and Care Committee of Emory University. All treatment groups were analyzed for statistical significance ( $*p < 0.05$ ) by an unpaired t-test.

### **6.2.3 *In vivo* LPS model with allylhydrazine encapsulated in liposomes**

Two groups of C57Bl/6 male mice (n = 5 per group), aged 8-10 weeks, were obtained from Jackson Labs. Inflammation was induced by injecting 200  $\mu$ L of LPS in saline (2 mg/mL) into the peritoneal cavity of the mice, 200  $\mu$ L of saline was injected into control mice. 20 hours later the mice were anaesthetized with isofluorane and the fur on the chest and abdomen was removed. An ultrasound probe was placed horizontally across the ventral surface of the mice chest, and 100  $\mu$ L of APLs (14 mg allylhydrazine/mouse) was injected intravenously into the retro-orbital capillary bed. The mouse liver was imaged using a 14 MHz Siemens Acuson Sequoia 512 clinical ultrasound system (Siemens, USA) for 10 minutes after the APLs injection (MI = 0.05, 187 kPa pressure, 1.5 cycle pulses and 70 Hz pulse repetition frequency). The ultrasound transmitted power was minimized and a linear relationship between transmitted power (dB) and video intensity was observed. DICOM image data were processed with ImageJ

software (NIH). The region of interest in the liver was analyzed and the mean video intensity was normalized. To investigate if the increase in ultrasound signals was due to the radicals reacting with allylhydrazine inside the liposomes and not due to the tissue becoming more echogenic during inflammation, empty liposomes (without allylhydrazine) were injected into mice treated with LPS after 20 hours, and the mice were imaged with a clinical ultrasound system. All animal studies were conducted under a protocol that was approved by the Animal Use and Care Committee of Emory University. All treatment groups were analyzed for statistical significance ( $*p < 0.05$ ) by an unpaired t-test.

#### **6.2.4 Comparison with clinical contrast agents (Definity)**

Two C57Bl/6 male mice, aged 8-10 weeks, were obtained from Jackson Labs. The mice were anaesthetized with isoflurane and the fur on the chest and abdomen was removed. An ultrasound probe was placed horizontally across the ventral surface of the mice chest. The mice liver was imaged using a 14 MHz Siemens Acuson Sequoia 512 clinical ultrasound system (Siemens, USA) with fixed ultrasound settings (MI = 0.05, 187 kPa pressure, 1.5 cycle pulses and 70 Hz pulse repetition frequency).

In the first study, 50  $\mu$ L of Definity (1000 x dilution) was injected intravenously into the retro-orbital capillary bed. The mice liver was imaged before and after each injection at various time points (0, 1, 2, 3, 5, 7, 10 min). In the second study, 50  $\mu$ L of Definity (1000 x dilution) was injected intravenously into the retro-orbital capillary bed. The mice liver was imaged with both B-mode and Doppler imaging before and after each injection at various time points (0, 1, 2, 3, 5, 7, 10 min).



The ultrasound transmitted power was minimized and a linear relationship between transmitted power (dB) and video intensity was observed. DICOM image data were processed with ImageJ software (NIH). All animal studies were conducted under a protocol that was approved by the Animal Use and Care Committee of Emory University.

## 6.3 Results

### 6.3.1 Ultrasound imaging of bubble nucleation inside intraperitoneal cavity of mice

We investigated if the reaction of allylhydrazine with the hydroxyl radical can generate bubbles inside the mice IP cavity and be detected with a clinical ultrasound system. **Figure 6.1 (A-F)** shows that mice injected with allylhydrazine (100 mM) and the hydroxyl radical (1 mM) generated detectable amount of bubbles almost immediately after the hydroxyl radical injection. Increase in video intensity (brighter image) corresponds with stronger echogenicity. **Fig. 6.1 (A)** shows the mice IP cavity before injection, and **Fig. 6.1 (B)** shows the mice cavity after the injection of 4 mL of saline, and the skin bulged upward due to the fluid pressure. The dark background in the IP cavity is the fluid, and the bright spot in the middle of the IP cavity is the tip of needle. In **Fig. 6.1 (C)**, bubble formation was observed immediately following the injection of allylhydrazine and the hydroxyl radical, as shown by the bright spots (indicated by the arrow) in the IP cavity. **Figure 6.1 (D-F)** shows that the video intensity increased continually for 10 minutes until the IP cavity is filled with bubbles.

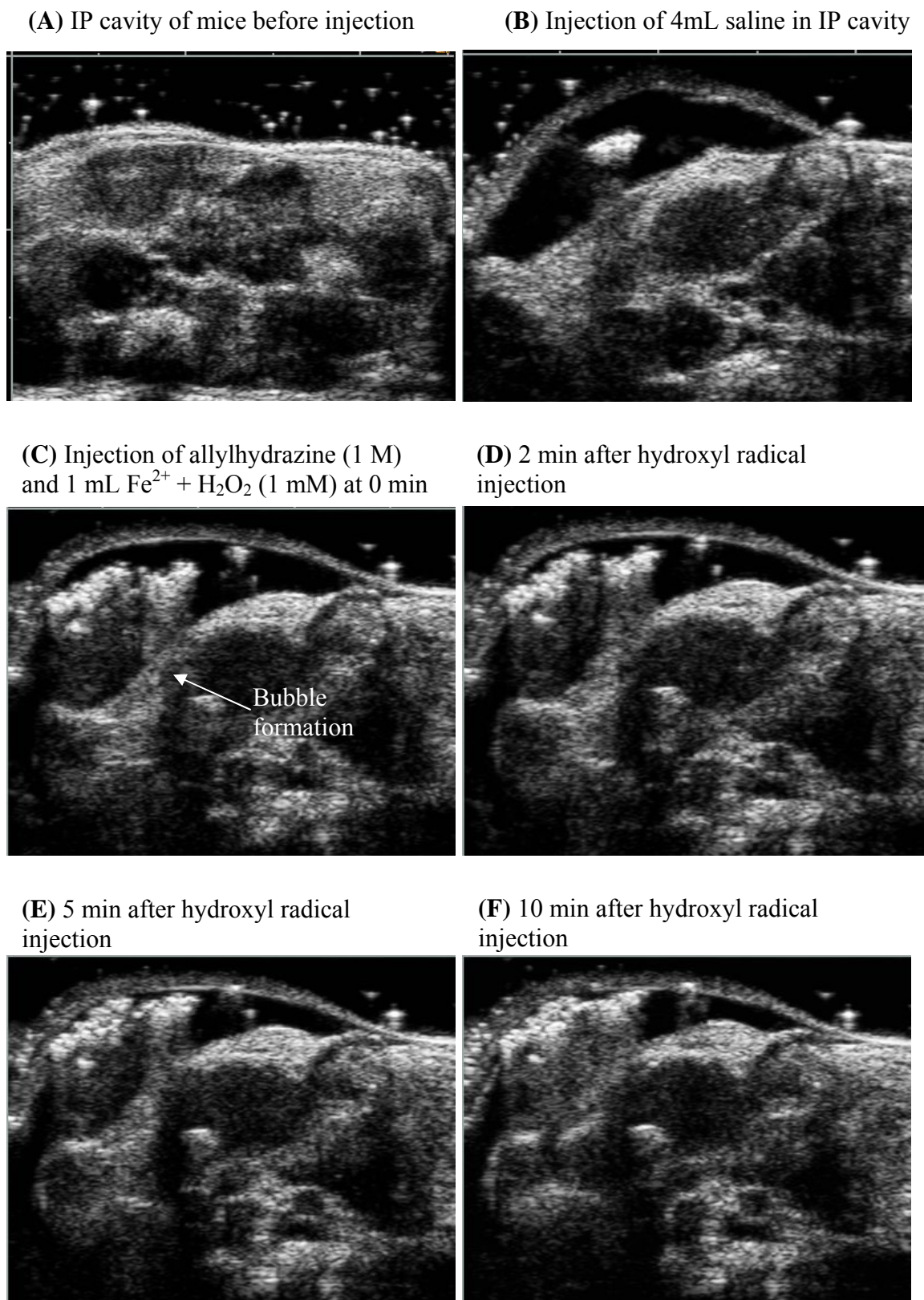
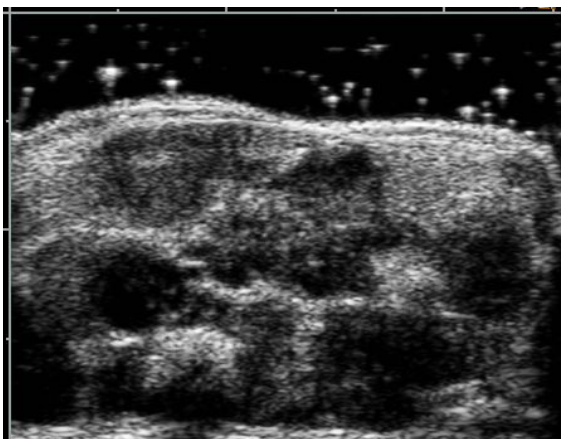


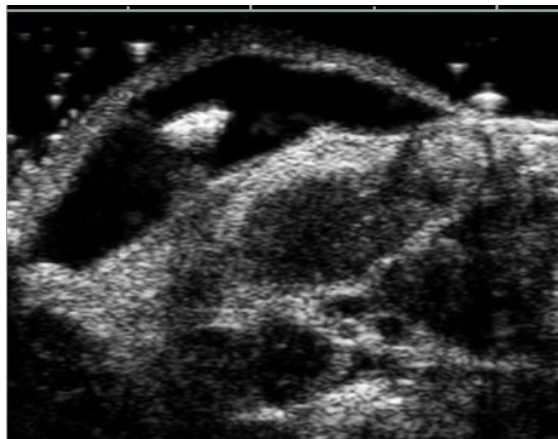
**Figure 6.1.** Injection of allylhydrazine (100 mM) and hydroxyl radical (1 mM) inside mouse IP cavity

We next investigated if bubble formation could be generated at lower hydroxyl radical concentration and also be detected with ultrasound. **Figure 6.2 (A-F)** shows that mice injected with allylhydrazine (100 mM) and the hydroxyl radical (86  $\mu$ M) generate significant amount of bubbles immediately after injection. **Fig. 6.2 (A)** shows the mice IP cavity before injection. **Fig. 6.2 (B)** shows the mice cavity after the injection of 4 mL saline, and the skin bulged upward due to the fluid pressure. The dark background in the IP cavity is the fluid, and the bright spot in the middle of the IP cavity is the tip of needle. **Fig. 6.2 (C)** shows the mice IP cavity after injection of allylhydrazine. In **Fig. 6.2 (D)** bubble formation was observed immediately following the injection of allylhydrazine and the hydroxyl radical, as shown by the bright spots in the IP cavity (indicated by the arrow). **Figure 6.2 (E-F)** shows that the video intensity increased continually for 10 minutes until the IP cavity is filled with bubbles. Comparing with the results from 1 mM hydroxyl radical concentration (**Fig. 6.1**), significant bubble formation can still be detected with a clinical ultrasound system even at lower hydroxyl radical concentrations (**Fig. 6.2**).

(A) IP cavity of mice before injection



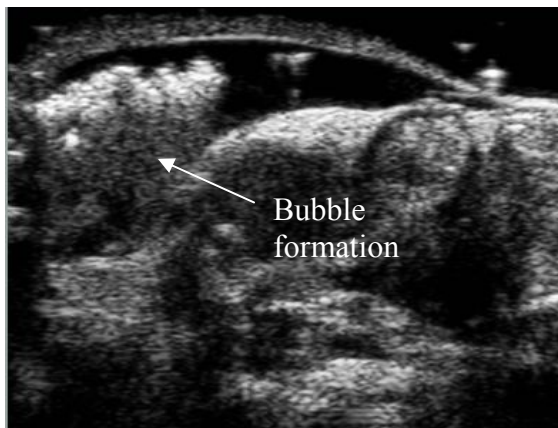
(B) Injection of 4mL saline in IP cavity



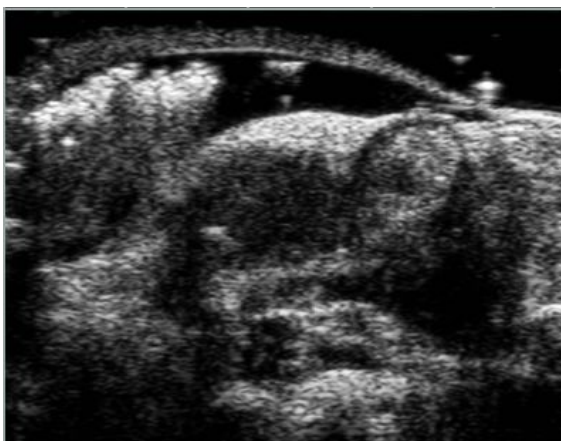
(C) Injection of 1 mL allylhydrazine (final concentration = 100 mM)



(D) Injection of 1 mL  $\text{Fe}^{2+} + \text{H}_2\text{O}_2$  (final concentration = 86  $\mu\text{M}$ ) at 0 min



(E) 2 min after hydroxyl radical injection



(F) 10 min after hydroxyl radical injection

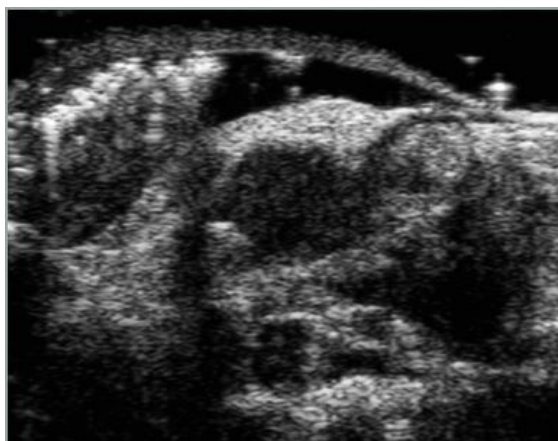


**Figure 6.2.** Injection of allylhydrazine (100 mM) and the hydroxyl radical (86  $\mu\text{M}$ ) inside mouse IP cavity

### 6.3.2 *In vivo* imaging of oxidative stress using allylhydrazine

We investigated the *in vivo* feasibility of using allylhydrazine to image oxidative stress in mice, triggered by an LPS-induced inflammatory response. Mice were given an intraperitoneal injection of LPS, or saline as a control. Allylhydrazine (14 mg/mouse) was injected intravenously into the retro-orbital capillary bed of the mice 20 hours later. The mice were then imaged with a Siemens Acuson Sequoia 512 clinical ultrasound machine at a 14 MHz frequency. **Figure 6.3** demonstrates that allylhydrazine can enhance acoustic contrast in mice experiencing oxidative stress. For example, 10 minutes after allylhydrazine injection, the livers of LPS-treated mice became significantly brighter, in comparison to mice treated with saline (**Fig. 6.3 B**).

We performed quantitative analysis on the ultrasound images and **Figure 6.4** shows that after 10 minutes, the normalized mean video intensity of LPS-treated mice increased by 60%, compared to a 30% increase for mice treated with saline. The normalized mean video intensity was determined by comparing the video intensity of the liver at 0 min and 10 min after the allylhydrazine injection. We expected that the 30% increase in background signal observed in saline-treated mice was due to the reaction of allylhydrazine with mitochondrial radical oxidants produced by metabolism [1]. The enhancement in ultrasound intensity indicated that allylhydrazine reacted with radical oxidants *in vivo* and generated gas forming molecules. These results also demonstrated that allylhydrazine can detect oxidative stress *in vivo* with 3D spatial resolution that cannot be achieved using fluorescent [33] or chemiluminescent [35] based contrast agents.

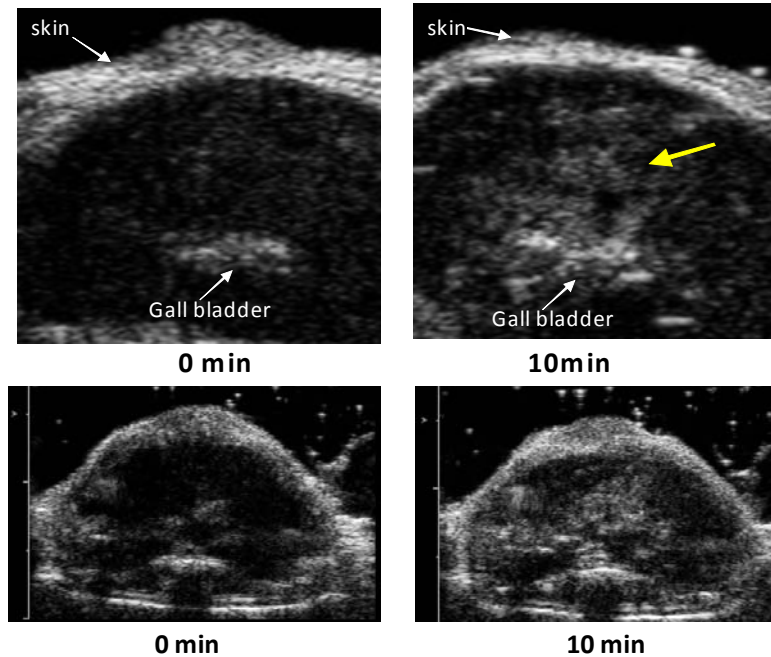
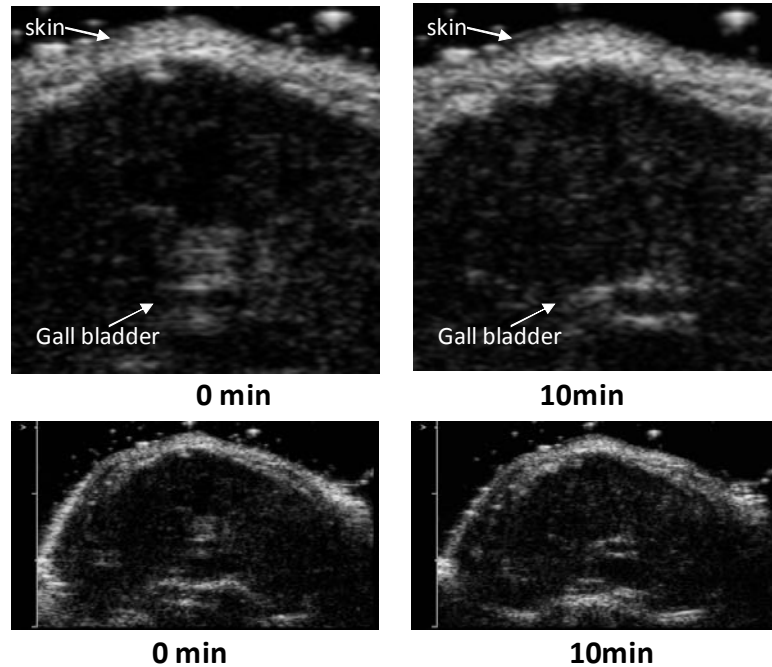


**Figure 6.3.** Representative ultrasound images of mice livers treated with allylhydrazine and LPS versus treatment with allylhydrazine and saline. Ultrasound images were taken at 0 min and 10 min after the allylhydrazine injection. The lower panel shows the entire cross-section area of the mice chest, and the upper panel shows the zoom-in area of the liver.

(A) Mice treated with LPS and allylhydrazine. Representative ultrasound images of the mouse liver show enhanced acoustic contrast after 10 minutes after the allylhydrazine injection. Arrow indicates location of enhanced acoustic contrast in the liver.





**(B)** Mice treated with saline and allylhydrazine. Representative ultrasound images of the mouse liver did not show significant changes 10 minutes after the allylhydrazine injection.

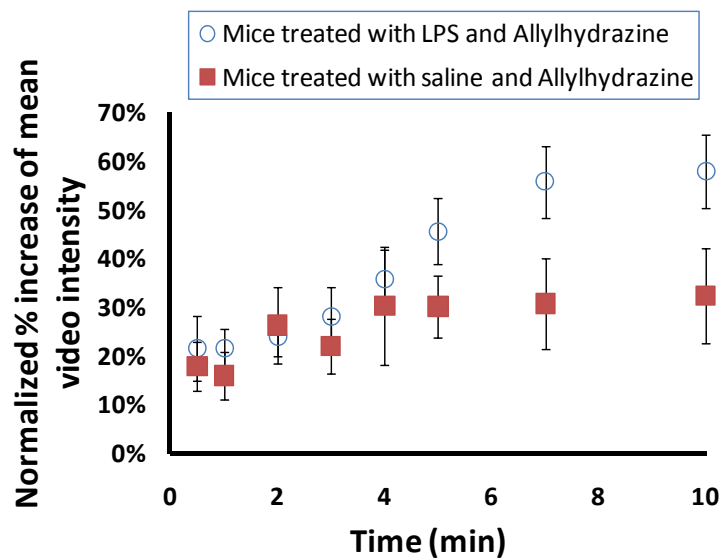


**Figure 6.4.** Quantitative analysis of the ultrasound images in Fig. 6.3 A and B demonstrated that mice treated with allylhydrazine and LPS increased their normalized mean video intensity by 60% (circles), compared to a 30% increase in control mice treated with allylhydrazine and saline (squares). The vertical bars represent standard error.

### 6.3.3 *In vivo* imaging of oxidative stress using allylhydrazine encapsulated within liposomes

We investigated if the APLs are more effective than free allylhydrazine for imaging oxidative stress *in vivo* with an LPS model of inflammation. We first verified that the liposome formulation used to generate the APLs were capable of targeting the liver within 10 minutes (**Fig. 5.7**). Mice were given an intraperitoneal injection of LPS, or saline as a control, and the APLs (14 mg allylhydrazine/mouse) were injected intravenously into the retro-orbital capillary bed 20 hours later. The mice were imaged with a Siemens Acuson clinical ultrasound system at a 14 MHz frequency. **Figure 6.5** illustrates that APLs can enhance acoustic contrast in mice experiencing oxidative stress while maintaining a low background signal in healthy mice. For example, 10 minutes after the APL injection, several bright spots became visible in the livers of LPS-treated mice (**Fig. 6.5 A**), but not in mice treated with saline (**Fig. 6.5 B**).

We performed quantitative analysis on the ultrasound images and **Figure 6.6** shows that after 10 minutes, the normalized mean video intensity of LPS-treated mice increased by 40%, but remained at baseline intensity levels for mice treated with saline. We also verified that the injection of empty APL-based liposomes (at the same lipid concentration used in **Fig. 6.5**) into LPS-treated mice ( $n = 5$ ) did not produce enhanced ultrasound echoes, demonstrating that inflammation in tissue alone did not enhance ultrasound echoes. Together, these results demonstrated that the APLs can reduce the reaction of allylhydrazine with radical oxidants produced in healthy tissue and enhance its efficacy.



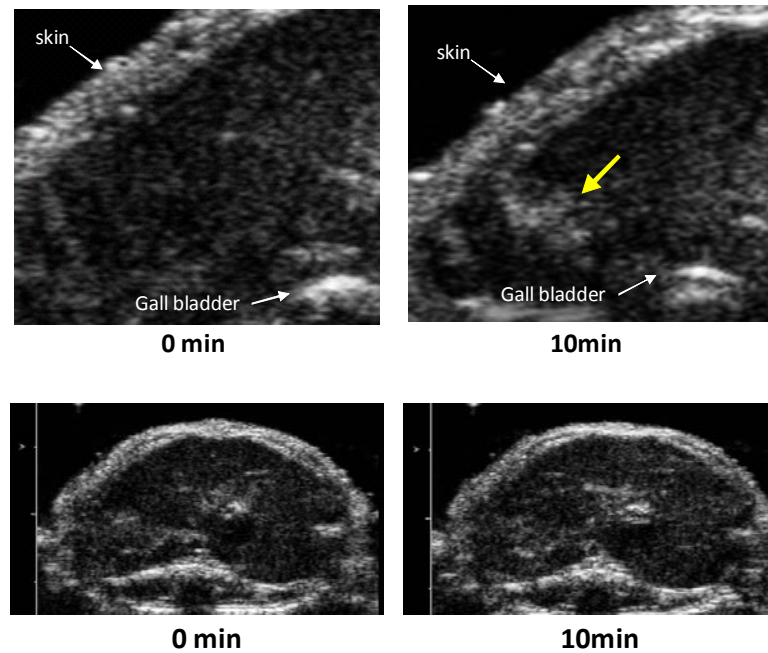
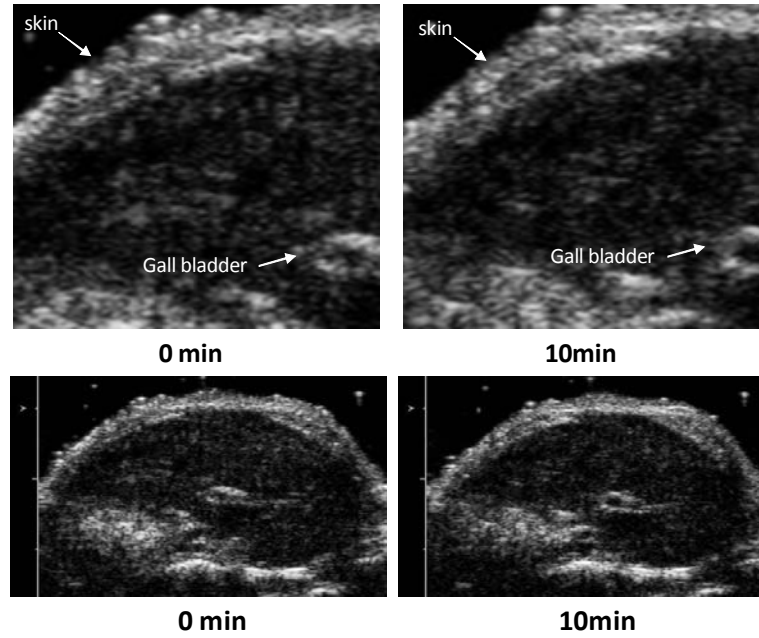


**Figure 6.5.** Representative ultrasound images of mice livers treated with the APLs and LPS versus mice treated with the APLs and saline. Ultrasound images were taken at 0 min and 10 min after the APLs injection. The lower panel shows the entire cross-section area of the mice chest, and the upper panel shows the zoom-in area of the liver.

(A) Mice treated with LPS and the APLs. Representative ultrasound images of the mouse liver show enhanced acoustic contrast 10 minutes after the APLs injection. Arrow indicates location of enhanced acoustic contrast in the liver.



**(B)** Mice treated with saline and the APLs. Representative ultrasound images of the mouse liver did not show significant changes 10 minutes after the APLs injection.

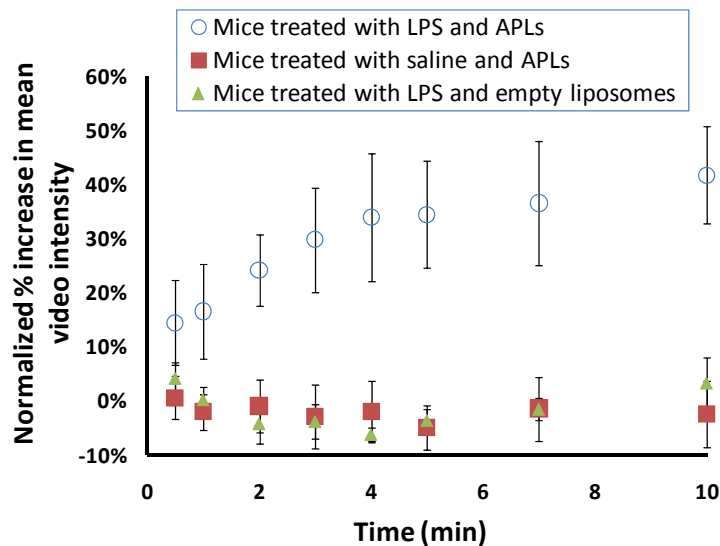


**Figure 6.6.** Quantitative analysis of the ultrasound images in Fig. 6.5 A and B demonstrated that mice treated with the APLs and LPS increased their normalized mean video intensity by 40% (circles), compared to no increase in control mice treated with the APLs and saline (squares). In addition, quantitative image analysis of mice treated with LPS and empty liposomes ( $n = 5$ ) did not show an increase in normalized mean video intensity (triangles). The vertical bars represent standard error.

### 6.3.4 Comparison with clinical contrast agent (Definity)

A clinical contrast agent, Definity was used as a positive control for comparison with our *in vivo* studies. Definity is composed of a perfluoropropane gas core and a PEGylated phospholipid shell with similar composition as the liposomes used in our *in vivo* studies with the APLs. The Definity solution was diluted before injection into mice to match the same clinical dosage for human. All the ultrasound settings remained the same to compare the imaging results of Definity with the APLs.

**Figure 6.7 (A)** shows an ultrasound image of a normal mice liver before injection, and **Figure 6.7 (B)** shows an ultrasound image immediately after the injection of 50  $\mu$ L Definity. The video intensity inside the liver decreased significantly to a dark background with B-mode imaging. **Figure 6.7 (C)** and **(D)** show that the ultrasound image of the mice liver gradually restored back to its original intensity after 5 and 10 minutes, respectively.

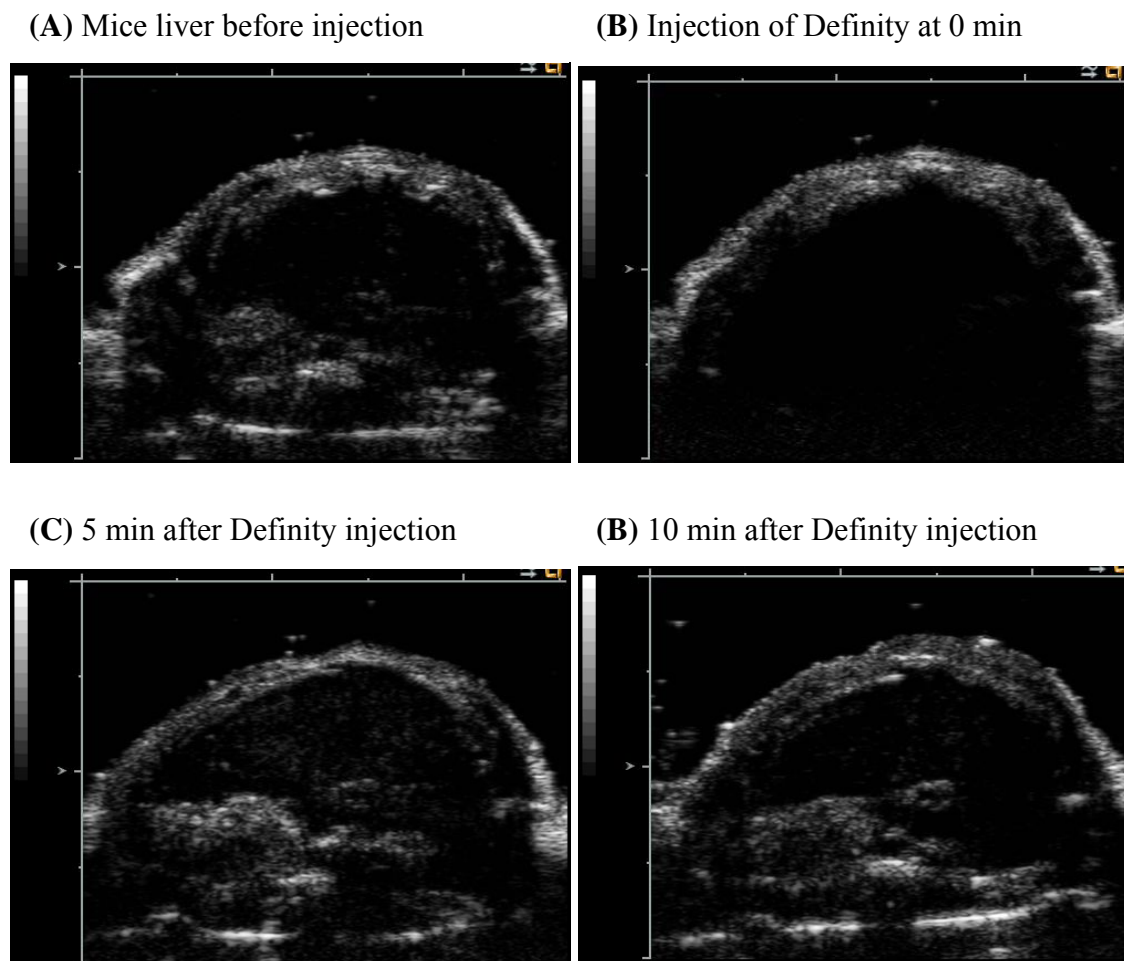


**Figure 6.7.** B-mode imaging of mice liver after intravenous injection of clinical contrast agent Definity.

At first, it was not clear what caused the decrease in video intensity immediately after Definity injection, and how the image restored to its original video intensity after 10 minutes. Since Definity was expected to provide stronger ultrasound signal under contrast mode, the Doppler-mode was used in the second study. The same amount of Definity solution (50  $\mu$ L) was injected into mice intravenously. The ultrasound settings remained the same, except for the additional turning on of Doppler mode imaging at fixed time intervals. **Figure 6.8 (A)** shows an ultrasound image of a normal mice liver before injection, and **Figure 6.8 (B)** shows an ultrasound image immediately after

injection of 50 uL Definity. **Figure 6.8 (C)** shows an inset of Doppler imaging in the liver, and strong Doppler shifts are indicated by the intense blue and red color in the image. **Figure 6.8 (D)** shows the B-mode imaging of mice liver 1 min after injection, and **Figure 6.8 (E)** shows the Doppler-mode imaging at the same time interval. Strong Doppler shift can still be detected after 1 minute. **Figure 6.8 (F)** and **(G)** traced the restoration of video intensity in the mice liver with B-mode imaging after 5, and 10 minutes. Doppler imaging is used to characterize flow and the Doppler shift can be intensified when gas bubbles are flowing in the blood vessel. This result showed that Definity contrast agent can reach the liver, but was only visible through Doppler-mode imaging.

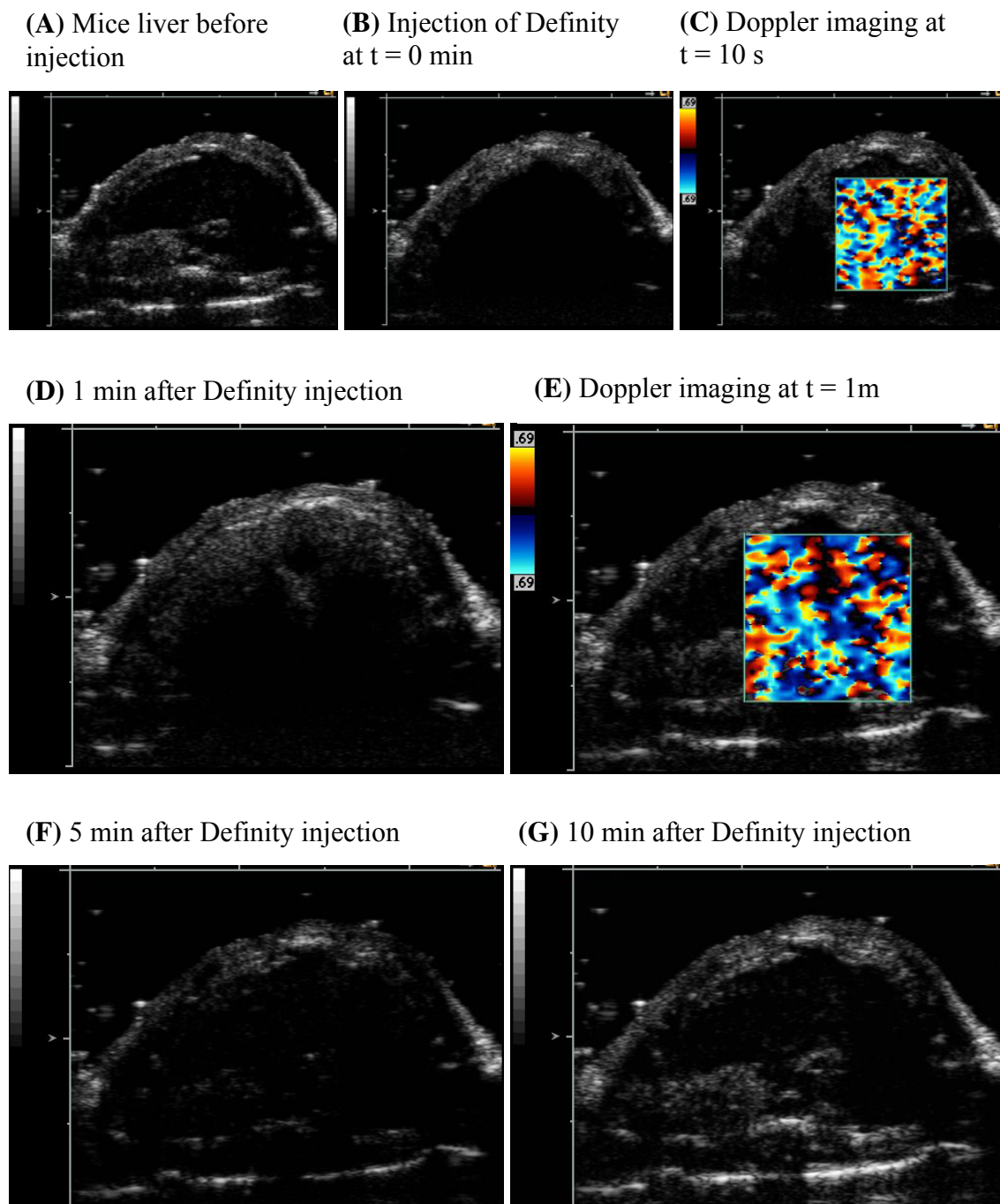


**Figure 6.8.** B-mode and Doppler imaging of mice liver after intravenous injection of clinical contrast agent Definity.

## 6.4 Discussion

### 6.4.1 *In vivo* imaging of oxidative stress using clinical ultrasound system

The ability of allylhydrazine to detect ROS was investigated *in vivo* using a LPS model of inflammation. Our *in vivo* studies demonstrate that allylhydrazine can image oxidative stress in mice liver with good spatial resolution (**Figure 6.3**). Moreover, a 10 minute time-frame for imaging is reasonably fast and suitable for clinical applications, where imaging procedure can take minutes to hours. Quantitative analysis of the ultrasound images (**Figure 6.4**) shows that after 10 minutes, the normalized mean video intensity of LPS-treated mice increased by 60%, compared to an only 30% increase for mice treated with saline. We expect that the 30% increase in background signal observed in saline-treated mice was due to the reaction of allylhydrazine with mitochondrial radical oxidants produced by metabolism [1]. Since liver macrophages are a major source of ROS production in the body, allylhydrazine may react with the ROS in the liver of healthy mice. The enhancement in ultrasound intensity indicated that allylhydrazine reacted with radical oxidants *in vivo* and generated gas forming molecules. These results also demonstrated that allylhydrazine can detect oxidative stress *in vivo* with 3D spatial resolution that cannot be achieved using fluorescent [33] or chemiluminescent [35] based contrast agents.

### 6.4.2 *In vivo* enhancement of liposomal encapsulation

To enhance targeting to the liver and to improve bubble stability, allylhydrazine was encapsulated inside phospholipid liposomes. Both *in vitro* acoustic characterization

and *in vivo* biodistribution studies confirmed our hypothesis (**Figures 5.2 and 5.7**). The *in vivo* studies using the APLs to image oxidative stress displayed similar results with using free allylhydrazine. Incidentally, this approach also has the benefit of reducing the background signal in healthy mice, possibly because the allylhydrazine were released from the APLs to react with the ROS after been endocytosed by activated macrophages, and there were fewer activated macrophages in the liver of healthy mice to endocytose the APLs.

There are, however, limitations to our *in vivo* studies, and it is difficult to extrapolate *in vivo* outcomes from *in vitro* behavior due to various factors such as the spatiotemporal distribution of the APLs, extravasation from blood circulation, and internalization by different cell population. The sensitivity of allylhydrazine toward ROS under *in vivo* conditions may be different from *in vitro* environment, and other biomolecules could compete with ROS to react with allylhydrazine and reduce its effective concentration. Furthermore, physical forces such as viscosity and fluid flow will also affect bubble formation and ultrasound detection. For example, Ferrara et. al. showed that phagocytosed microbubbles experienced viscous damping inside neutrophil [58], and concluded that contrast-enhanced ultrasound can detect distinct acoustic signals from microbubbles inside the neutrophil. This means that it is harder to nucleate bubble within intracellular medium compared to extracellular medium. On the other hand, microbubble-specific imaging sequences have been designed by varying imaging parameters such as the acoustic power, the transmit and receive frequencies, the pulse frequency, the pulse phase and amplitude. Optimization of these parameters is required for different contrast agents to obtain the best diagnostic performance [62].



## CHAPTER 7

### SUMMARY AND FUTURE DIRECTIONS

#### 7.1 Overall Summary

The overproduction of ROS is associated with numerous diseases, and the ability to detect oxidative stress *in vivo* in a clinical setting has the potential to significantly improve the diagnosis of human diseases. Hence, the development of ultrasound imaging probes that detect ROS can have a great impact on translational medicine. The overall objective of this thesis is to develop a new ultrasound contrast agent that has the physical and chemical properties needed to image ROS *in vivo*. This work presents a new approach to perform ultrasound imaging of oxidative stress *in vivo* via chemical reactions that generate gas forming molecules in the presence of ROS. The key issues for this strategy to be successful are: 1) the kinetics of gas generation should be faster than gas diffusion for bubbles to nucleate, 2) the sensitivity of ultrasound to detect gas formation from chemical reactions, and 3) translating this approach into more complex and dynamic conditions *in vivo*.

Here, we demonstrate that ROS can be imaged with allylhydrazine by ultrasound. Allylhydrazine is designed to nucleate gas bubbles in ROS-producing tissues, and the bubbles produce strong acoustic echoes that can be detected by ultrasound. In addition, allylhydrazine was encapsulated within liposomes to improve the *in vivo* efficacy by increasing bubble stability and targeting the liver macrophages, which are the major source of pathogenic ROS production.

The major contribution of this work is transforming a sequence of complex chemical reactions from *in vitro* characterization to *in vivo* applications under

physiological conditions. We demonstrated that the kinetics of gas generation was sufficiently fast for bubble nucleation and physiological concentrations of radical oxidant could be detected by ultrasound in a clinical setting (Aim I; Chapters 3 and 4). We also showed that the *in vivo* efficacy of allylhydrazine was enhanced by liposome encapsulation (Aim II; Chapter 5). Finally, we show that oxidative stress can be detected *in vivo* with clinical ultrasound system (Aim III; Chapter 6). Therefore, imaging ROS with gas-forming reaction could have translational impact on clinical ultrasound diagnostics.

## **7.2 Aim I: Ultrasound Detection of Chemically Generated Microbubbles**

The objectives of this aim were to design appropriate chemical reactions that can generate gas bubbles in the presence of radical oxidants and to investigate the feasibility of ultrasound detection. Allylhydrazine and its analogs were investigated, and the oxidation kinetics of allylhydrazine showed that it possessed suitable kinetics to generate bubbles under physiological conditions. Furthermore, bubble nucleation from the oxidation of allylhydrazine and radical oxidants was confirmed by optical observation and *in vitro* acoustic characterization. The effect of various ultrasound parameters were studied using a custom-built ultrasound system and optimized, and a linear correlation between ultrasound intensity and the concentrations of radical oxidants was observed. We also found that ultrasound can detect small increment (1-2%) of gas concentration above supersaturation, and suggest that classical bubble nucleation theory overestimated the threshold for bubble nucleation.

### **7.3 Aim II: Liposomal Encapsulation and Stabilization of Microbubbles**

The objectives of this aim were to determine if encapsulating allylhydrazine within liposomes can improve bubble stability and enhance *in vivo* efficacy. The effects of various liposome compositions on bubble nucleation were investigated, including lipid chain length, PEGylation, incorporation of charged lipid and porphyrin, loading ratio of lipid to allylhydrazine, and liposomes formulation. The *in vitro* acoustic response demonstrated that allylhydrazine encapsulated within liposomes displayed stronger ultrasound intensity than free allylhydrazine. The *in vivo* biodistribution of liposomes showed that they can target the liver within 10 minutes, demonstrating clinical potential for *in vivo* application.

### **7.4 Aim III: *In Vivo* Imaging of Oxidative Stress**

The objectives of this aim were to demonstrate *in vivo* imaging of oxidative stress using a clinical ultrasound system. We first demonstrated that bubble nucleation could be imaged with ultrasound inside the intraperitoneal cavity of mice by direct local injection of allylhydrazine and hydroxyl radicals into the mice IP cavity. Next, we demonstrated the feasibility of using allylhydrazine to image oxidative stress *in vivo* with clinical ultrasound system based on a LPS model of inflammation. Ultrasound images indicated the presence of oxidative stress in the mouse liver with well-defined resolution, and quantitative image analysis indicated stronger ultrasound signal from mice treated with allylhydrazine and LPS compared to mice treated with allylhydrazine and saline. We also demonstrated that the *in vivo* efficacy of allylhydrazine was improved by

encapsulation within liposomes. Lastly, we investigated a clinical ultrasound contrast agent as a positive control.

## 7.5 Conclusions

The development of contrast agents that can image disease biomarkers in a clinical setting remains a major challenge. Ultrasound contrast agents have tremendous diagnostic potential because of their excellent spatial resolution and the widespread clinical use of ultrasound. Here, we demonstrate a new strategy for performing molecular imaging by ultrasound based on chemical reactions that generate gas forming molecules. This approach was demonstrated with the imaging of ROS by an allylhydrazine-based contrast agent, termed the APLs. The overproduction of radical oxidants is associated with many inflammatory diseases, and therefore the APLs have numerous potential applications. Moreover, the concept of using gas-forming reactions for targeted ultrasound imaging opens up a new area for the development of ultrasound contrast agent outside of pre-formed gas bubbles.

## 7.6 Future directions

The current work demonstrated *in vivo* ultrasound imaging of oxidative stress in the liver based on a LPS model of inflammation. We encapsulated allylhydrazine inside various liposomes compositions (e.g. APLs), and showed that the liposomes can target the liver. Many other diseases associated with ROS such as arthritis, cardiovascular disease, renal ischemia-reperfusion, and muscular inflammation can also be explored with our present approach. However, further studies are needed to investigate the APLs' ability to target areas outside the liver, and to differentiate intracellular versus extracellular response of the APLs. Encapsulating allylhydrazine inside liposomes has

another benefit because toxicity related to allylhydrazine could be another issue for clinical applications, and the current strategy can be optimized by reducing the amount of allylhydrazine used *in vivo* while maintaining sufficient levels of ultrasound signal.

Moreover, the concept of using gas-forming reactions to perform molecular imaging can be applied to other biomarkers. Numerous biologically important molecules, such as enzymes, thiols [109], and the hydronium ion (pH) [54] participate in chemical reactions that generate gas forming molecules, and can potentially be imaged by ultrasound through carefully-designed gas-forming chemistry. Finally, optimization of ultrasound parameters such as harmonic imaging can enhance the detection of acoustic signals specific to bubble nucleation in clinical setting.

## APPENDIX A

### CLINICAL ULTRASOUND SYSTEM AND CALIBRATION

#### Clinical Ultrasound system calibration

A calibration was performed to ensure that the clinical ultrasound system operates in the linear range and that the video intensity increases linearly with ultrasound intensity. The correlation between the ultrasound power, mechanical index and gain settings were characterized. The mechanical index was determined by stepping up the ultrasound power from -30 dB to -10 dB.

To determine the optimal power or mechanical index the ultrasound imaging, a 25 gauge stainless steel needle was used as a reference. The mean video intensity of the reference was measured and the ultrasound power was increased from -30 dB to -10 dB. Two different gain setting were used (-20 dB and -7 dB) to determine if the video intensity reaches saturation.

After the linear ranges for mechanical index and gain level have been determined, we tried to minimize the background signal was minimized while maintaining adequate ultrasound gain at  $MI = 0.05$ . The ultrasound power was chosen to provide the best contrast for the ultrasound image.

The conversion between mechanical index and ultrasound power was plotted in **Figure A.1**. Since all the ultrasound experiments were performed at  $MI = 0.05$ , this corresponds to an ultrasound power of -20 dB.

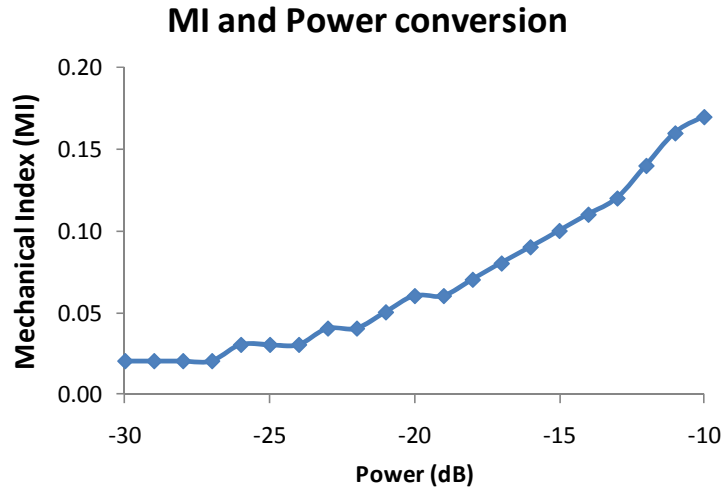


**Figure A.1.** Conversion between mechanical index (MI) and ultrasound power

Figures A.2 and A.3 show that the video intensity is linearly proportional to the ultrasound power at two different gain settings. Based on these characterization, the ultrasound power was set at -20 dB (MI = 0.05) for all imaging studies.

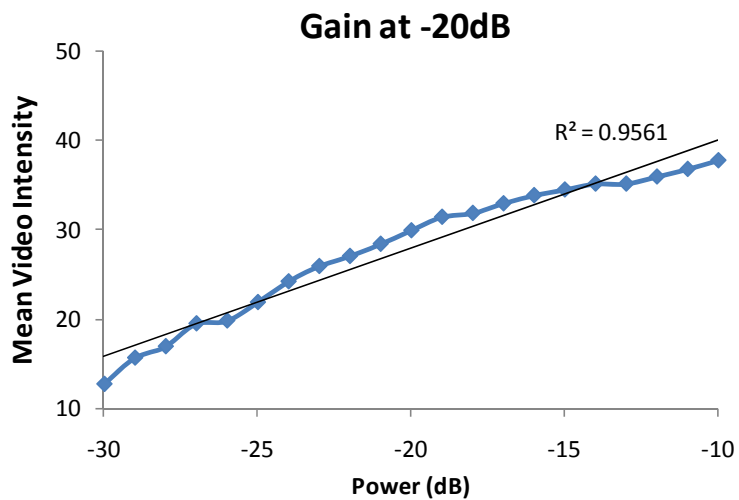


**Figure A.2.** Linear relationship between mean video intensity and power at -20 dB gain

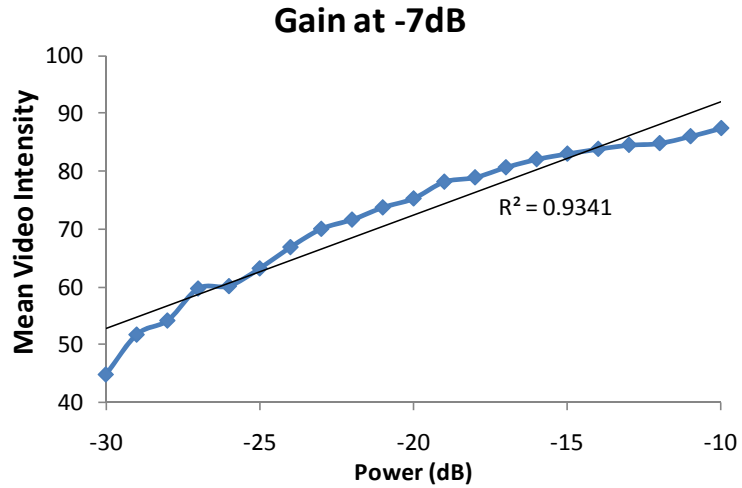


**Figure A.3.** Linear relationship between mean video intensity and power at -7 dB gain

**Figure A.4** shows the correlation between the mean video intensity and ultrasound gain from -20 dB to 0 dB. The gain was set to -7 dB for all imaging studies.

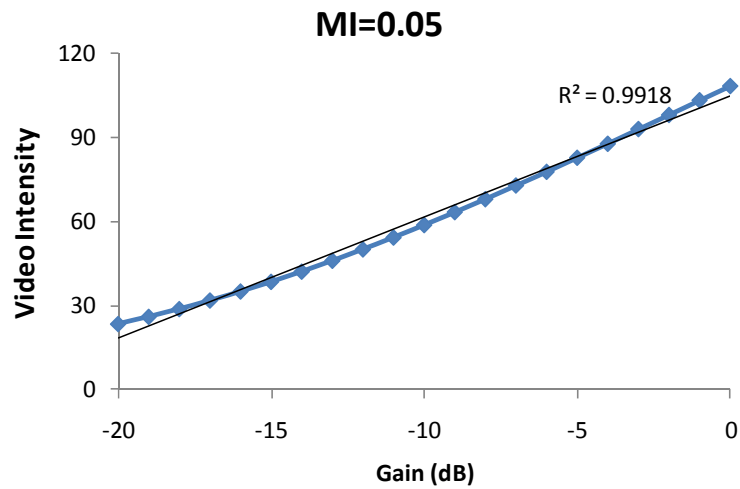


**Figure A.4.** Linear relationship between video intensity and gain at MI = 0.05



## REFERENCES

1. Valko, M., et al., *Free radicals and antioxidants in normal physiological functions and human disease*. Int J Biochem Cell Biol, 2007. **39**(1): p. 44-84.
2. Harvey, C.J., et al., *Advances in ultrasound*. Clin Radiol, 2002. **57**(3): p. 157-77.
3. Kaufmann, B.A. and J.R. Lindner, *Molecular imaging with targeted contrast ultrasound*. Curr Opin Biotechnol, 2007. **18**(1): p. 11-6.
4. Weismann, C.F., et al., *Three-dimensional targeting: a new three-dimensional ultrasound technique to evaluate needle position during breast biopsy*. Ultrasound Obstet Gynecol, 2000. **16**(4): p. 359-64.
5. Bloch, S.H., P.A. Dayton, and K.W. Ferrara, *Targeted imaging using ultrasound contrast agents*. Ieee Engineering in Medicine and Biology Magazine, 2004. **23**(5): p. 18-29.
6. Lindner, J.R., *Microbubbles in medical imaging: current applications and future directions*. Nature Reviews Drug Discovery, 2004. **3**(6): p. 527-532.
7. Correas, J.M., et al., *Ultrasound contrast agents: properties, principles of action, tolerance, and artifacts*. European Radiology, 2001. **11**(8): p. 1316-1328.
8. Kovacic, P., et al., *Mechanism of mitochondrial uncouplers, inhibitors, and toxins: Focus on electron transfer, free radicals, and structure-activity relationships*. Current Medicinal Chemistry, 2005. **12**(22): p. 2601-2623.
9. Klibanov, A.L., *Targeted delivery of gas-filled microspheres, contrast agents for ultrasound imaging*. Advanced Drug Delivery Reviews, 1999. **37**(1-3): p. 139-157.
10. Christiansen, J.P., et al., *Noninvasive imaging of myocardial reperfusion injury using leukocyte-targeted contrast echocardiography*. Circulation, 2002. **105**(15): p. 1764-1767.
11. Willmann, J.K., et al., *Targeted microbubbles for imaging tumor angiogenesis: Assessment of whole-body biodistribution with dynamic micro-PET in mice*. Radiology, 2008. **249**(1): p. 212-219.

12. Willmann, J.K., et al., *US imaging of tumor angiogenesis with microbubbles targeted to vascular endothelial growth factor receptor type 2 in mice*. Radiology, 2008. **246**(2): p. 508-518.
13. Weller, G.E.R., et al., *Ultrasonic imaging of tumor angiogenesis using contrast microbubbles targeted via the tumor-binding peptide arginine-arginine-leucine*. Cancer Research, 2005. **65**(2): p. 533-539.
14. Unger, E.C., et al., *In vitro studies of a new thrombus-specific ultrasound contrast agent*. American Journal of Cardiology, 1998. **81**(12A): p. 58g-61g.
15. Wright, W.H., et al., *Evaluation of new thrombus-specific ultrasound contrast agent*. Academic Radiology, 1998. **5**: p. S240-S242.
16. Dayton, P.A. and K.W. Ferrara, *Targeted imaging using ultrasound*. Journal of Magnetic Resonance Imaging, 2002. **16**(4): p. 362-377.
17. Rapoport, N., Z.G. Gao, and A. Kennedy, *Multifunctional nanoparticles for combining ultrasonic tumor imaging and targeted chemotherapy*. Journal of the National Cancer Institute, 2007. **99**(14): p. 1095-1106.
18. Korpanty, G., et al., *Monitoring response to anticancer therapy by targeting microbubbles to tumor vasculature*. Clinical Cancer Research, 2007. **13**(1): p. 323-330.
19. Catalano, O., et al., *Contrast-enhanced sonography of the spleen*. American Journal of Roentgenology, 2005. **184**(4): p. 1150-1156.
20. Harvey CJ, L.A., Lynch M, Blomley MJK, Cosgrove DO, *Application of ultrasound microbubbles in spleen*, in *Contrast media in ultrasonography: Basic principles and clinical applications*, Q. E, Editor. 2005, Springer, Berlin Heidelberg New York. p. 205-219
21. Thannickal, V.J. and B.L. Fanburg, *Reactive oxygen species in cell signaling*. American Journal of Physiology-Lung Cellular and Molecular Physiology, 2000. **279**(6): p. L1005-L1028.
22. Finkel, T. and N.J. Holbrook, *Oxidants, oxidative stress and the biology of ageing*. Nature, 2000. **408**(6809): p. 239-247.

23. Harman, D., *Aging: a theory based on free radical and radiation chemistry*. J Gerontol, 1956. **11**(3): p. 298-300.
24. Mccord, J.M. and Fridovic.I, *Superoxide Dismutase an Enzymic Function for Erythrocyte (Hemoglobin)*. Journal of Biological Chemistry, 1969. **244**(22): p. 6049-&.
25. Droge, W., *Free radicals in the physiological control of cell function*. Physiological Reviews, 2002. **82**(1): p. 47-95.
26. Turrens, J.F., *Superoxide production by the mitochondrial respiratory chain*. Bioscience Reports, 1997. **17**(1): p. 3-8.
27. Cadenas, E. and H. Sies, *The lag phase*. Free Radical Research, 1998. **28**(6): p. 601-609.
28. Valko, M., et al., *Role of oxygen radicals in DNA damage and cancer incidence*. Molecular and Cellular Biochemistry, 2004. **266**(1-2): p. 37-56.
29. Boveris, A. and B. Chance, *Mitochondrial Generation of Hydrogen-Peroxide - General Properties and Effect of Hyperbaric-Oxygen*. Biochemical Journal, 1973. **134**(3): p. 707-716.
30. Aikens, J. and T.A. Dix, *Perhydroxyl Radical (H<sub>2</sub>O<sub>2</sub>) Initiated Lipid-Peroxidation - the Role of Fatty-Acid Hydroperoxides*. Journal of Biological Chemistry, 1991. **266**(23): p. 15091-15098.
31. Valko, M., et al., *Free radicals, metals and antioxidants in oxidative stress-induced cancer*. Chemico-Biological Interactions, 2006. **160**(1): p. 1-40.
32. Tanaka, K., et al., *Rational design of fluorescein-based fluorescence probes. Mechanism-based design of a maximum fluorescence probe for singlet oxygen*. J Am Chem Soc, 2001. **123**(11): p. 2530-6.
33. Gomes, A., E. Fernandes, and J.L.F.C. Lima, *Fluorescence probes used for detection of reactive oxygen species*. Journal of Biochemical and Biophysical Methods, 2005. **65**(2-3): p. 45-80.

34. Rice, B.W., M.D. Cable, and M.B. Nelson, *In vivo imaging of light-emitting probes*. J Biomed Opt, 2001. **6**(4): p. 432-40.
35. Chen, W.T., C.H. Tung, and R. Weissleder, *Imaging reactive oxygen species in arthritis*. Mol Imaging, 2004. **3**(3): p. 159-62.
36. Lee, D., et al., *In vivo imaging of hydrogen peroxide with chemiluminescent nanoparticles*. Nat Mater, 2007. **6**(10): p. 765-9.
37. Scharlin, P., et al., *Solubility of gases in water: Correlation between solubility and the number of water molecules in the first solvation shell*. Pure and Applied Chemistry, 1998. **70**(10): p. 1895-1904.
38. Corey, E.J., et al., *Stereospecific Total Synthesis of (+/-)-Cafestol*. Journal of the American Chemical Society, 1987. **109**(15): p. 4717-4718.
39. Jabbari, A., E.J. Sorensen, and K.N. Houk, *Transition states of the retro-ene reactions of allylic diazenes*. Organic Letters, 2006. **8**(14): p. 3105-3107.
40. Price, J.D. and R.P. Johnson, *Thermal Rearrangements of Cyclic Allenes Via Retro-Ene Reactions*. Tetrahedron Letters, 1985. **26**(21): p. 2499-2502.
41. Benn, F.R., J. Dwyer, and I. Chappell, *Ene Reaction of Maleic-Anhydride with Alkenes*. Journal of the Chemical Society-Perkin Transactions 2, 1977(5): p. 533-535.
42. Stephenson, L.M. and D.L. Mattern, *Stereochemistry of an Ene Reaction of Dimethyl Azodicarboxylate*. Journal of Organic Chemistry, 1976. **41**(22): p. 3614-3619.
43. Yu, Z.X. and K.N. Houk, *Intramolecular 1,3-dipolar ene reactions of nitrile oxides occur by stepwise 1,1-cycloaddition/retro-ene mechanisms*. Journal of the American Chemical Society, 2003. **125**(45): p. 13825-13830.
44. Calderwood, T.S., et al., *Oxidation of Substituted Hydrazines by Superoxide Ion - the Initiation Step for the Autoxidation of 1,2-Diphenylhydrazine*. Journal of the American Chemical Society, 1984. **106**(17): p. 4683-4687.

45. Nanni, E.J. and D.T. Sawyer, *Superoxide Ion Oxidation of Hydrophenazines, Reduced Flavins, Hydroxylamine, and Related Substrates Via Hydrogen-Atom Transfer*. Journal of the American Chemical Society, 1980. **102**(25): p. 7591-7593.
46. Misra, H.P. and I. Fridovich, *Oxidation of Phenylhydrazine - Superoxide and Mechanism*. Biochemistry, 1976. **15**(3): p. 681-687.
47. Itano, H.A. and J.L. Matteson, *Mechanism of initial reaction of phenylhydrazine with oxyhemoglobin and effect of ring substitutions on the biomolecular rate constant of this reaction*. Biochemistry, 1982. **21**(10): p. 2421-6.
48. Chern, C.I. and J.S. Filippio, *Reaction of Superoxide with Hydrazines, Hydrazones, and Related Compounds*. Journal of Organic Chemistry, 1977. **42**(1): p. 178-180.
49. Jones, S.F., G.M. Evans, and K.P. Galvin, *Bubble nucleation from gas cavities - a review*. Advances in Colloid and Interface Science, 1999. **80**(1): p. 27-50.
50. Blander, M. and J.L. Katz, *Bubble Nucleation in Liquids*. Aiche Journal, 1975. **21**(5): p. 833-848.
51. Lubetkin, S.D., *Why is it much easier to nucleate gas bubbles than theory predicts?* Langmuir, 2003. **19**(7): p. 2575-2587.
52. Bowers, P.G., K. BarEli, and R.M. Noyes, *Chemical oscillations and instabilities .100. Unstable supersaturated solutions of gases in liquids and nucleation theory*. Journal of the Chemical Society-Faraday Transactions, 1996. **92**(16): p. 2843-2849.
53. Finkelstein, Y. and A. Tamir, *Formation of Gas-Bubbles in Supersaturated Solutions of Gases in Water*. Aiche Journal, 1985. **31**(9): p. 1409-1419.
54. Rubin, M.B. and R.M. Noyes, *Chemical Oscillations and Instabilities .77. Measurements of Critical Supersaturation for Homogeneous Nucleation of Bubbles*. Journal of Physical Chemistry, 1987. **91**(15): p. 4193-4198.

55. Klibanov, A.L., et al., *Detection of individual microbubbles of ultrasound contrast agents: imaging of free-floating and targeted bubbles*. Invest Radiol, 2004. **39**(3): p. 187-95.
56. Sboros, V., et al., *Absolute measurement of ultrasonic backscatter from single microbubbles*. Ultrasound Med Biol, 2005. **31**(8): p. 1063-72.
57. Sun, Y., et al., *Observation of contrast agent response to chirp insonation with a simultaneous optical-acoustical system*. IEEE Trans Ultrason Ferroelectr Freq Control, 2006. **53**(6): p. 1130-7.
58. Dayton, P.A., et al., *Optical and acoustical dynamics of microbubble contrast agents inside neutrophils*. Biophysical Journal, 2001. **80**(3): p. 1547-1556.
59. Leighton, T., *The acoustic bubble*. 1994, London: Academic Press.
60. Fyrrillas, M.M. and A.J. Szeri, *Dissolution or Growth of Soluble Spherical Oscillating Bubbles*. Journal of Fluid Mechanics, 1994. **277**: p. 381-407.
61. Blake, F., *The onset of cavitation in liquids. I. Cavitation threshold sound pressures in water as a function of temperature and hydrostatic pressure*, Harvard university Acoustic Research Laboratory Technical Memorandum p. 1-52.
62. Frinking, P.J.A., et al., *Ultrasound contrast imaging: Current and new potential methods*. Ultrasound in Medicine and Biology, 2000. **26**(6): p. 965-975.
63. de Jong, N., et al., *Optical imaging of contrast agent microbubbles in an ultrasound field with a 100-MHz camera*. Ultrasound in Medicine and Biology, 2000. **26**(3): p. 487-492.
64. Dayton, P.A., et al., *Optical and acoustical observations of the effects of ultrasound on contrast agents*. Ieee Transactions on Ultrasonics Ferroelectrics and Frequency Control, 1999. **46**(1): p. 220-232.
65. Morgan, K.E., et al., *Experimental and theoretical evaluation of microbubble behavior: Effect of transmitted phase and bubble size*. Ieee Transactions on Ultrasonics Ferroelectrics and Frequency Control, 2000. **47**(6): p. 1494-1509.

66. Caskey, C.F., et al., *Direct observations of ultrasound microbubble contrast agent interaction with the microvessel wall*. Journal of the Acoustical Society of America, 2007. **122**(2): p. 1191-1200.
67. Vanliew, H.D. and M.E. Burkard, *Behavior of Bubbles of Slowly Permeating Gas Used for Ultrasonic-Imaging Contrast*. Investigative Radiology, 1995. **30**(5): p. 315-321.
68. Kabalnov, A., et al., *Dissolution of multicomponent microbubbles in the bloodstream: 1. Theory*. Ultrasound in Medicine and Biology, 1998. **24**(5): p. 739-749.
69. de Jong, N., et al., *Ultrasonic characterization of ultrasound contrast agents*. Medical & Biological Engineering & Computing, 2009. **47**(8): p. 861-873.
70. Duncan, P.B. and D. Needham, *Test of the Epstein-Plesset model for gas microparticle dissolution in aqueous media: Effect of surface tension and gas undersaturation in solution*. Langmuir, 2004. **20**(7): p. 2567-2578.
71. Cable, M. and J.R. Frade, *The Influence of Surface-Tension on the Diffusion-Controlled Growth or Dissolution of Spherical Gas-Bubbles*. Proceedings of the Royal Society of London Series a-Mathematical Physical and Engineering Sciences, 1988. **420**(1859): p. 247-265.
72. Barnhart, J., et al., *Characteristics of Albunex: air-filled albumin microspheres for echocardiography contrast enhancement*. Invest Radiol, 1990. **25 Suppl 1**: p. S162-4.
73. Wheatley, M.A. and S. Singhal, *Structural Studies on Stabilized Microbubbles - Development of a Novel Contrast Agent for Diagnostic Ultrasound*. Reactive Polymers, 1995. **25**(2-3): p. 157-166.
74. Wang, W.H., C.C. Moser, and M.A. Wheatley, *Langmuir trough study of surfactant mixtures used in the production of a new ultrasound contrast agent consisting of stabilized microbubbles*. Journal of Physical Chemistry, 1996. **100**(32): p. 13815-13821.
75. Singhal, S., C.C. Moser, and M.A. Wheatley, *Surfactant-Stabilized Microbubbles as Ultrasound Contrast Agents - Stability Study of Span-60 and Tween-80 Mixtures Using a Langmuir Trough*. Langmuir, 1993. **9**(9): p. 2426-2429.

76. Bjerknes, K., et al., *Preparation of polymeric microbubbles: formulation studies and product characterisation*. International Journal of Pharmaceutics, 1997. **158**(2): p. 129-136.
77. Unger, E.C., et al., *Local drug and gene delivery through microbubbles*. Prog Cardiovasc Dis, 2001. **44**(1): p. 45-54.
78. Kim, D.H., A.L. Klibanov, and D. Needham, *The influence of tiered layers of surface-grafted poly(ethylene glycol) on receptor-ligand-mediated adhesion between phospholipid monolayer-stabilized microbubbles and coated glass beads*. Langmuir, 2000. **16**(6): p. 2808-2817.
79. AlkanOnyuksel, H., et al., *Development of inherently echogenic liposomes as an ultrasonic contrast agent*. Journal of Pharmaceutical Sciences, 1996. **85**(5): p. 486-490.
80. Demos, S.M., et al., *In vivo targeting of acoustically reflective liposomes for intravascular and transvascular ultrasonic enhancement*. Journal of the American College of Cardiology, 1999. **33**(3): p. 867-875.
81. Huang, S.L. and R.C. MacDonald, *Acoustically active liposomes for drug encapsulation and ultrasound-triggered release*. Biochimica Et Biophysica Acta-Biomembranes, 2004. **1665**(1-2): p. 134-141.
82. Pu, G., M.L. Longo, and M.A. Borden, *Effect of microstructure on molecular oxygen permeation through condensed phospholipid monolayers*. Journal of the American Chemical Society, 2005. **127**(18): p. 6524-6525.
83. Borden, M.A. and M.L. Longo, *Dissolution behavior of lipid monolayer-coated, air-filled microbubbles: Effect of lipid hydrophobic chain length*. Langmuir, 2002. **18**(24): p. 9225-9233.
84. Kim, D., *Mechanical Properties, Microstructure, and Specific Adhesion of Phospholipid Monolayer-Coated Microbubbles*. 1999, Duke University.
85. Torchilin, V.P., *PEG-based micelles as carriers of contrast agents for different imaging modalities*. Advanced Drug Delivery Reviews, 2002. **54**(2): p. 235-252.



86. *Definity Data sheet*. September 2009, Global Medical Solutions Ltd: Auckland, New Zealand.
87. Lindner, J.R., et al., *Noninvasive imaging of inflammation by ultrasound detection of phagocytosed microbubbles*. *Circulation*, 2000. **102**(5): p. 531-538.
88. Lindner, J.R., et al., *Noninvasive ultrasound imaging of inflammation using microbubbles targeted to activated leukocytes*. *Circulation*, 2000. **102**(22): p. 2745-2750.
89. Lindner, J.R., et al., *Microbubble persistence in the microcirculation during ischemia/reperfusion and inflammation is caused by integrin- and complement-mediated adherence to activated leukocytes*. *Circulation*, 2000. **101**(6): p. 668-675.
90. Villanueva, F.S., et al., *Microbubbles targeted to intercellular adhesion molecule-1 bind to activated coronary artery endothelial cells*. *Circulation*, 1998. **98**(1): p. 1-5.
91. Halliwell, B., *Reactive Oxygen Species in Living Systems - Source, Biochemistry, and Role in Human-Disease*. *American Journal of Medicine*, 1991. **91**: p. S14-S22.
92. Blomley, M., et al., *Stimulated acoustic emission in liver parenchyma with Levovist*. *Lancet*, 1998. **351**(9102): p. 568-568.
93. Forsberg, F., et al., *Tissue-specific US contrast agent for evaluation of hepatic and splenic parenchyma*. *Radiology*, 1999. **210**(1): p. 125-132.
94. Leen, E., et al., *Prospective multicenter trial evaluating a novel method of characterizing focal liver lesions using contrast-enhanced sonography*. *American Journal of Roentgenology*, 2006. **186**(6): p. 1551-1559.
95. Schneider, M., et al., *Gray-scale liver enhancement in VX2 tumor-bearing rabbits using BR14, a new ultrasonographic contrast agent*. *Investigative Radiology*, 1997. **32**(7): p. 410-417.

96. Tarantino, L., et al., *Diagnosis of benign and malignant portal vein thrombosis in cirrhotic patients with hepatocellular carcinoma: color Doppler US, contrast-enhanced US, and fine-needle biopsy*. *Abdom Imaging*, 2006. **31**(5): p. 537-44.
97. Berry, J.D. and P.S. Sidhu, *Microbubble contrast-enhanced ultrasound in liver transplantation*. *Eur Radiol*, 2004. **14 Suppl 8**: p. P96-103.
98. Rossi, S., et al., *Contrast-enhanced versus conventional and color Doppler sonography for the detection of thrombosis of the portal and hepatic venous systems*. *AJR Am J Roentgenol*, 2006. **186**(3): p. 763-73.
99. Quaia, E., et al., *Characterization of focal liver lesions with contrast specific US modes and a sulfur hexafluoride-filled microbubble contrast agent: Diagnostic performance and confidence*. *Radiology*, 2004. **232**(2): p. 420-430.
100. Kim, S.H., et al., *Value of contrast-enhanced sonography for the characterization of focal hepatic lesions in patients with diffuse liver disease: receiver operating characteristic analysis*. *AJR Am J Roentgenol*, 2005. **184**(4): p. 1077-84.
101. Nicolau, C., et al., *Importance of evaluating all vascular phases on contrast-enhanced sonography in the differentiation of benign from malignant focal liver lesions*. *American Journal of Roentgenology*, 2006. **186**(1): p. 158-167.
102. Nicolau, C., et al., *Evaluation of hepatocellular carcinoma using SonoVue, a second generation ultrasound contrast agent: correlation with cellular differentiation*. *European Radiology*, 2004. **14**(6): p. 1092-1099.
103. Quaia, E., et al., *Comparison of visual and quantitative analysis for characterization of insonated liver tumors after microbubble contrast injection*. *American Journal of Roentgenology*, 2006. **186**(6): p. 1560-1570.
104. Fretland, D.J., et al., *Temporal relationships of cytokine production in mouse non-lethal sepsis: Effect of nitric oxide synthase inhibitors*. *Inflammation Research*, 1997. **46**: p. S155-S156.
105. Rubin, M.B., R.M. Noyes, and K.W. Smith, *Oscillations and Instabilities in Chemical-Systems .74. Gas-Evolution Oscillators .9. A Study of the Ammonium Nitrite Oscillator*. *Journal of Physical Chemistry*, 1987. **91**(6): p. 1618-1622.

106. Gerth, W.A. and E.A. Hemmingsen, *Heterogeneous Nucleation of Bubbles at Solid-Surfaces in Gas-Super-Saturated Aqueous-Solutions*. Journal of Colloid and Interface Science, 1980. **74**(1): p. 80-89.
107. Bowers, P.G., et al., *Supersaturation Limit for Homogeneous Nucleation of Oxygen Bubbles in Water at Elevated Pressure - Superhenry-Law*. Journal of Physical Chemistry, 1995. **99**(23): p. 9632-9637.
108. Hey, M.J., A.M. Hilton, and R.D. Bee, *The Formation and Growth of Carbon-Dioxide Gas-Bubbles from Supersaturated Aqueous-Solutions*. Food Chemistry, 1994. **51**(4): p. 349-357.
109. Zalipsky, S., et al., *Thiolitically cleavable dithiobenzyl urethane-linked polymer-protein conjugates as macromolecular prodrugs: Reversible PEGylation of proteins*. Bioconjugate Chemistry, 2007. **18**(6): p. 1869-1878.
110. Kakade, M.L. and I.E. Liener, *Determination of Available Lysine in Proteins*. Analytical Biochemistry, 1969. **27**(2): p. 273-&.
111. Re, R., et al., *Antioxidant activity applying an improved ABTS radical cation decolorization assay*. Free Radical Biology and Medicine, 1999. **26**(9-10): p. 1231-1237.
112. Bird, R.B., W.E. Stewart, and E.N. Lightfoot, *Transport phenomena*. 2nd, Wiley international ed. 2002, New York: J. Wiley. xii, 895 p.
113. Ferrell, R.T. and Himmelbl.Dm, *Diffusion Coefficients of Nitrogen and Oxygen in Water*. Journal of Chemical and Engineering Data, 1967. **12**(1): p. 111-&.
114. Cadenas, E. and K.J.A. Davies, *Mitochondrial free radical generation, oxidative stress, and aging*. Free Radical Biology and Medicine, 2000. **29**(3-4): p. 222-230.
115. Goldstein, S., D. Meyerstein, and G. Czapski, *The Fenton Reagents*. Free Radical Biology and Medicine, 1993. **15**(4): p. 435-445.
116. Herbert, E., S. Balibar, and F. Caupin, *Cavitation pressure in water*. Physical Review E, 2006. **74**(4): p. -.

117. Zheng, Q., et al., *Liquids at Large Negative Pressures - Water at the Homogeneous Nucleation Limit*. Science, 1991. **254**(5033): p. 829-832.
118. Church, C.C., *Spontaneous homogeneous nucleation, inertial cavitation and the safety of diagnostic ultrasound*. Ultrasound in Medicine and Biology, 2002. **28**(10): p. 1349-1364.
119. Apfel, R.E. and C.K. Holland, *Gauging the Likelihood of Cavitation from Short-Pulse, Low-Duty Cycle Diagnostic Ultrasound*. Ultrasound in Medicine and Biology, 1991. **17**(2): p. 179-185.
120. Talanquer, V. and D.W. Oxtoby, *Nucleation of Bubbles in Binary Fluids*. Journal of Chemical Physics, 1995. **102**(5): p. 2156-2164.
121. Church, C.C., *Spontaneous homogeneous nucleation, inertial cavitation and the safety of diagnostic ultrasound*. Ultrasound Med Biol, 2002. **28**(10): p. 1349-64.
122. Eller, A. and H.G. Flynn, *Rectified Diffusion during Nonlinear Pulsations of Cavitation Bubbles*. Journal of the Acoustical Society of America, 1965. **37**(3): p. 493-&.
123. Borden, M.A., et al., *Surface phase behavior and microstructure of lipid/PEG-emulsifier monolayer-coated microbubbles*. Colloids and Surfaces B-Biointerfaces, 2004. **35**(3-4): p. 209-223.
124. Hettiarachchi, K., et al., *On-chip generation of microbubbles as a practical technology for manufacturing contrast agents for ultrasonic imaging*. Lab on a Chip, 2007. **7**(4): p. 463-468.

## **VITA**

### **JOHN KANGCHUN PERNG**

John received a B.S. in Electrical Engineering and Computer Science from the University of California Berkeley in 2001, and a M.S. in Electrical and Computer Engineering from Georgia Institute of Technology in 2006 before pursuing a doctorate in Bioengineering at Georgia Institute of Technology.